UNIVERSITY OF OKLAHOMA

GRADUATE COLLEGE

GEOPHYSICAL CHARACTERIZATION OF RESOURCE PLAYS

A DISSERTATION

SUBMITTED TO THE GRADUATE FACULTY

in partial fulfillment of the requirements for the

Degree of

DOCTOR OF PHILOSOPHY

By

SWETAL PATEL
Norman, Oklahoma
2020

GEOPHYSICAL CHARACTERIZATION OF RESOURCE PLAYS

A DISSERTATION APPROVED FOR THE
SCHOOL OF GEOSCIENCES

BY THE COMMITTEE CONSISTING OF

Dr. Kurt J. Marfurt, Chair

Dr. Heather Bedle

Dr. Xiaowei Chen

Dr. Ali Tinni

Dr. Sumit Verma

To my family and friends like family

ACKNOWLEDGEMENTS

I have received an enormous amount of support during my time pursuing a Ph.D.; the journey would not have been possible without the support of a lot of people.

First and foremost, I would like to thank my advisor Dr. Kurt Marfurt. This dissertation would not have been possible without the support, guidance, idea, motivation, and encouragement provided by Dr. Marfurt. With a background in petroleum engineering, I had less idea about the reflection seismology processing and interpretation. My career transitioning from petroleum engineering to interpretative reflection seismology would not have been easy without the career guidance of Dr. Marfurt. His suggested course works were apt for the research I wanted to conduct. He understood my shortcomings in computational geophysics and wrote all the algorithms required for the research work. His passion for computational geophysics and machine learning applications in geophysics motivates me to overcome my shortcomings in the area. Apart from improving my research ability, I have learned to be patient, humble, techniques to motivates team, passion for work, and time management. He is the most wonderful and joyful person I have ever met in my life.

I would like to thank Dr. Carl Sondergeld, Dr. Chandra Rai, Dr. Ali Tinni, and Dr. Deepak Devegowda for their support and critical analysis of my research in geophysical characterization of Meramec formation. They provided me core measurements required for the research. Without their input, none of the research would have been possible. They have taught me to be an independent learner and how to be the best version of myself in the work I pursue.

Next, I would like to thank Thang Ha for kindly providing me technical support I needed to carry out tasks, whether related to learning interpretation and processing software or required for research. His quick

response prevented all the setbacks. I think I speak on behalf of all the students working with Dr. Marfurt; you are an invaluable asset to the team.

I would also like to thank Ishank Gupta and Jing Fu for providing me rock type and core velocity analysis data required for my research. I appreciate their quick response to my data requirements. Ishank Gupta guided me very patiently in structuring my further studies in machine learning applications.

I also want to thank Dr. Matthew Pranter and his students Javier Téllez-Rodríguez, Hope Williams, Michael Miller, and Laynie Hardisty for proving geological data, and input to my research in reservoir characterization of Meramec play. The geological discussion with Javier gave me a great insight into incorporating geology to my geophysical analysis.

I also want to thank Mr. Chris McLain for sharing his geologic insight as well as providing critical mentorship throughout this project. He has been a great support throughout my time pursuing research on Meramec. I appreciate his quick response to all my data and technical needs.

I appreciate the input of Dr. Xiaowei Chen and Dr. Bedle Heather to my research. I am thankful to them for agreeing to be committee members on my dissertation. Dr. Chen and Dr. Marfurt' s analysis of earthquakes and delineated faults in the Anadarko Basin lead to the shaping of chapter three of my dissertation.

I would like to thank Dr. Sumit Verma to be one of the committee members. He motivates me to write papers and engage in extracurricular activities. He guided me very well in pursuing extracurricular activities hosted by SEG.

I would also like to thank the entire administrative staff of the School of Geosciences. They provided timely assistance with finances and reimbursements, making my life easy and simple. This is the most welcoming, approachable, efficient, and easy-going staff I have worked with. A great number of thanks to

Rebecca Fay for guiding me with graduate college requirements and helping me with all the issues I faced with credit transfer and paperwork. She made my life a lot simpler by providing quick and correct guidance.

I would also like to thank my co-authors and friends Saurabh Sinha, Saurabh Goyal, Lennon Infante, Megan Gunther, Gabriel Machado, Yuji Kim, David Lubo, Bin Lyu, Karen Leopoldino, Emilio Torres, Francis Oyebanji, Clayton Silver, Abdulmohsen AlAli, Julian Chenin, Roberto Clairmont, Karelia LaMarca-Molina, and Tao Zao for listening to my research at meetings and providing their valuable feedback. Hangout with them relieved the occasional stress I experience when things did not work out as expected.

I thank all the consortium members for providing financial assistance to me while I pursued my research. Without their financial assistance and guidance, the research students pursue at the University of Oklahoma is not possible.

Finally, I am grateful to my mom, dad, wife, and sister-in-law for their moral support throughout my research work. They made these four years of research simple in ways I cannot apprehend. My special thanks to my nephew, Naksh, my wife, and sister-in-law. Spending time with them, relieved me from all the stress, and provided a break from my research thoughts. It cultivated new ideas and solutions to the research problems.

TABLE OF CONTENTS

LIST OF FIGURES

ABSTRACT

The shale exploration and production in the United States have changed the dynamics of the oil and gas business in the world. The production heterogeneity associated with shale resource plays demands recording different kinds of data during the lifecycle of a shale reservoir. Surface seismic, microseismic, well logs, vertical seismic profile (VSP), and core data are some of the most common data acquired for subsurface characterization. Due to the large number of wells drilled in some of the most prolific basins such as Anadarko and Permian Basins, geoscientist resort to well correlations and statistical analysis to plan optimum well locations and the surface seismic data is considered unsought. Well planning with well log correlation entails high uncertainty due to high inherent rock heterogeneity. In this dissertation, I show how incorporating the surface seismic data with log/core data can decrease the uncertainty of mapping producible rock types, and aid in avoiding perilous drilling location such as those that can cause induced earthquakes.

In this dissertation I show a methodology that combines core and seismic data to delineate petrophysically defined rock types away from the cored well. In the case study presented in the dissertation, the rock types were delineated over an area of 477 square miles from measurements conducted on one cored well. The rock types were defined using porosity and permeability values and estimated away from the well by combining elastic measurements from seismic and core samples. The seismic elastic properties P-impedance (Z_P), S-impedance (Z_S), and density (ρ) were estimated by simultaneous prestack inversion. One of the limitations of estimating elastic parameters from prestack data is Z_S, and ρ experiencing a decrease in resolution compared to Z_P due stretching of the non-zero offset data caused by NMO corrections. Hence, we propose a

method to compensate for the NMO stretch that balances the spectrum across the reflector, increasing the resolution of Z_S and ρ after prestack inversion.

In the final chapter of the dissertation, I propose methodologies to image seismogenic faults. The strike-slip faulting is the dominant deformation style in Anadarko Basin, and the faults get unrecognized due to their low offset in the sedimentary formation while planning water injection or hydrocarbon production well. These faults might act seismogenic to injection or production activities based on their orientation and regional stress conditions. I propose a new method called band-limited multispectral coherence to image the strike-slip faults in basins with similar deformation style as Anadarko Basin and with a record of active induced seismicity. In Anadarko Basin, the strong visual correlation between recorded earthquakes and the faults delineated by the proposed methodology signals the seismogenic nature of the faults. The faults with no associated induced seismicity, geomechanical modeling is proposed to investigate their reactivation potential.

CHAPTER 1 INTRODUCTION

After the Mitchell energy commercialized the first Shale gas well in 1991, more than 1 million wells have been drilled in the United States producing more than 12 million barrels of oil and 100 billion cubic feet of natural gas per day in 2019, making country the largest producer of oil and gas in the world (EIA report 2019). A vast amount of seismic, core and log data have been recorded through these years for drilling these wells but only 25% of the data is used for analysis (personal communication Halliburton personals). In the dissertation, I discuss methods to improve the value of products that can be created with the core, log, and/or seismic data.

In Chapter 1, I address the problems associated with NMO/migration stretched data. I discuss about the improvements that can be made in analyzing seismic data by compensating for NMO/migration stretch. Alignment of the non-zero offset traces with the zero offset traces causes stretching of the non-zero offset traces which is proportional to source-receiver offset to depth ratio. The stretching causes changes in AVO and AVAZ signature and decrease in resolution of prestack inversion products. I propose a method to compensate for the stretch using matching pursuit algorithm to locate the reflection's spike, fit wavelet to the data and then compensate for the migration stretch. The method was applied to the wide azimuth survey acquired over the Fort Worth Basin. A less than 2^{o} dip of the reflectors in the study area makes seismic data ideal for testing the applicability of the method. The method balances the frequency across the reflectors increasing resolution of the far-offset data. We support out analysis with forward AVO modeling and address the limitation of the methods using elastic modeling.

In Chapter 2, I discuss about spatial delineation of rock types by combining core and seismic data. It is very well established that the resource play exploitation must deal with inherit production heterogeneity which arise due to low fluid flow capacity of the rock matrix. The effectiveness of the exploitation will depend on the way the hydraulic fractures intersects with the producible and permeable rock types. Hence, it is imperative to locate such rock types before the well or completion is planned. I propose a methodology to define rock types using porosity and permeability measured on core samples, thereafter upscaling the rock types to seismic scale using Bayesian statistics. I address the challenges that occur in extending the rock types from core to seismic due to resolution difference between core and seismic. The methodology was applied to a survey acquired over the STACK area of Anadarko Basin located in the north central Oklahoma in the Anadarko Basin. The outcome of the methodology is a rock type volume, showing the lateral and horizontal variation of rock types, and probability volumes for each rock types.

In chapter 3, I propose methods to improve seismic imaging of seismogenic faults in Oklahoma. Oklahoma has witnessed 34000 earthquakes within the last decade. Majority of the earthquakes are attributed to wastewater injection into the subsurface formation. The injection causes decrease in effective stress leading to reactivation of critically stressed faults causing earthquakes. Recent studies attribute some of the earthquakes to hydraulic fracturing also. A hydraulic fracturing completion near a critically stress fault can reactivate it leading to earthquakes. Oklahoma Geological Survey (OGS) has cataloged hundreds of faults in Oklahoma using published literature and contribution from industry. While in some parts of Oklahoma earthquakes occur along the previously mapped faults, in many places in Oklahoma a lack of correlation is observed between the earthquakes and the mapped faults. This is likely because the previously mapped faults are located within the sedimentary layers, while earthquakes mainly

occur within the crystalline basement or due to incomplete fault mapping. The incomplete fault mapping can be due to lack of data or faults overlooked by interpreter due to low vertical offset. STACK (Sooner Trend Anadarko Basin Canadian Kingfisher counties) is one of the regions which has witnessed increase in earthquake, but the earthquakes does not show correlation with mapped faults. We propose a method called band-limited multispectral coherence and aberrancy to image the seismogenic faults. The faults mapped using the seismic attributes show excellent correlation with the earthquakes laterally and horizontally.

REFERENCES

Energy Information Administration 2019. The Distribution of U.S. Oil and Natural Gas Wells by Production Rate.

CHAPTER 2 A METHOD TO COMPENSATE FOR MIGRATION STRETCH TO IMPROVE THE RESOLUTION OF AVO, S-IMPEDANCE (Z_S) AND DENSITY (P)

Swetal Patel and Kurt J. Marfurt
The University of Oklahoma, School of Geosciences.
This paper is submitted to SEG journal Interpretation and is under 2nd revision.

ABSTRACT

Because of their improved leverage against ground roll and multiples, as well as the ability to estimate azimuthal anisotropy, wide-azimuth 3D seismic surveys are now routinely acquired over most resource plays. For a relatively shallow target, most of these surveys can be considered to be long offset as well, containing incident angles up to 45°.Unfortunately, effective use of the far offset data is often compromised by noise and NMO (or more accurately, prestack migration) stretch. The conventional NMO correction is well known to decrease the frequency content and distort the seismic wavelet at far offsets, sometimes giving rise to tuning effects. Most quantitative interpreters work with prestack migrated gathers rather than unmigrated NMO-corrected gathers. However, prestack migration of flat reflectors suffers from the same limitation called migration stretch. Migration stretch leads to lower S-impedance (Z_S) and density (ρ) resolution estimated from inversion, misclassification of AVO types, and infidelity in AVAZ inversion results. We describe a matching pursuit algorithm commonly used in spectral decomposition to correct the migration stretch by scaling the stretched wavelets using a wavelet compensation factor. The method is based on hyperbolic moveout approximation. The corrected gathers show increased resolution and higher fidelity amplitudes at the far offsets leading to improvement in AVO

classification. Correction for migration stretch rather than conventional "stretch-mute" corrections provides three advantages: (1) preservation of far angles required for accurate ρ inversion, (2) improvement in the vertical resolution of Z_S and ρ volumes, and (3) preservation of far angles that provide greater leverage against multiples. We apply our workflow to data acquired in the Fort Worth Basin and retain incident angles up to 42^o at the Barnett Shale target. Comparing Z_P, Z_S, and ρ of the original gather and migration stretch compensated data, we find an insignificant improvement in Z_P, but a moderate to significant improvement in resolution of Z_S and ρ. The proposed method is valid for reservoirs, which exhibit dip no more than 2^o. Consistent improvement is observed in resolving thick beds, but the method might introduce amplitude anomalies at far offset for tuning beds.

INTRODUCTION

The normal moveout (NMO) correction is to align the non-zero offset traces with the zero-offset trace, allowing the reflection events to be stacked and facilitating subsequent AVO, AVAZ, or prestack impedance inversion analysis. Prestack migration improves on the simple NMO correction by reducing CMP smear, placing dipping reflectors in a more accurate location, and properly focusing diffractions. In the time domain, both NMO-corrections and prestack migration are usually implemented on a sample-by-sample basis leading to distortion of the non-zero incident angle traces, where the amount of distortion increases with increasing source-receiver offset to depth ratio. Such distortion leads to a decrease in frequency and increased waveform interference at the farther incident angles. Such distorted gathers lead to a decrease in the resolution of inversion products and may create misleading results. The Aki and Richards' (1980) approximation to Zoeppritz's (1919) equations shows that P-impedance (Z_P), S-impedance (Z_S), and density (ρ) can be estimated from the "PP" reflected waves as a function of incident angle (Figure 1). At near

angles, the PP reflection is only sensitive to changes in Z_P. At farther angles, the PP reflection is sensitive to changes in all three parameters, Z_P, Z_S, and ρ. Because no converted waves are measured, the loss in resolution for inverted Z_S and ρ can be partially attributed to migration stretch.

As early as 1972, Buchholtz (1972) quantified the degree of stretch with offset introduced by the NMO correction. To avoid the negative impact of stretch on the final stack, it was desirable to perform simple mute on the part of the far offset data that was unacceptably distorted. Since muting decreases the stack fold and causes a loss of information contained in the far offset data, Rupert and Chun (1975) proposed a Block Move Sum (BMS) method to address the stretching problem without muting. In this method, the seismic data are treated as blocks, and a single dynamic correction is applied to a block of data to eliminate stretching. Unfortunately, overlapping of adjacent blocks at far offsets introduced wavelet replication and discontinuities. Shatilo and Aminzadeh (2000), Brouwer (2002), and Masoomzadeh et al. (2010) improved upon Rupert and Chun's (1975) BMS technique. Hicks (2001) combined Radon, and spatial Fourier transforms to develop a new transform to remove the NMO stretch from the NMO corrected CMP gather. Trickett (2003) discussed the shortcomings of the Hicks (2001) method and proposed an alternative method which directly generates stretch-free stacked data using an inversion process. However, this technique does not provide an NMO stretch corrected CMP gather required for AVO analysis and prestack inversion. Hilterman and Van Schuyver (2003) developed an approach for wide-angle data based on prestack migration using event-based travel time to correct the NMO stretch for a specified interval. The limitation with their method is that only the specified interval is truly flat in the gathers after the processing.

Estimating the correct vertical shift of the non-zero incident angle traces for a particular reflection is the most crucial task in NMO correction. Chen et al. (2018) describe the two most common means of estimating vertical shift in NMO-correction techniques: (1) using velocities based on user-defined travel time equations, and (2) computing local time shifts of adjacent non-zero offset traces with respect to the zero offset trace (Fomel, 2007). The first technique computes the NMO correction using velocity spectra (Taner and Koehler, 1969).

Chen at al. (2018) uses the second technique to align the data by applying a Dynamic Time Wrapping (DTW) algorithm to find the time shifts based on the similarity of the adjacent traces in the prestack time-migrated gather. The process does not require a velocity spectrum; however, a velocity model is needed for the implied reverse NMO correction. The process also fails for interfering events and thin-layer waveform interference.

Careful velocity analysis is a critical tool in discriminating between primaries, reflectors, and crossing coherent events (such as multiples). Stretch correction processes developed by Perroud and Tygel (2004), Abedi and Riahi (2016), Shatilo and Aminzadeh (2000), Zhang et al. (2013), Faccipieri et al. (2019) and Abedi et at. (2019) require velocity or travel time analysis prior to the application of the process. Zhang et al. (2013) compute a wavelet-by-wavelet rather than sample-by-sample NMO correction, where the reflection events are modeled using a matching-pursuit wavelet-based decomposition algorithm. Mutlu and Marfurt (2015) used the workflow described by Zhang et al. (2013) and combined with prestack structure-oriented filtering provided S- impedance volumes exhibiting the same vertical resolution as the P-impedance volumes. The major drawback of the Zhang et al. (2013) algorithm is the complexity and computational intensity.

In this paper, we combine Zhang et al.'s (2013) reverse NMO and non-stretch NMO processes into one, significantly decreasing algorithmic complexity and increasing speed. For the

same dataset, Zhang et al.'s (2013) methods completed both the processes of reverse NMO and non-stretch NMO in 14 hours, whereas the method mentioned in this paper completed in approximately 8 hours. We begin with a detail description of our migration-stretch compensation algorithm. We then show the effect of migration stretch on AVO and prestack inversion computed from a simple elastic synthetic model. Next, we apply our algorithm to prestack migrated data volume acquired over a Barnett Shale reservoir in the Fort Worth Basin, Texas, showing the improvement in resolution of Z_S and ρ over those obtained by inverting the uncorrected data. Finally, we conclude with a summary of the value and limitations of this workflow.

METHODOLOGY

NMO and NMO stretch

Travel time for a flat and homogeneous isotropic layer is hyperbolic. If the vertical two-way travel time is given by T_0, then the travel time for the same reflector at source-receiver offset h for velocity v_{RMS} is approximated by

$$t(T_0, v_{\mathrm{RMS}}, h) = \left\{T_0^2 + \left[\frac{h}{v_{\mathrm{RMS}}(T_0)}\right]^2\right\}^{1/2}, \tag{1}$$

where each trace is defined by a fixed offset, h. The change in two-way travel time t as a function of the zero-offset travel time T_0 is simply

$$\frac{\partial t}{\partial T_0} = T_0\left\{T_0^2 + \left[\frac{h}{v_{RMS}(T_0)}\right]^2\right\}^{-1/2} < 1. \tag{2}$$

Wavelet decomposition

Let us assume an earth model is composed of a suite of J reflections at time t_j and reflection coefficient r_j. Let's also assume that the time-varying source wavelet can be represented by Morlet wavelets of the form $w(f_j, \phi_j)$, where f_j and ϕ_j are the frequency and phase of the wavelets. The seismic trace without the NMO correction is then

$$u(t^{\mathrm{RNMO}}) = \sum_{j=1}^{J} r_j \delta\left(t_j^{\mathrm{RNMO}}\right) w\left(f_j, \phi_j\right) \tag{3}$$

where the superscript RNMO indicates that the times are measured after reverse NMO. After a conventional sample-by-sample NMO correction, these wavelets are stretched, which leads to lower frequencies in the far-offset data for non-interfering events.

Compensation for migration stretch

Rather than starting with uncorrected gathers, most interpreters start with prestack time migrated data volumes. In addition to placing the data in a more appropriate lateral position, prestack migration also reduces CMP smear. Velocity analysis of smeared CMP gathers over dipping reflectors results in velocities that are erroneously high. Deregowski (1990) recognized this shortcoming and developed a workflow (called the Deregowski loop) whereby prestack time-migrated gathers are subjected to reverse NMO, from which velocity spectra are computed and analyzed. These new velocities can then be used by NMO to align the gathers better (e.g., Mutlu and Marfurt, 2016) or, in Deregowski's (1990) case, to remigrate the data.

Let's assume our migration velocities were (1) sufficiently accurate, and (2) provided by the service company along with the migrated gathers. Applying reverse NMO followed by NMO using the same velocity reproduces the original migrated data. Zhang et al. (2013) applied reverse NMO and then constructed a wavelet decomposition on the reverse-NMO corrected gathers, where

each wavelet (rather than each sample) was subjected to a subsequent NMO correction, thereby eliminating NMO stretch.

Our modification is simple, but also quite efficient. Here, we represent each migrated trace using the same method as in equation 3:

$$u(T_0) = \sum_{j=1}^{J} r_j \delta\left(T_{0j}\right) w\left(f_j, \phi_j\right) \tag{4}$$

where the time axis T_0 indicates that the reflection event times have already been migrated (or NMO-corrected). We can compensate for migration stretch by computing a wavelet compression factor, c, by mapping T_{0j} to t_j, using equation 5:

$$c_j = \frac{1}{T_{0j}} \left\{ T_0^2 + \left[\frac{h}{v_{RMS}(T_0)} \right]^2 \right\}^{1/2} > 1, \tag{5}$$

which can then be used to scale the wavelets in equation 4 and generate the compensated trace

$$u_{\text{comp}}(T_0) = \sum_{j=1}^{J} r_j \delta\left(T_{0j}\right) w\left(c_j f_j, \phi_j\right) \tag{6}$$

The input to the algorithms consists of migrated seismic gathers and either an RMS or migration velocity model (Figure 2). The output is a volume of gathers that have been compensated for migration stretch.

Implementation of matching pursuit in stretch compensation

Matching pursuit (e.g., Castagna and Sun, 2006; Liu and Marfurt, 2007) works in a manner similar to high-resolution Radon transforms, where the spectra of the strongest events are estimated and subtracted from the trace first, followed by iterative estimation and subtraction of successively weaker events. Since their original introduction, more general basis pursuit

algorithms that use a suite of nonorthogonal basis functions as well as L1 norms applied to the data misfit and L1 constraints to minimize the number of components has been found to be quite effective in improving the resolution of seismic data (e.g., Puryear and Castagna, 2011). We provide an updated description of the relatively simple matching pursuit algorithm used by Liu and Marfurt (2007).

We begin the analysis by assuming that each seismic time trace, *u(t)*, is band-limited and can be represented by a linear combination of *J* Morlet wavelets, *w*:

$$u(t) = \sum_{j=1}^{J} r_j \cdot w(t - t_j, f_j, \phi_j) + n(t), \tag{7}$$

where r_j, t_j, f_j, and φ_j represents the reflection coefficient, center time, peak frequency, and phase of the j^{th} wavelet centered about time t_j, and $n(t)$ represents noise. In general, reflected events from thin beds, gradients in impedance, discontinuities in attenuation (1/Q), and inaccurately migrated events, as well as dispersed events, will have arbitrary phases even if the source wavelet is zero phase. For this reason, we construct our basis functions using a suite of complex Morlet wavelets (Figure 3). We calculate the center time t_j of each candidate wavelet using the peaks in the instantaneous envelope and the wavelet frequency, f_j, using the instantaneous frequency at the envelope peak. The temporal behavior of a zero-phase Morlet wavelet is given by:

$$w(t, f_j) = \exp(-t^2 f_j^2 \cdot 2\ln 2) \cdot \cos(2\pi f_j t), \tag{8}$$

while its magnitude spectrum is given by:

$$\overline{w}(f, f_j) = \frac{\sqrt{\pi / \ln 2}}{f_j} \cdot \exp\left[-\frac{\pi^2 (f - f_j)^2}{2\ln 2 \cdot f_j^2} \right]. \tag{9}$$

To efficiently solve for both the magnitude and phase of each wavelet, we use the Hilbert transform, and form both an analytic data-trace, *U(t)*:

$$U(t) = u(t) + iu^H(t)\,, \tag{10}$$

and a table of analytic complex wavelets:

$$W(t, f_j) = w(t, f_j) + iw^H(t, f_j)\,, \tag{11}$$

where w are symmetric cosine wavelets given by equation 8, and w^H are antisymmetric sine wavelets (Figure 3).

The first step in the matching pursuit algorithm is to precompute a finely sampled wavelet dictionary that spans the bandwidth of the input data. The analytic analog of equation 7 then becomes:

$$U(t) = \sum_j A_j \cdot W_j(t - t_j, f_j) + N(\mathrm{t})\,, \tag{12}$$

where

$$e(t) = \|U(t)\|\,, \tag{13}$$

$$A_j = r_j e^{i\phi_j}\,, \tag{14}$$

and where $e(t)$ is the instantaneous envelope of the seismic trace, and r_j and φ_j represents the magnitude and phase of the complex wavelet W_j. Our objective is to minimize the energy of the residual analytic trace, *R(t)*, defined as the squared difference between the analytic seismic trace and the matched wavelets:

$$\|R(t)\|^2 = \left\| U(t) - \sum_j^J [A_j W_j (t - t_j, f_j)] \right\|^2 . \quad (15)$$

If we were to attempt to estimate all wavelet coefficients in one iteration, we would write equation 15 in matrix form and simply solve the normal equations:

$$\mathbf{A} = [\mathbf{W^H W} + \varepsilon \mathbf{I}]^{-1} \mathbf{W^H U} \quad (16)$$

where W=[$W(t,f_1),W(t,f_2),\ldots,W(t,f_m)$] is a vector of wavelets centered of known frequency at each known envelope peak, $\mathbf{A} = (A_1, A_2, \ldots A_m)$ is a vector of unknown complex wavelet amplitudes, I is the identity matrix and ε is a small number which makes the solution stable. For seismic data, A will be a complex-symmetric banded matrix, with the bandwidth proportional to the number of samples used to define the lowest frequency wavelet used, and therefore amenable to an efficient solution. Liu's (2006) provides a graphical image of equation 15, where the black and red curves represent the real part and imaginary parts of the complex trace and complex wavelets (Figure 4).

Even if we attempted to approximate the seismic data using wavelets centered about all the peaks of $e(t)$, the resulting residual $R(t)$ may still contain weaker seismic events of interest, implying an iterative solution to find them. Alternatively, isolated low amplitude events may represent noise, implying that we may wish to start with the highest amplitude event, estimate and subtract it, and iteratively repeat the process on the residual, giving rise to what is called a greedy matching pursuit algorithm (Mallat and Zhang, 1993). If we consider a thin bed tuning model where the top and bottom reflection events are nearly equal, resolvable, but interfere with each other, it is clear that the greedy matching pursuit will be biased. For this reason, Liu and Marfurt

(2007) provide a parameter, $0 \le \beta \le 1$, that allows the interpreter to adjust how many events k=1, 2, …, K of the J envelope peaks are used in each iteration. Specifically,

$$k = \begin{cases} j \quad \text{if } e_k \ge \beta \underset{j}{MAX}\left(e_j\right) \\ null \text{ if } e_k < \beta \underset{j}{MAX}\left(e_j\right) \end{cases}, \tag{17}$$

where "null" indicates that that event is not used. The iteration continues until either an acceptable residual has been reached or if the convergence rate slows down to a level indicating numerical convergence.

To compensate for migration stretch, we simply replace the wavelets given by equation 7 with the "non-stretched" wavelets f_k with compensated wavelets $c_k f_k$ described by equations 5 and 6. We also apply the phase shift occurring in A_j to the real wavelet, w, rather than to the reflection coefficient, r_j:

$$u(t) = \mathrm{Re}\left[U(t)\right] = \mathrm{Re}\left[\sum_{j=1}^{J} r_j \exp\left(i\varphi_j\right) W_j(t - t_j,\, f_j) + N(\mathrm{t})\right] = \sum_{j=1}^{J} r_j w_j(t - t_j,\, f_j, \varphi_j) + n(\mathrm{t})\,. \tag{18}$$

APPLICATION

Results after compensating for migration stretch

We apply the algorithm to a wide-azimuth seismic survey acquired over the Fort Worth Basin. The depth of the Barnett Shale target is approximately 5600 ft while the offset of farthest migrated gather is 10560 ft. The sweep of the vibrator was 120 Hz. The data were prestack time-migrated using a Kirchhoff algorithm. Figure 5a shows an unmuted common reflection point (CRP) gather from the data. Figure 5b shows the migration stretch compensated unmuted CRP gather. Figure 5c shows the data not modeled by the matching pursuit algorithm. The unmodeled

is the uncompensated data. The algorithm compensates for significantly greater amounts of stretch mute, where the default value of 100% will compress correspondingly stretched wavelets by a factor of 2. The unmodeled data is the one stretched above 100%. Figure 5d shows the frequency compensation factor. The compensation factor increases with offset and decreases with depth, such that the far offset data of the shallower zone suffer from more significant stretching. Figure 5b shows an increase in resolution at the farther offsets at the Barnett Shale target at t=1.1 s when corrected for migration stretch.

Data conditioning

Migrated gathers are often contaminated by noise, may require a residual move out, or even muting prior to AVO or prestack inversion analysis. To ascertain changes caused by migration stretch compensation, the same suite of conditioning steps and parameters were applied to both the volumes. First, we applied a seismic mute to remove high amplitude reverberations that overprint the shallow far-offset data. Then we applied a parabolic Radon transform to discriminate between primaries and long period multiples. Next, we suppress the noise crosscutting the reflectors of interest by applying prestack structure-oriented filtering (Zhang et al., 2016; Sinha et al., 2017) using a Lower Upper Median (LUM) filter. Finally, we apply trim statics to align the reflectors better horizontally. Figures 6a and 6b shows the same gathers shown in Figure 5 after data conditioning. Compensating for migration stretch has considerably improved the resolution of the far-offset data. Figure 7 compares the amplitude spectra of original and compensated near-, mid- and far-angle traces. Figure 7a shows that stretch compensation has a limited effect on the amplitude spectrum of near incident angles. Examining the compensation factor in Figure 5d shows only a small factor *C* for near incident angles that increases as the incident angle increases,

which is validated by the increase in high frequencies for the mid and far angle traces (Figures 7b and c).

Effect of stretching on AVO

Zoeppritz's (1919) equations describe the partitioning of the P- and S-wave energy into transmitted and reflected components as a function of incident angle. Figure 1 shows a cartoon of conventional "PP" seismic data acquisition. For flat-layered geology and vertical incidence, almost 100% of the near-offset reflected energy consists of PP reflections. At farther offset, the P wave energy is converted to PP and PS reflections and transmissions, which leads to the PP reflection at far offset sensitive to both Z_S and ρ. Unless we acquire multicomponent data, we do not directly measure the PS reflection events. Rather, it is the sensitivity of the PP reflection events to the incident angle that allows us to invert for Z_S and ρ. The three-term approximation of the Zoeppritz's equations developed by Aki and Richards (1980) show that Z_P, Z_S, and ρ can be estimated from the coefficients (intercept, gradient, and curvature) of the three-term approximation equations which are calculated from 'PP' reflected waves as a function of incident angles (Figure 8). The intercept is the zero-angle reflection coefficient, which is related to the acoustic impedance contrast across the reflector. The gradient is related to both the shear and acoustic impedance contrast across the interface. The third coefficient (curvature), which measures the curvature of the amplitude near the critical angle, is greatly influenced by the density contrast across the interface. Because the offset is small, the recorded seismic wavefield does not suffer from migration stretch. At farther offsets (Figure 1b), the PP reflected event now suffers from migration stretch. Since the farther offset is sensitive to Z_S and ρ, the lower resolution of Z_S and ρ compared to that of Z_P is partially attributed to migration stretch.

Inversion results for reflectors that fall near the tuning frequency are particularly affected by migration stretch, which we demonstrate using the elastic finite-difference model shown in Figure 9. Figure 9a shows a sketch of the model used for modeling migration stretch effect on tuning beds. Z_P of the background model is 6,900 (m/s * g/cm^3). Z_P of both top and bottom events is 7,200 (m/s * g/cm^3) but are 50 m and 150 m thick, respectively. The acquisition consists of 100 receivers and 100 sources spread across 10,000 m offset. The elastic wave propagation was carried out using a Ricker wavelet of 25 Hz peak frequency. The CMP gather was then prestack time migrated (PSTM) to obtain Figure 9b. The stretching causes interference of positive and negative amplitude response of the top and bottom of the event A, which in turn causes resolution loss of event A with offset, which is just above the tuning resolution, disappearing at the farthest offset. Figure 9c shows the applied migration stretch compensation algorithm provides good, but not perfect improvement to thin, tuned event A by broadening the spectrum. The algorithm introduces positive and negative amplitudes at the offset where it was supposed to compensate for stretch to resolve event A. This is because the composite amplitude of those spectral components that fall below thin-bed tuning is incorrectly represented by a composite wavelet with a 90^o phase change. The compensation algorithm then inaccurately represents this part of the spectrum by a broader band but 90^o phase wavelet that falls in the middle of the thin bed. Event B is less effected by stretching because it is significantly thicker than the tuning resolution. The composite amplitude for the better components of the amplitude spectrum is accurately corrected, like the event at 1.1 seconds in Figures 10a and b that are adequately resolved, giving rise to higher positive and negative amplitudes at the farther offsets that previously suffered from destructive interference.

The events in Figure 10a and b show improvement in resolution at far offset after compensating for migration stretch. The reflectors, which gradually disappear at far offset due to

interference of over- and under-lying reflectors caused by stretching appear stronger after the compensation (reflector highlighted by the red and blue lines in Figure 10). Figure 10 shows that such interference causes false amplitude signature at far offset for the reflector bounded by the interfering reflectors, which in turn leads to an inaccurate AVO signature. The positive amplitude event at 1.1 seconds (Figure 10) shows a phase reversal at far offset in the original angle gather. In reality, the phase reversal is caused by interference of negative amplitude reflectors over- and under-lying this positive amplitude event. The compensation causes resolution balancing over the entire reflector, which leads to the appearance of the positive amplitudes at far offset, which was hidden by stretching and interference. We confirm the fidelity of the appearance of amplitude at far offset by comparing original and compensated gather with the forward modeled angle gather (Figure 11). Unlike the modeled angle gather (purple arrow in Figure 11c), the negative amplitude reflector at 1.1 second disappears at far offset due to stretching and interference of overlying and underlying positive amplitudes reflectors (purple arrows in Figure 11a). The stretch compensation algorithm improves the resolution of far offset data leading to the appearance of negative amplitude reflector at far offset as shown by the modeled angle gather data (purple arrow in Figure 11b). Due to balanced resolution, the events appear continuous after stretch compensation as predicted by modeled data (Figure 11c). The stretch compensation also improves amplitude consistency across the offset as predicted by modeled gather (events shown by orange arrow in Figure 11).

Prestack simultaneous inversion

Simultaneous inversion to estimate Z_P, Z_S, and ρ are critical in many resource plays. Z_P and Z_S can be correlated to mineralogy and hence brittleness using ECS or other mineralogy logs, which in turn can map areas that are amenable to hydraulic fracturing. Volumetric estimates of ρ can be correlated to log measurements and core analysis to predict areas that have total organic

carbon. The maximum usable incident angle of 42^o at the Barnett Shale target allowed us to estimate ρ from inversion. Angles beyond 42° were contaminated by strong linear noise from the shallow section; they also fall beyond the critical angle and are not useful for inversion. The inversion of both data volumes was carried out with the exact same parameters. Figures 11a and c show the Z_P estimated from simultaneous inversion of the original prestack migrated and migration stretch compensated gathers, respectively. A good match between the Z_P^{log} and $Z_P^{seismic}$ (impedances measured by well logs and seismic inversion) confirms the fidelity of the inversion (Figure 12b and d). Comparing with well Z_P, we do not see significant improvement in Z_P after stretch compensation.

The difference between $Z_P^{original}$ and $Z_P^{compensated}$ (Figure 12e) highlights the area of significant change. The maximum change in Z_P occurs near the fast rocks (limestone and basement). During prestack inversion, Z_P is not independently estimated from zero offset traces, rather it is calculated from the coefficients of the three-term linear approximation equation. Stretch compensation causes change in the values of those coefficients by changing the AVO response. The AVO is a function of impedance contrast across the reflector. If the contrast is high, the change is AVO before and after compensation will be high (Figure 13). Hence, we observe a maximum change in Z_P near the fast rocks (Caddo, Forrestburg, Ellenberger, and Basement). The change observed in Figure 12e is attributed to change in the AVO response. There is an insignificant change in Z_P after stretch compensation away from the fast rocks.

Figure 14a and c show Z_S from prestack simultaneous inversion for original and compensated gather. The black arrows in Figure 14e highlight the areas of maximum change. These changes can be attributed to both a change in the AVO response and an increase in resolution. The gray arrows indicate areas where an increase in resolution is observed. A

significant increase in resolution is obtained in the shallower zone than the deeper. This is because the wavelet compensation factor applied in the methodology decreases with depth and increases with angle of incidence (Figure 5c). Figure 14b and d shows the change in Z_S near the well. A good match between the well and seismic shows fidelity of the inversion. We do see a significant change in resolution near the well as well as far away from the well; some of them highlighted by grey arrows in Figure 14c.

A maximum usable incident angle of 42^o at Barnett Shale allowed us to invert the prestack data for density during simultaneous prestack inversion. The ρ results for the original and compensated gathers is shown in Figure 15a and c, respectively. The black arrows in the difference volume (Figure 15e) indicate areas near the fast reflectors, where the maximum change in ρ is observed. We attribute these changes to a change in AVO response and an increase in resolution. The gray arrows indicate areas away from the faster reflectors where the change in density is attributed to the increase in resolution. Comparing with the density logs, Figure 15b, and d shows that we observe an overall increase in density resolution. As with the Z_S images, the improvement in resolution is higher for the shallower zone than the deeper zone because the compensation factor is higher for the shallower zone.

LIMITATIONS

The stretch-compensation we use assumes that the stretch from prestack time migration is approximately the same as caused due to NMO. We believe this to be an accurate approximation for most resource plays in North America, such as the Barnett Shale, which exhibits dips no more than 2°. Furthermore, commercial prestack impedance inversion software used by oil company quantitative interpreters often assumes the dip of the reservoir to be relatively gentle. The migration stretch compensation algorithm described here (and most commercial inversion

software) will not work on steeply dipping reservoirs located on salt flanks and other tectonically complex terrains. These data often require prestack depth migration to be imaged appropriately and will require the development of a stretch compensation algorithm based on the kinematics of residual moveout algorithms currently in use. Stretch compensation applied on the 2D elastic response of the model suggest that resolution improvement using bandwidth extension methods based on the location of energy peaks such as matching pursuit (Mallat and Zhong (1992), Matos and Marfurt (2014)) cannot extend the resolution of poorly resolved spectral components. The method incorrectly compensates the composite response of the tuned beds at far offset by a broader band but 90^{o} phase wavelet that falls in the middle of the bed. This introduces false positive and negative amplitudes at offsets, where it is supposed to resolve the bed. A potential solution to this approach is a double spike inversion approach described by Puryear and Castagna (2006).

CONCLUSIONS

In principle, seismic reflections are represented by discrete spikes at reflector boundaries. These spikes are then convolved with the seismic wavelet to provide the seismic trace. Migration assumes each sample of the seismic trace is a potential reflection spike, leading to stretch of the imaged wavelets, which in turn leads to a lower resolution for inverted S-impedance and density. Such stretching may give rise to an apparent phase reversal of the reflectors due to interference of the stretched reflectors bounding it, leading to false AVO signatures and inversion results. We use a matching pursuit algorithm to estimate the location of the reflection's spikes, fit wavelets to the data, and then compensate for migration stretch. Comparison of the amplitude spectrum for near, mid and far angle stack of the original gather and stretch-compensated gathers shows an increase in higher frequencies. Because P-impedance is heavily dependent on the zero angles reflected PP waves, there is an insignificant improvement in P-impedance resolution. In contrast, there is a

significant improvement in resolution for Z_S and ρ in the shallow section and a moderate improvement in the deeper section. The method shows significant improvement for well-resolved beds, but it incorrectly estimates the composite response of tuned beds at the far offset, leading to the addition of false amplitudes.

ACKNOWLEDGEMENT

Thanks to Pioneer Natural Resources Company for providing a license to their seismic data for use in research and education. Thanks to CGG Geosoftware for licenses to their Geoview inversion package. The finite-difference synthetic seismic gathers and migrated results were computed using TesseralPro. Finally, thanks to the sponsors of the AASPI consortium for their guidance and financial support.

FIGURES

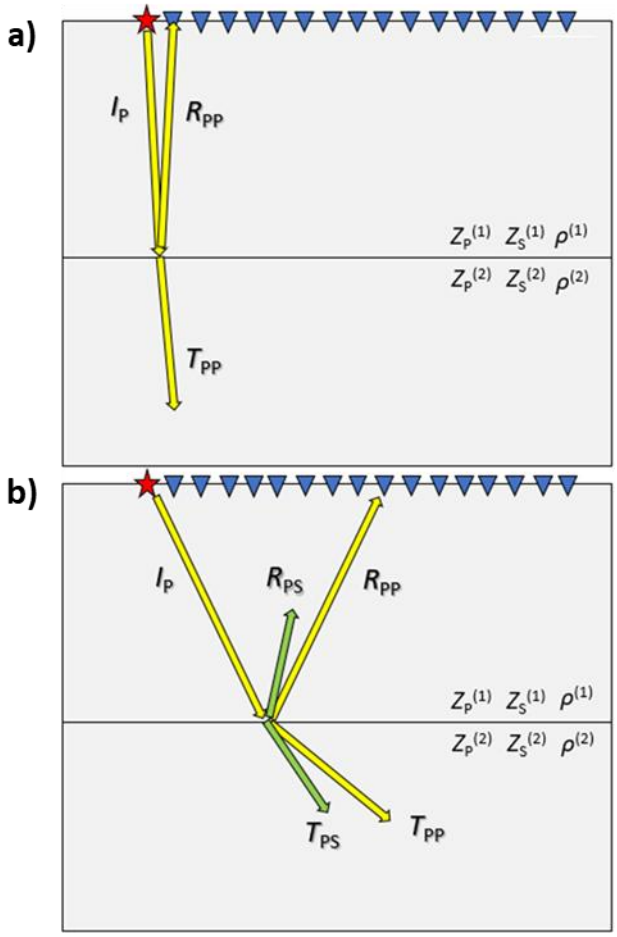

Figure 2-1. Cartoon showing conventional "PP" seismic data acquisition using vertical geophones (on land) or hydrophones (at sea). (a) At near incident angles, P wave generates only PP reflections and transmission. Hence, the near incident angles are sensitive to only Z_P contrast across the interface. At large offset (b), P wave generates both P and S reflections and transmission such that 'PP' reflection energy is sensitive to the Z_S and ρ contrasts across the interface as well. Because the farther offsets suffer from migration stretch, inverted for Z_S and ρ volumes often exhibit lower resolution than the corresponding Z_P volume.

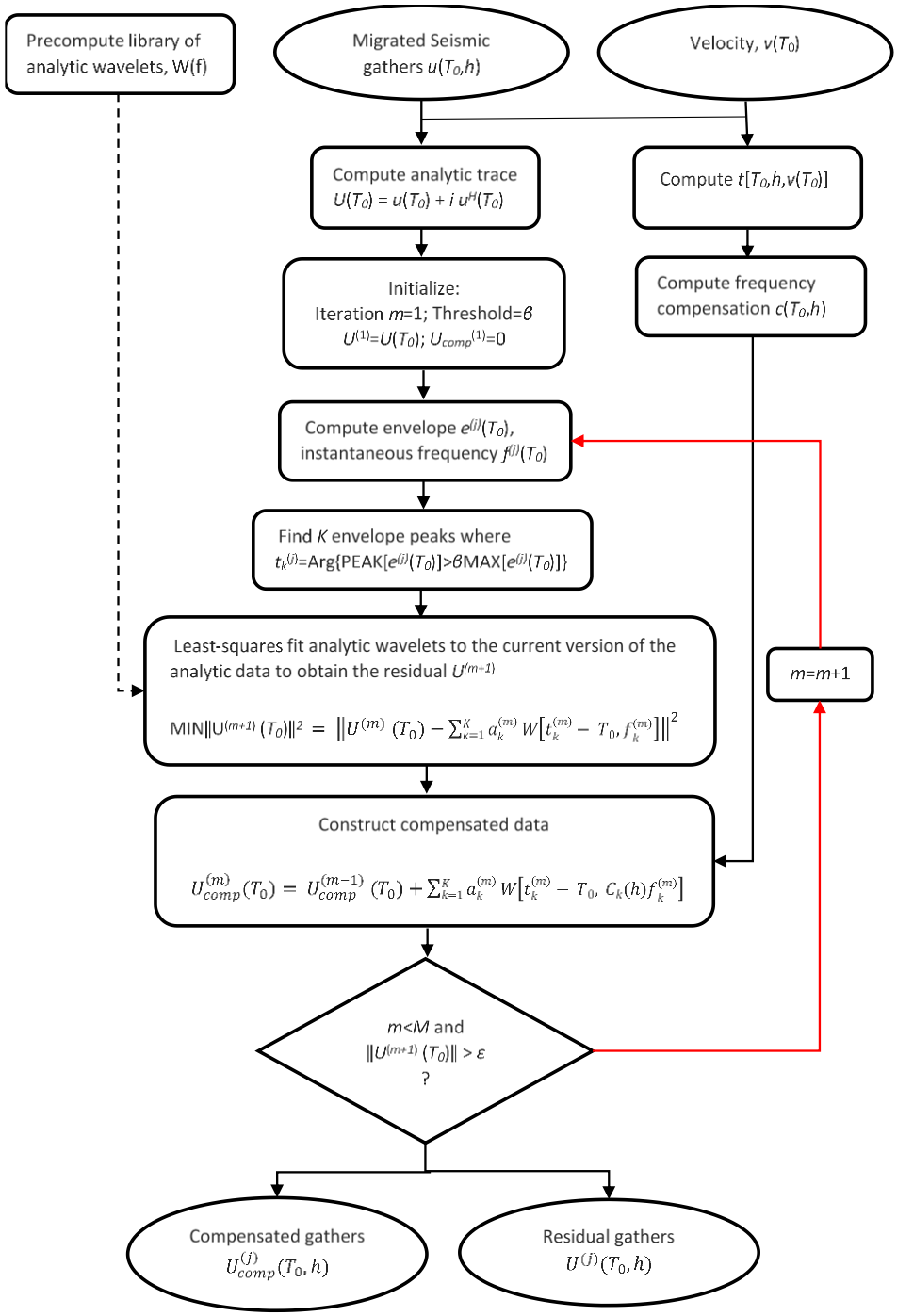

Figure 2-2. Flow chart of the migration stretch compensation algorithm. The input to the program is unmuted prestack time-migrated gathers and the velocities used to migrate the data.

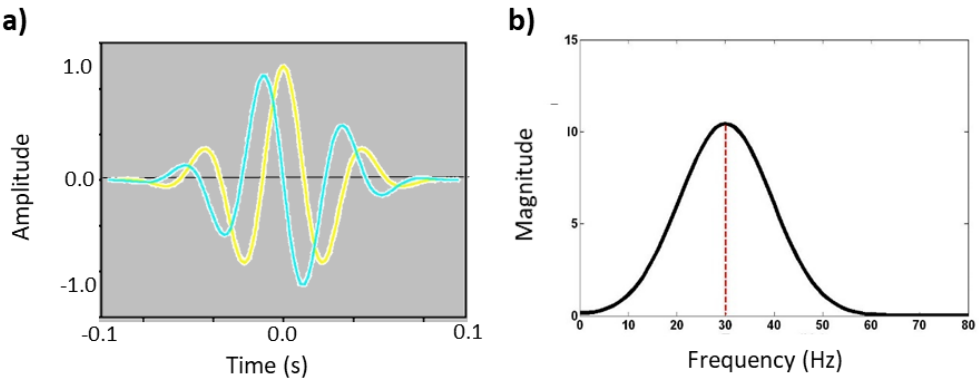

Figure 2-3. (a) A complex 30 Hz Morlet wavelet consisting of a real part or 0° Morlet wavelet (yellow) and an imaginary part 90° Morlet wavelet (cyan). (b) The corresponding magnitude spectrum. (After Liu, 2006).

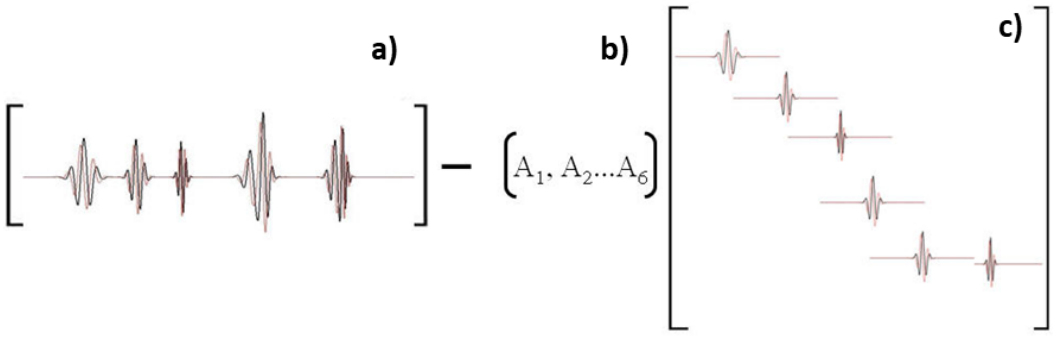

Figure 2-4. (a) A complex seismic trace represented by (b) six complex amplitudes, and (c) six complex Morlet wavelets. The goal of equation 15 is to compute the complex wavelet amplitudes A_j that, when multiplied by W_j and summed, approximate the complex seismic trace in a least-squares sense. (After Liu, 2006).

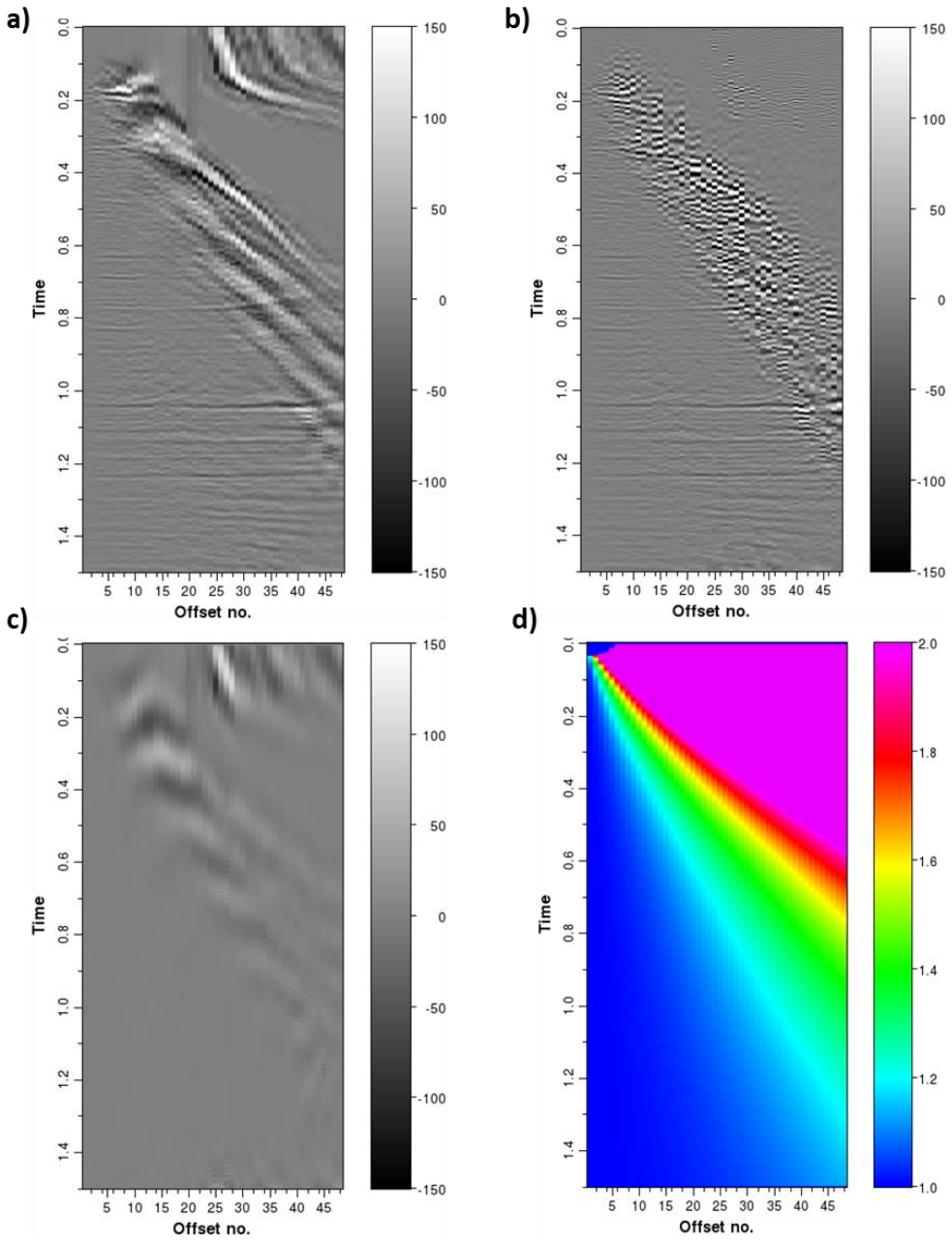

Figure 2-5. (a) The unmuted CRP gather of the data, (b) unmuted migration stretch compensated CRP gather, (c) unmodeled data and, (d) the frequency compensation factor. The compensation factor increases with increasing offset and decreases with increasing time.

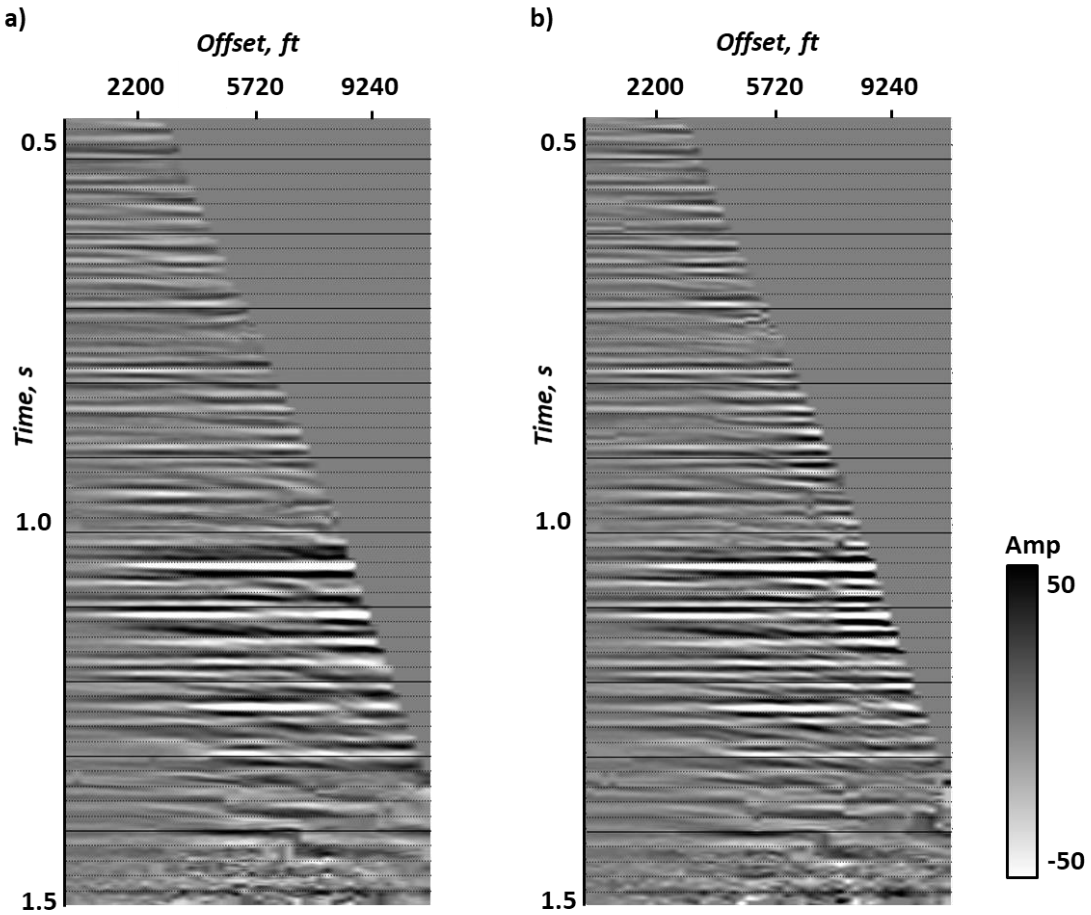

Figure 2-6. The (a) original migrated and (b) stretch-compensated CRP gathers corresponding to Figure 3a and b, but now after data conditioning. The same suite of conditioning steps and parameters have been applied to both data volumes. Note how stretch compensation increased the resolution of the long-offset data, leaving the near-offset unchanged.

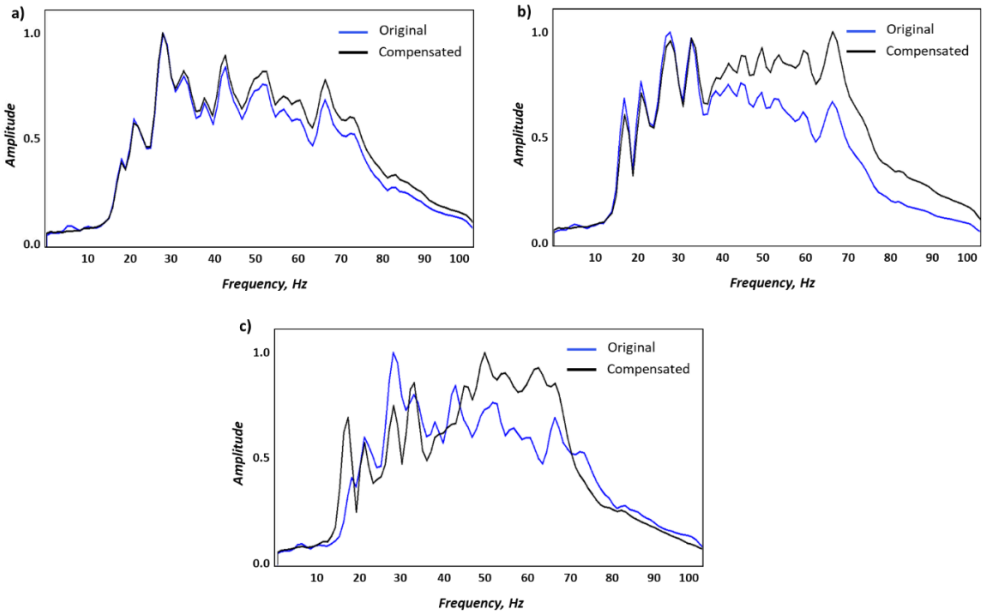

Figure 2-7. Amplitude spectrum of the original and compensated gather for (a) near angle CRP gather (6º-20º), (b) mid angle CRP gather (20º – 34º), and (c) far angle CRP gather (34º-42º). Compensation for migration stretch increases the ratio of high frequency to the overall spectrum.

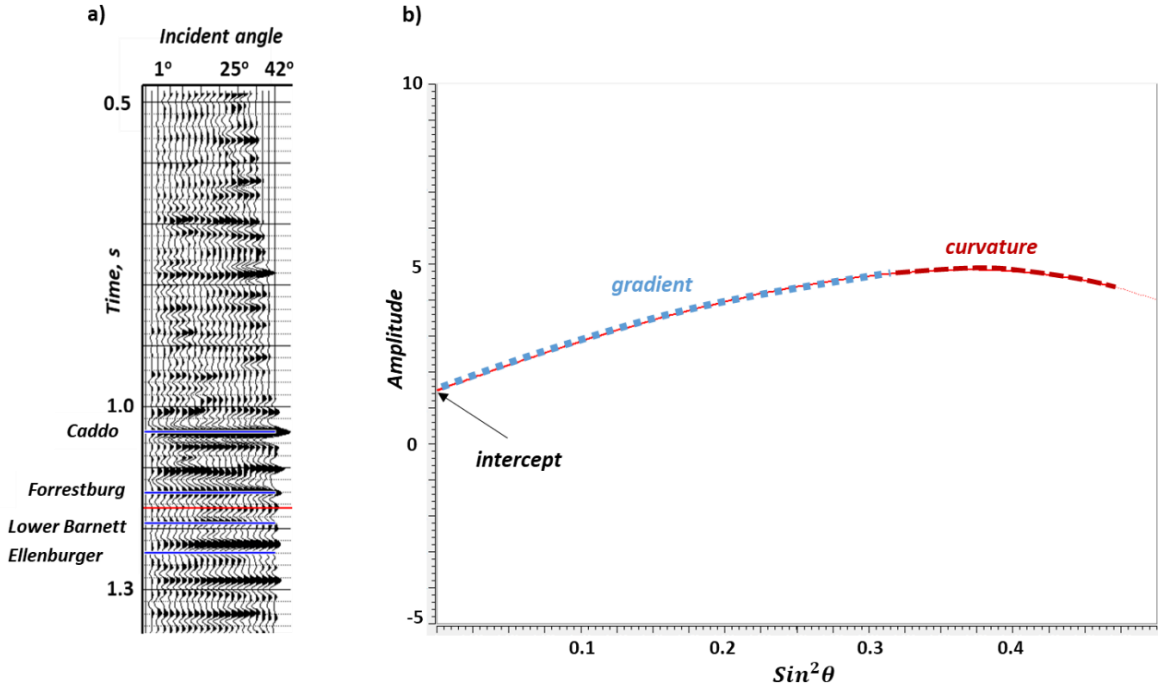

Figure 2-8. (a) The angle gathers corresponding to the compensated gather shown in Figure 4b with reflectors of interest highlighted in blue. (b) The AVO response of the event indicated by the red line in (a). The blue dashed line indicates the approximate AVO gradient. The red dashed line indicates the AVO curvature.

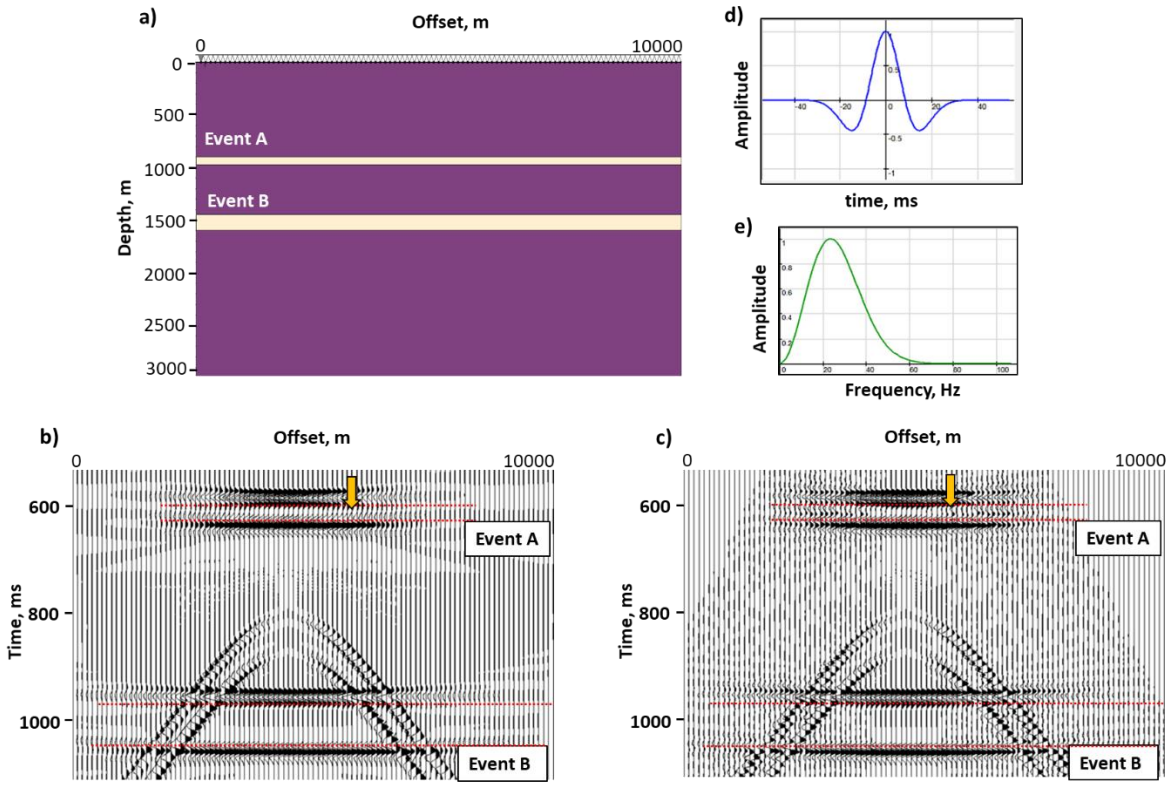

Figure 2-9. (a) A simple model constructed to show the change of tuning with offset. Layer A is 50 m thick while Layer B is 150 m thick. The thickness of the event A is just above the quarter wavelength of source wavelet. The Z_P of both the event is 7200 (m/s * g/cm3), while the Z_P of the background model is 6900 (m/s * g/cm3). (b) Prestack time migrated CMP gather of the 2D elastic modeling response of the model. The yellow arrow indicates the offset where it is challenging to resolve event A due to stretching of the top and bottom reflector of the event. c) Migration stretch compensated CMP gather of the 2D elastic modeling response of the model. The yellow arrow indicates artifacts caused due to incorrect representation of the composite wavelet for the event. Source wavelet (Ricker) in (d) time domain and (e) frequency domain. The red dash lines show the top and bottom of the events. The modeling shows a decrease in the resolution of event A with offset (yellow arrows). The elastic modeling also shows interference of positive (top of event A) and bottom (bottom of event A) negative amplitudes at far offset, leading to the thickness of event A being unresolved at far offset.

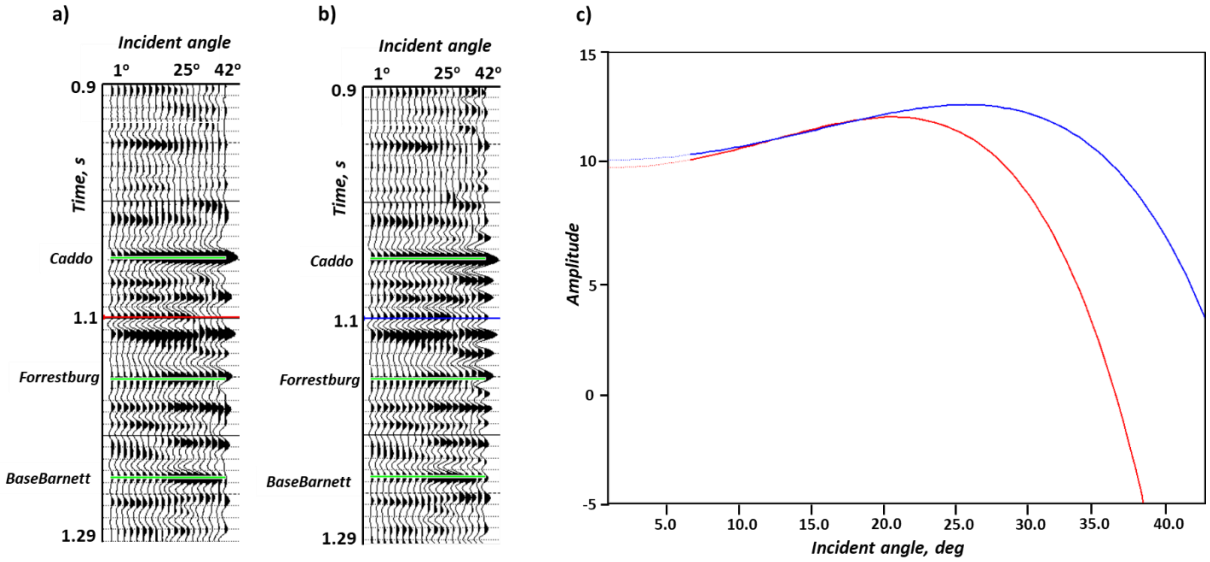

Figure 2-10. Shows the angle gather of (a) original and (b) compensated prestack data with the reflectors of interest highlighted by green lines. (c) The red and blue line shows the AVO curve for original and compensated gather for an event at 1.1 seconds highlighted by red and blue line in (a) and (b) respectively. The AVO curve has been derived using Aki and Richards' three-term approximation equation.

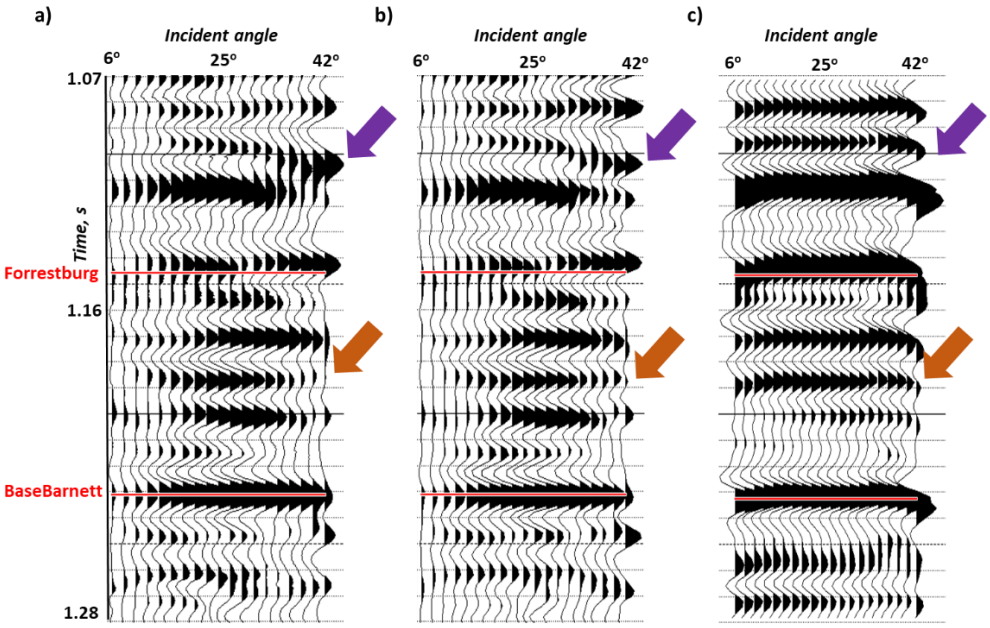

Figure 2-11. a) Shows the original, b) stretch compensated, and c) forward modeled angle gather. The purple arrow in a) shows the far offset gather where two events intersect each other due stretching but are resolved after stretch compensation in b) as shown by forward modeled gather in c). The orange arrow indicates an event where a decrease in amplitude is observed in the original gather, unlike modeled gather, but stretch compensation restores the amplitude at far offset.

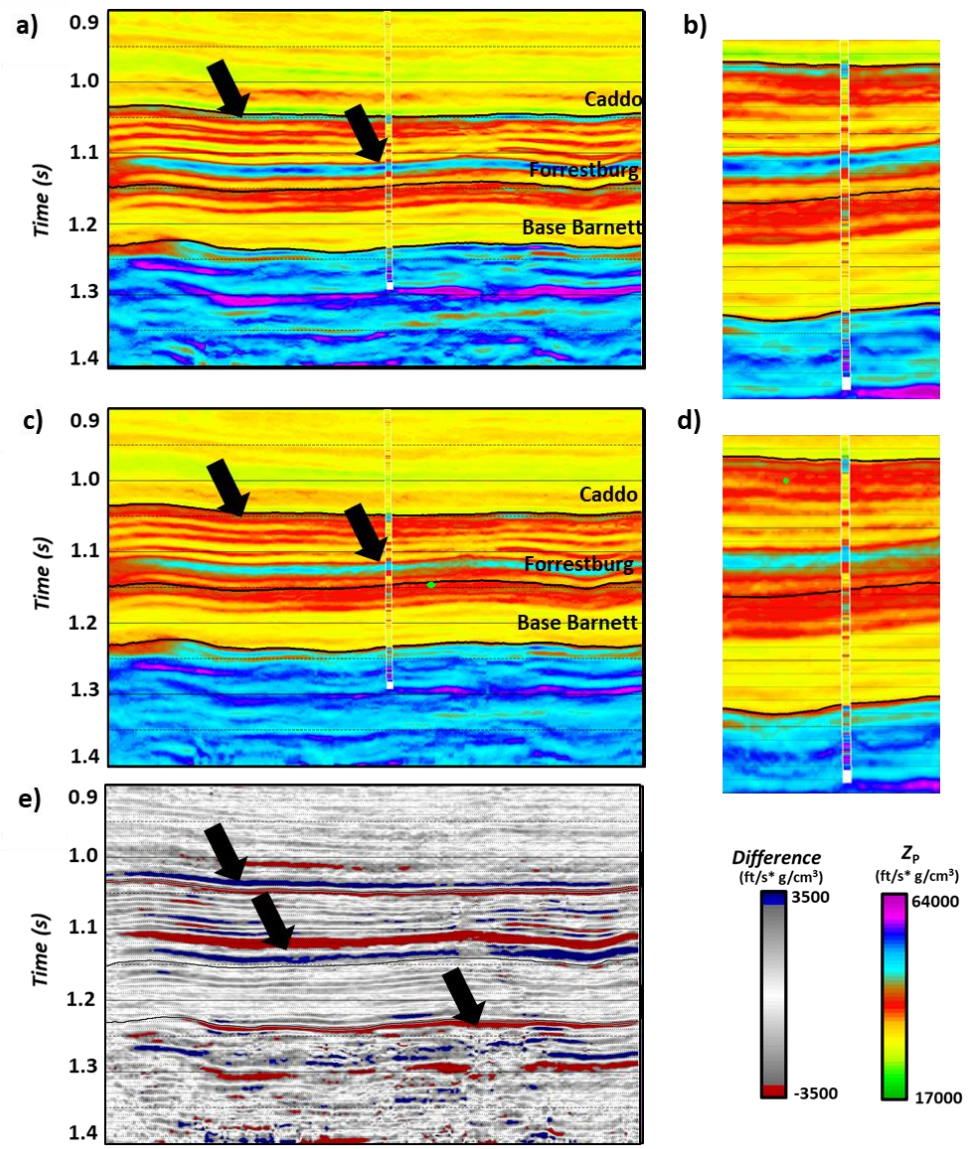

Figure 2-12. Z_P estimated from simultaneous inversion of the (a) original prestack and, (c) migration stretch compensated prestack gathers and e) the difference between (b) and (a) (compensated-original). b) and d) is a close-up view near the well of a) and b), respectively, showing a change in Z_P with respect to well after stretch compensation. Black arrows indicate areas where significant changes in Z_P are observed. An insignificant change is observed in the resolution after compensation.

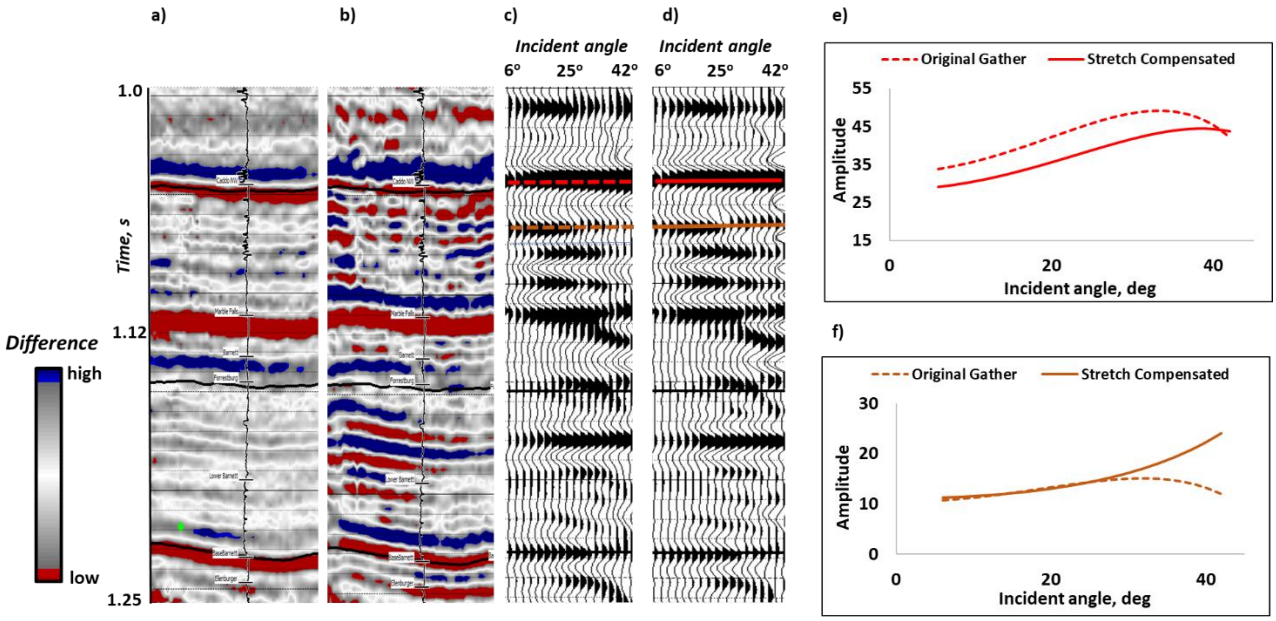

Figure 2-13. The difference between original and stretch compensated a) Z_P (compensated-original), b) ρ (compensated-original). Angle gathers c) original and d) stretch compensated. e) AVO curve of the Caddo formation shown by the red line in c) and d). f) AVO curve of formation shown by the orange line in c) and d). We can observe that a significant change in AVO occurs near the fast rocks. Hence, we see a change in Z_P near the fast rocks. Whereas away from the fast rocks, we do not see a significant change in AVO except the change in curvature above 35^o (orange curve in f)), which is reflected by an insignificant change in Z_P and considerable change in ρ.

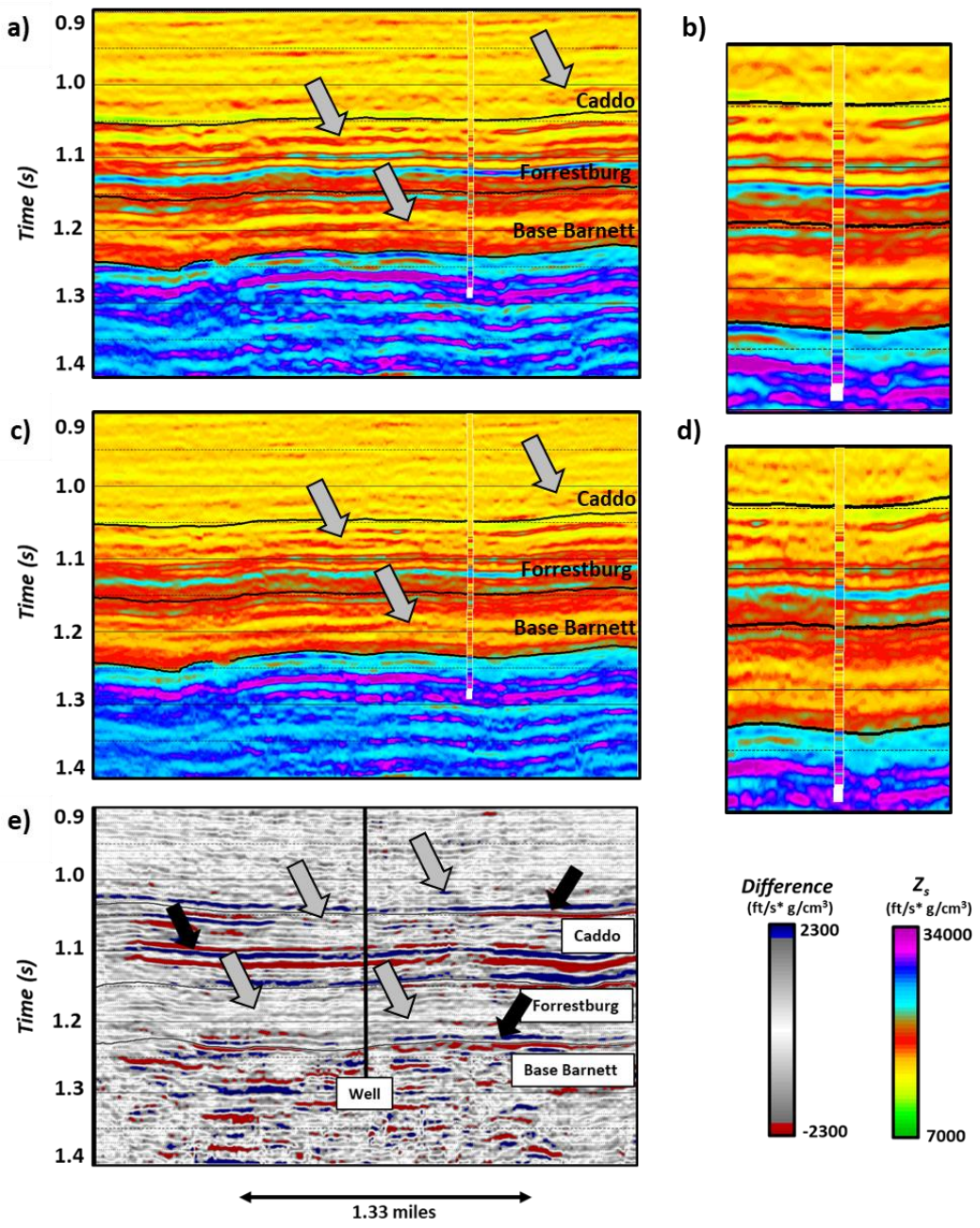

Figure 2-14. Z_S estimated from simultaneous inversion of (a) original prestack gather and, (c) migration stretch compensated prestack gather and e) the difference between (b) and (a) (compensated-original). b) and d) is a close-up view near the well of a) and b), respectively, showing a change in Z_S with respect to well after stretch compensation. The grey arrows show some of the areas of a significant improvement in the resolution of Z_S from the compensation of migration stretch. The black arrows point to the zone where the change in Z_S is observed across the whole reflector. These changes might be due to change in AVO and/or change in resolution.

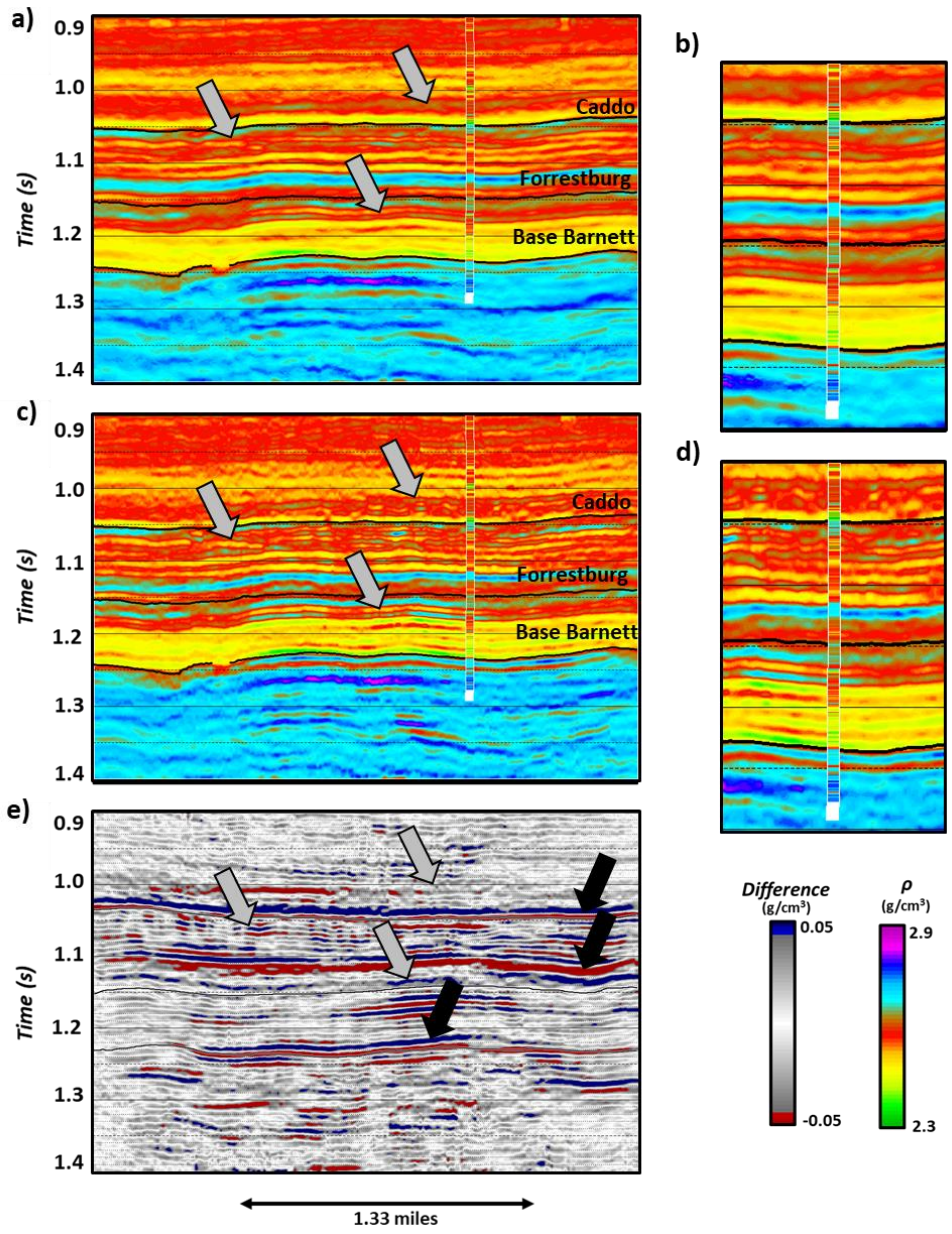

Figure 2-15. ρ estimated from simultaneous inversion of (a) original prestack gather and, (c) migration stretch compensated prestack gather and e) the difference between (b) and (a) (compensated-original). b) and d) is a close-up view near the well of a) and b), respectively, showing a change in ρ with respect to well after stretch compensation. Grey arrows indicate some of the areas of significant improvement in resolution of ρ by compensating for migration stretch. The black arrows point to the zone where the change in Z_S is observed across the whole reflector. These changes might be due to change in AVO and/or change in resolution.

REFERENCES

Abedi, M. M., and M. A. Riahi, 2016, Nonhyperbolic stretch-free normal moveout correction: Geophysics, 81 (6), U87–U95, doi: 10.1190/geo2016-0078.1.

Abedi, M. M., M. A. Riahi, and A. Stovas, 2019. Three-parameter normal moveout correction in layered anisotropic media: A stretch-free approach: Geophysics, 84 (3), C129-C142, doi: 10.1190/GEO2017-0855.1.

Aki, K. L., and P. G. Richard, 1980, Quantitative seismology: W. H. Freeman and Co.

Brouwer, J. H., 2002, Improved NMO correction with a specific application to shallow seismic data: Geophysical Prospecting, 50 (2), 225–237, doi: 10.1046/j.1365-2478.2002.00310.x.

Buchholtz, H., 1972, A note on signal distortion due to dynamic (NMO) corrections: Geophysical Prospecting, 20 (2), 395–402, doi: 10.1111/j.1365-2478.1972.tb00642.x.

Chen, S., S. Jin, L. Xian-Yang, and W. Yang, 2018, Nonstretching normal-moveout correction using a dynamic time warping algorithm: Geophysics, 83 (1), V27-V37, doi: 10.1190/GEO2016-0673.1.

Deregowski, S. M., 1990, Common-offset migrations and velocity analysis: First Break, 8, 224-234, doi: 10.1190/1.9781560801917.

Faccipieri, J. H., T. A. Coimbra, T.A. and R., Bloot, 2019, Stretch-free generalized normal moveout correction: Geophysical Prospecting, 67 (1), 52-68, doi: 10.1111/1365-2478.12702.

Fomel, S, 2007, Velocity-independent time-domain seismic imaging using event slopes: Geophysics, 72 (3), 139-147, doi: 10.1190/1.2714047

Hicks, G. J., 2001, Removing NMO stretch using the Radon and Fourier- Radon transforms: 63rd Annual Conference and Exhibition, EAGE, Extended Abstracts, A-18.

Hilterman, F., and C. Van Schuyver, 2003, Seismic wide-angle processing to avoid NMO stretch: 73rd Annual International Meeting, SEG, Expanded Abstracts, 215–218. doi: 10.1190/1.1817768

Liu, J., 2006, Spectral decomposition and its application in mapping stratigraphy and hydrocarbons: Ph. D. dissertation, University of Houston.

Liu, J., and K. J. Marfurt, 2007, Instantaneous spectral attributes to detect channels: Geophysics, 72 (2), P23-P31. doi: 10.1190/1.2428268

Mallat, S., and S. Zhong, 1992, Characterization of signals from multiscale edges: IEEE Transactions on Pattern Analysis and Machine Intelligence, 14 (7), 710–732. doi: 10.1109/34.142909.

Mallat, S. and Z. Zhang, 1993, Matching pursuit with time-frequency dictionaries: IEEE transactions in signal processing, 41 (2), 3397-3415. doi: 10.1109/78.258082

Masoomzadeh, H., P. J. Barton, and S. C. Singh, 2010, Nonstretch moveout correction of long offset multichannel seismic data for subbasalt imaging: Example from the North Atlantic: Geophysics, 75 (4), R83–R91, doi:10.1190/1.3443579.

Matos, M., and K. J. Marfurt, 2014, Complex wavelet transform spectral broadening: 83rd Annual International Meeting, SEG, Expanded Abstracts, 1465–1469, doi:10.1190/segam2014-1369.1.

Mutlu, O., and K. J. Marfurt, 2015, Improving seismic resolution of prestack time-migrated data: Interpretation, 3 (4), T245-T255. doi: 10.1190/INT-2014-0260.1

Perroud, H., and M. Tygel, 2004, Nonstretch NMO: Geophysics, 69 (2), 599–607, doi: 10.1190/1.1707080.

Puryear, C., and J. P. Castagna, 2008, Layer-thickness determination and stratigraphic interpretation using spectral inversion: Theory and application: Geophysics, 73 (2), R37-R48. doi: 10.1190/1.2838274.

Rupert, G. B., and J. H. Chun, 1975, The block move sum normal moveout correction: Geophysics, 40 (1), 17–24. doi: 10.1190/1.1440511.

Shatilo, A., and F. Aminzadeh, 2000, Constant normal-moveout (CNMO) correction: A technique and test results: Geophysical Prospecting, 48 (3), 473–488, doi: 10.1046/j.1365-2478.2000.00190.x.

Sinha, S., K. J. Marfurt, D. Devegowda, R. Pires de Lima, and S. Verma, 2017, Seismic inversion based SRV and reserves estimation for shale plays: SPE Annual Technical Conference and Exhibition, SPE-187137-MS. doi: 10.2118/187137-MS.

Taner, M. T., and F. Koehler, 1969, Velocity spectra-digital computer derivation applications of velocity functions: Geophysics, 34 (6), 859–881, doi: 10.1190/1.1440058.

Trickett, S., 2003, Stretch-free stacking: 73rd Annual International Meeting, SEG, Expanded Abstracts, 2008–2011. doi: 10.1190/1.1817723

Zhang, B., K. Zhang, S. Guo, and K. J. Marfurt, 2013, Nonstretching NMO correction of prestack time-migrated gathers using a matching-pursuit algorithm: Geophysics, 78 (1), U9-U18. doi: 10.1190/geo2011-0509.1.

Zhang, B., T, Lin, S. Guo, O. E. Davogustto, and K. J. Marfurt, 2016, Noise suppression of time-migrated gathers using prestack structure-oriented filtering: Interpretation, 4 (2), SG19-SG-29. doi: 10.1190/INT-2015-0146.1

Zoeppritz, K., 1919, Uber Erdbebenwellen VII b: Gottinger Nachrichten, 66-84.

CHAPTER 3 SPATIAL DELINEATION OF ROCK TYPES IN THE MERAMEC FORMATION BY INTEGRATING CORE AND SEISMIC MEASUREMENTS, KINGFISHER/LOYAL COUNTY, ANADARKO BASIN

Swetal Patel [1], Ishank Gupta [2], Jing Fu [2], Dr. Ali Tinni [2], Kurt. J. Marfurt [1], Dr. Carl Sondergeld [2] and Dr. Chandra Rai [2]*

[1]*School of Geosciences, The University of Oklahoma*
[2]*Mewbourne School of Petroleum and Geological Engineering, The University of Oklahoma*

This paper is planned to be submitted to SEG journal Interpretation special section "The STACK Play in Oklahoma"

ABSTRACT

The Mississippian-age STACK area of Oklahoma is one of the more important new resource plays in North America and consists of multilevel objectives including mudrock, siltstone, and carbonate reservoirs, some of which are self-sourced and all of which require hydraulic fracturing to produce commercial quantities of oil. The efficacy of the fracturing relies on whether the created fracture network drains from producible rock types. We integrated data at both core and seismic resolution scales to map the spatially exhaustive lateral and vertical variation of the rock types for this new play. We measured porosity, permeability, saturated P- and S- wave velocity and density in the lab at 2 ft intervals on the cores. We then defined rock types corresponding to engineering flow units based on porosity and permeability measurements. We mapped these rock types against alternative elastic property cross plots, including P-impedance, S-impedance, Poisson's ratio, LamdaRho, and MuRho. P- and S- impedance are the only two

independent elastic properties measured on the core samples. The other elastic properties are calculated from these two measurements. Hence, the rock types showed equal sensitivity to all the elastic property pairs. We observe a 30% difference between core and seismic elastic values, only part of which can be attributed to dispersion. We address this discrepancy between core and surface seismic elastic values by simple linear scaling. We found that P-impedance and Poisson's ratio core measurements were easier to scale linearly to the corresponding seismic frequency measurements. Once scaled, we used Bayesian classification to map the P-impedance and Poisson's ratio rock type template defined by the core measurements to the same elastic parameters measured by prestack seismic inversion. As we move away from the six cored wells deeper into the basin and more distal from the shelf, we encounter P-impedance/Poisson's ratio pairs not seen in core, resulting in areas where the rock type is "unknown". The seismically predicted rock types show an excellent correlation at the well locations and provided stratigraphically reasonable images away from the wells, suggesting that as more wells are cored, these unknown rock types can be classified.

INTRODUCTION

The Meramec formation is considered one of the principal reservoirs in the STACK (Sooner Trend Anadarko [Basin] Canadian Kingfisher counties) play of Oklahoma. Long lateral horizontal wells combined with hydraulic fracturing lead to economic exploitation of the formation beginning in 2010 and continuing until the present day. Optimum exploitation of the Meramec requires the well lateral and hydraulic fractures to intersect rock types/fluid flow units with a large hydrocarbon storage capacity, which we call 'sweet spots.' The fluid flow heterogeneity of the formation in the Anadarko Basin can be attributed to two factors: 1) deposition of the formation during the transition from decreasing thermal subsidence to flexure subsidence mechanisms

foreshadowing the tectonic events of the Pennsylvanian period (Miller et al., 2019), and 2) change in depositional environment from shallow-water carbonates sediments in the North (Rogers, 2001; Pranter et al., 2016) to the deep water siliciclastic carbonate sediments in the south of the Anadarko Basin (Price et al., 2017).

A rock type/fluid flow unit is a representative volume of rock that has predictable and consistent fluid flow influencing petrophysical properties within the representative rock volume (Amaefule et al., 1993). These rock types are generally mapped using porosity and permeability cross plots, where Amaefule et al. (1993) introduced the concept of Flow Zone Indicator (FZI) to map the rock types. Winland and Pitman (1992) introduced a rock type classification based on Hg injection measurements while Kaale (2010) defined rock types based on similar values of porosity, FTIR mineralogy, Hg injection capillary pressure, and TOC measured on 1600 ft of core. Using these kinds of measurements as input, Lee et al. (2002) defined rock types using principal components and model-based cluster analysis while Gupta et al. (2017) used unsupervised clustering algorithms. We map the rock types using the Flow Zone Indicator (FZI) technique developed by Amaefule et al. (1993).

In this paper, we delineated the lateral and spatial distribution of rock types over a 477 square mile area. The process requires the integration of core and seismic data. Since the resolution of these data is different, extending the rock type classification from core to seismic scale can be challenging. Furthermore, petrophysical properties such as permeability used in defining the rock types are not directly measured by surface seismic data. For these reasons, the process of extending these rock types from the core to seismic requires statistical analysis of their response in seismic attribute space. The number of rock types discriminated in the seismic attribute space might be

less than one defined at core scale due to different sensitivity of petrophysically derived rock types in seismic attribute space.

Such classification can be achieved through statistical, automated clustering, or pattern recognition algorithms (Grana et al., 2016). Da Veiga and La Ravalec (2012) and Schlanser et al. (2014) used maximum likelihood criteria to classify facies. Wang et al. (2014) used a supervised classification technique to classify different kinds of shales in unconventional resource plays. Avseth et al. (2001) used Mahalanobis quadratic discriminant analysis to classify lithofacies derived on the geological description. Grana et al. (2016) compare the Bayesian classification and expectation-maximization method used in facies classification. Mukerji et al. (2001) and Doyen (2007) details the process of extending the classification at log or core scale to seismic scale. In this paper, we classify the core derived rock types in the seismic elastic domain using a Bayesian classification scheme.

Bayesian classification links rock types with the elastic parameters through conditional probability and prior probability functions. Such a scheme measures interpretation uncertainty in rock type classification extended to the seismic scale. A classical approach in computing conditional probabilities assumes that the elastic properties are normally distributed (Gaussian) for each facies. Such an assumption is not always valid and can lead to the misclassification of outliers and the inability to mathematically map a nonlinear trend in the hyperplane separating the facies. In contrast, a non-parametric classification such as the kernel density function used here, does not assume the data distributions to be Gaussian. For this reason, the computed conditional probabilities are less affected by outliers, give fewer outliers, and map non-linear trends in the discriminant hypersurface (Gonzalez et al., 2000). Gonzalez et al., (2000) find that although non-parametric conditional probability density estimation can be computationally exhaustive is high-

dimensional space, it works well for two or three attributes; implying that is appropriate to use in computing .conditional probabilities from geomechanical properties derived from surface seismic data such as P-impedance and Poisson's ratio.

We begin our paper with an overview of Meramec play in the study area. We then use results from laboratory core measures to construct a suite of rock types that are correlated to flow unit zones. Next, we correlate the elastic parameters estimated from surface seismic data to those measured in core, allowing us to transfer our rock type template to the 3D seismic volume. Using this rock type template, we then construct 3D probability volumes for each rock type for the entire survey. We conclude with a discussion of the advantages and limitations of this workflow.

STUDY AREA

The study area is in the STACK area of the Anadarko Basin (Figure 1) which covers four counties of central Oklahoma. With depths to the basement of 30,000-40,000 ft, the south-dipping asymmetric Anadarko Basin along the northern flank of Wichita uplift, is the deepest phanerozoic sedimentary basin in North America, shallowing out into the Anadarko Shelf to the north and east. The formation and evolution of the Anadarko Basin have strongly influenced the sedimentation rate, erosion, depositional environment, reservoir seal, and source rocks from Cambrian through Permian time. Perry (1989) divides the history of the Anadarko basin into four significant periods: (1) Precambrian igneous activities leading to crustal consolidation, (2) development of the Southern Oklahoma Aulacogen during Early Cambrian through Middle Cambrian, (3) development of the southern Oklahoma trough during Late Cambrian through Early Mississippian and (4) initiation of an independent Anadarko Basin during Late Mississippian time. The Basin continued to experience crustal unrest till the late Pennsylvanian period leading to the formation of Wichita Mountains (the southwest margin of the Anadarko Basin), the Arkoma Basin, Ouachita

Mountains (southeast Oklahoma) and the Nemaha Uplift and fault zone (Figure 1). The geometry of the facies deposition is mainly attributed to tectonic events during the Cambrian Period (Higley et al., 2014).

The Meramec formation was deposited during the Mississippian period approximately 320 to 360 million years ago when the continental shelf was covered by a shallow warm sea. The shallow marine Meramec was deposited during second-order marine transgression and subsidence. A higher-order sea level cyclicity is also visible at a finer scale. Physiochemical conditions varied from the shallow water in the north to deeper water in the south leading to a variety of lithofacies deposition. Duarte (2018) suggests that the deposition of the Meramec was controlled by a range of tectonic activities; hence, the source of sediments of these lithofacies is only partly understood. Based on the core descriptions, Miller (2019) reports five different lithofacies in the study area: mudstone, argillaceous siltstone, argillaceous, calcareous siltstone, silty limestone, and calcareous siltstone. While important in understanding the depositional environment, completion engineers are less interested in geologic lithofacies and more interested in rock types that define porosity and permeability properties used to define flow zone indicators. Nevertheless, the lateral change in geologic lithofacies as we extend further from the shelf will modify our rock type template based on elastic parameters measured in core and from surface seismic data.

CORE-DERIVED ROCK TYPES

The purpose of rock typing is to integrate various petrophysical properties, including porosity, permeability, X-Ray Fluorescence (XRF) mineralogy, ultrasonic velocities, and water saturation measured in the lab or calculated using logs. When mapped to seismic data, rock type volumes across the study area can help select sweet spots for future well locations as well as select optimum zones for completion. We mapped the rock types using the Flow Zone Indicator (FZI)

technique on core porosity and permeability data measured in six cored wells. Figure 2 indicates that the Meramec consists of three different rock types, which we denote as RT1, RT2, and RT3. Figure 3 shows the variability in porosity, permeability, as well as carbonate and clay content for these rock types. Average porosity and clay content decrease from rock type 1 to rock type 3, while the average permeability and carbonate content increase from rock type 1 to rock type 3 (Figures 3a and 3b). The increasing carbonate content from rock type 1 to rock type 3 suggests increasing calcite cement as the cause of the decreasing porosity trend from rock type 1 to rock type 3 (Figures 3a and 3c). Figures 3a and 3d suggest higher clay content is correlated with higher porosity.

During the course of this study, the mineralogy, porosity and permeability measurements were made on six cored samples but experimentally exhaustive P-wave, S-wave and density measurements as a function of confining pressure on saturated vertical core samples were made only for one of the core. The P-wave, S-wave and density measurements were then used to calculate other elastic moduli. An increase in Young's modulus from rock type 1 to rock type 3 implies a corresponding increase in brittleness (Figure 3f). A similar trend is observed in brittleness calculated using elastic parameters using Rickman et al.'s (2008) scaled Poisson's ratio and Young's Modulus. For our data, rock type 1 is the clay-rich porous ductile rock, while rock type 3 is calcite-rich less porous brittle rock. Rock type 2 is a transitionary between rock types 1 and 3. Although rock type 3 is more permeable than rock type 1, all wells will be hydraulically fractured, such that the greater hydrocarbon storage capacity of more porous rock type 1 makes it the preferred drilling target.

Although rock type 1 is relatively ductile, seismic brittleness calculated using elastic parameters such as proposed by Rickman et al. (2008) ignores the stress dependence of moduli and might behave brittlely under in-situ stress conditions. More important, operator experience

has shown no problems in hydraulic fracturing and producing from rock type 1 in the Meramec formation. Hence, in the next sections, we combine seismic data with these core derived rock types to map the spatial variation of rock type 1, where the lateral and horizontal variation of rock type 1 will define “sweet spots” in the Meramec formation.

THE SENSITIVITY OF ROCK TYPES TO ELASTIC PROPERTIES

The rock types mentioned in the previous section were derived from porosity and permeability measurements. Although P-wave impedance is often well correlated with porosity, the seismic experiment is quite insensitive to lateral changes in permeability. Mapping these rock types using seismic data therefore requires correlating both rock types and surface seismic data to a measurement common to the two analyses. Elastic parameters derived using prestack seismic inversion is a natural choice since measured the same elastic parameters for each laboratory sample measured for porosity and permeability. Ultrasonic P-wave velocity, S-wave velocity**,** and density were measured as a function of confining pressure on vertical core sample**s** at every 2 ft for one of the wells. The core samples were saturated with dodecane at a confining pressure of 5000 psi. P- and S-wave velocities measured on vertical core plugs at confining pressure of 4000 psi were used to calculate P-impedance (Z_P^{core}), S-impedance (Z_S^{core}), V_P/V_S^{core}, Lambda-rho ($\lambda\rho^{core}$), Mu-rho ($\mu\rho^{core}$), Youngs modulus-rho ($E\rho^{core}$) and Poisson's ratio (ν^{core}). The same elastic parameters were independently estimated at the seismic scale ($Z_P^{seismic}$, $Z_S^{seismic}$, $V_P/V_S^{seismic}$, $\lambda\rho^{seismic}$, $\mu\rho^{seismic}$, $E\rho^{seismic}$, and $\nu^{seismic}$) using prestack seismic inversion. Initial analysis suggested that classifying all three rock types in the Z_P – Z_S elastic domain (Figure 4a) resulted an unacceptably high prediction error. . Similar unsatisfactory results were obtained in cross plots between Z_P and ν, $\lambda\rho$ and $\mu\rho$, Z_P and V_P/V_s, $E\rho$ and ν.

The confusion matrix obtained using Bayesian classification indicate that there is only a 42% probability of correctly estimating RT2 (Table 1). RT1 and RT2 are clay-rich high porosity low permeable rocks, while RT3 is a calcite-rich low porosity high permeable rock. We therefore combined RT2 with RT1 and called the new rock type RT1*. Such a combination reduced the dimensionality of the problem to classifying only two rock types in the elastic domain: high porosity RT1* and high permeability RT3. The cross plot between Z_P and Z_S shows improved discrimination between RT1* and RT3 (Figure 4b). Also, such a combination of rock types increases the probability of correct estimation using the corresponding seismic volumes (Table 2).

Figure 5a-d shows cross plots of the typical elastic domains used to separate lithologies or rock types. RT1* and RT3 are sensitive to all the parameters. Some classification algorithms, such as artificial neural networks, require the construction of a linear discriminator. In this case, better separation can be obtained by applying nonlinear transformations to the input data (e.g. converting Z_P and v to $\lambda\rho$ and $\mu\rho$). The kernal density function allows irregular boundaries and hence can classify the rock types in for different domain choices with a similar probability. In this paper, we choose the P-impedance and Poisson's ratio domain to classify RT1* and RT3.

COMPENSATING ELASTIC PROPERTIES FOR FREQUENCY DEPENDENCE

The core elastic properties were measured using ultrasonic (~200-600 MHz) frequencies, while the seismic elastic properties were measured using seismic (~10-60 Hz) frequencies, with the background velocity model constructed using P- and S-wave sonic logs measured at 2000 Hz frequencies. Even though both measurements are independent of each other, they follow a similar trend along with depth, implying fidelity of the seismic inversion to the core measurement (Figure

6). However, the core properties exhibit higher values than the corresponding seismic elastic properties, which we attribute to velocity dispersion and spatial sampling. The average difference between core and seismic Z_P and v relative to the core is 25% (+/- 7%) and 0.9% (+/- 16%), respectively.

Velocity dispersion is a phenomenon wherein velocity is a function of frequency or wavelength. An elastic wave propagates with a different velocity at different frequencies or wavelengths. Hence, the elastic properties measured at seismic and ultrasonic scale will have the same trend but different values. Since the recognition of the phenomenon, its effect on different frequency bands ranging from seismic (10-100 Hz) to sonic (1000-10,000 Hz) to ultrasonic frequency (1 MHz) has been well documented. Stewart at al., (1984), Hornby et al., (1995) and Schmitt., (1999) discuss the change in velocity due to dispersion effect at seismic and sonic frequencies. Murphy et al., (1986), Best et al., (1997), Duranti et al., (2005) and Hofmann (2006) discusses dispersion effects at sonic and ultrasonic frequencies. Hornby et al., (1995) showed that in sands, the difference in velocity measured with a sonic tool and in the lab was only 3%. However, Hoffman (2006) states that this difference can be as high as 15% in shales. Suarez-Rivera et al., (2001) have seen as much as 45% change in P-velocity between sonic and ultrasonic measurements. Duranti et al. (2005) made velocity measurements on shale samples. They observed almost no dispersion effect until 1000 Hz. The maximum effect was observed at ultrasonic frequencies. The difference in P-wave between ultrasonic and sonic was 30% for a wave traveling perpendicular to the fabric and 28% for a wave traveling parallel to the fabric. Azra (2010) measured velocity as a function of frequency for different shales as well as sandstone rocks. The pressure at which these measurements were made is not reported. A significant difference of 32% was observed for P-wave passing through TGShale1 at sonic and ultrasonic frequencies. The

Meramec formation show as much as 32% variation in P-wave velocity between seismic and ultrasonic frequencies. Since Meramec is argillaceous, calcareous siltstone, such a high variation in P-wave velocity with frequency is possible due to dispersion.

In order to use our core-based template for subsequent Bayesian classification of the seismic inversion elastic measurements, we need to first account for the variation of elastic properties with frequencies. We do not correct for dispersion effects through a model; instead, we scale core and seismic elastic properties through a simple linear transform.

Figure 7 shows the cross plots of core elastic properties against the similar properties extracted along the well from seismic inversion. As expected, the core values are higher than those at the lower frequency seismic scale. We used a simple linear transform for each acoustic parameter and found that $\lambda\rho$, ν, Z_S, and $\mu\rho$ show a high variation along the best fit line. The transform is not linear, which will cause an error in Bayesian classification. $\mu\rho$ shows the same scaling as Z_S. $E\rho$ shows better scaling opportunities than all acoustic properties except Z_P. We ultimately chose Z_P and ν to be the best domain to scale our rock type template for use in Bayesian classification. The best linear transform was observed for Z_P since most of the points clustered around the best fit line. ν required a minimum correction to scale core to seismic measurements (Figures 7a and e). Z_P^{core} and ν^{core} were scaled to seismic frequencies using linear transforms (equations shown in Figures 7a and e). Figures 8a and b show the same cross plots as Figures 7a and e but after scaling.

CONSTRUCTING A ROCK TYPE TEMPLATE FOR USE WITH 3D SEISMIC DATA

Once the elastic parameters have chosen and scaled, the rock types need to be classified in the elastic domain. We use a Bayesian classification scheme to classify the rock types. In Bayesian classification, we compute conditional probabilities and a prior probabilities of rock types using core/log measurements to yield the probability of occurrence of rock types in each seismic voxel:

$$\boldsymbol{P}\left(\boldsymbol{R_i}\middle|\frac{\boldsymbol{Z_p}}{\boldsymbol{v}}\right) = \frac{\boldsymbol{P}\left(\frac{\boldsymbol{Z_p}}{\boldsymbol{v}}\middle|\boldsymbol{R_i}\right)\boldsymbol{P}(\boldsymbol{R_i})}{\boldsymbol{P}(\frac{\boldsymbol{Z_p}}{\boldsymbol{v}})}\ , \tag{1}$$

where, $\boldsymbol{R_i}$ is the i^{th} rock type/classes (in our case RT1* and RT3), $\boldsymbol{P}(\boldsymbol{R_i})$ is the prior probability of the rock types, $\boldsymbol{P}(\frac{\boldsymbol{Z_p}}{\boldsymbol{v}})$ is the probability of having the specific value of elastic parameters (Zp, ν) regardless of the class, $\boldsymbol{P}\left(\frac{\boldsymbol{Z_{pP}}}{\boldsymbol{v}}\middle|\boldsymbol{R_i}\right)$ is the conditional probability that we have a specific value of the combination of Z_P and v given rock type $\boldsymbol{R_i}$, and $\boldsymbol{P}\left(\boldsymbol{R_i}\middle|\frac{\boldsymbol{Z_{pP}}}{\boldsymbol{v}}\right)$ is the "a posterior" probability that we have rock type $\boldsymbol{R_i}$ given a value of the combination of Z_P and v.

Since the rock types were already defined from the core measurements, the prior probability of the rock types was calculated by dividing the number of points into each rock type by the total number of 87 core measurement. **P(RT1*)** was 0.54, and **P(RT3)** was 0.47. $\boldsymbol{P}(\frac{\boldsymbol{Z_p}}{\boldsymbol{v}})$ can be calculated by summing the products of the conditional probabilities and prior probabilities of all classes. The conditional probabilities $\boldsymbol{P}\left(\frac{\boldsymbol{Z_p}}{\boldsymbol{v}}\middle|\boldsymbol{R_i}\right)$ can be calculated using a Probability Density Function (PDF). In our case, the probability density was calculated from the core data (Figure 9a). Figure 9b shows the confidence of predicting the rock types based on conditional PDFs shown in Figure 9a.

The histogram and PDFs showed in Figures 9c, and d suggest that the distribution of the elastic property is not Gaussian. Hence a non-parametric statistic is required to solve for the conditional probability, $\boldsymbol{P\left(\frac{Z_p}{v}\middle|R_i\right)}$**.** We use kernel density estimates of the points in each class to calculate the conditional probabilities. A kernel is a weighting function used to calculate the density functions of variables. Once we have calculated the conditional and prior probabilities, the probabilities of rock type occurrence in each seismic voxel in the 3D seismic volume are calculated using equation 1. The class of rock types to which each seismic voxel away from the well belongs is estimated using a decision rule. Since each seismic voxel away from the well has a value of Z_P and v,

If $\boldsymbol{P\left(\frac{Z_p}{v}\middle|RT1^*\right)\ P(RT1^*) > P\left(\frac{Z_p}{v}\middle|RT3\right)P(RT3)}$, then the Z_P and v pair at the voxel belongs to class *RT1** , or

If $\boldsymbol{P\left(\frac{Z_p}{v}\middle|RT3\right)\ P(RT3) > P\left(\frac{Z_p}{v}\middle|RT1^*\right)\ P(RT1^*)}$ then the Z_P and v pair at the voxel belongs to class *RT3.*

Similar calculations for each voxel estimate the probability of each rock type in the entire seismic volume. Some voxels exhibit Z_P - v pairs not encountered in our core and will be poorly represented by either rock type kernel density function. To better represent the uncertainty in our predictions, we construct a third, "unknown" rock type.

RESULTS

The rock types were estimates over an area of 477 square miles between the top of the Meramec and the top Woodford in the Anadarko Basin using Bayesian classification. Zones of rock type 1* with more than 80% probability were considered to be sweet spots. Figure 10a shows

a proportional slice 40% below the Meramec and Woodford tops through the predicted rock type volumes. Channels seen by other seismic attributes such as coherence and spectral decomposition (Patel and Marfurt, 2019) are also highlighted by the rock types. The N-S flowing channels are filled with mainly RT3, indicating that they are more calcite rich lower porosity, and high permeability compared to the surrounding flood plain, which consists of RT1*. Production data (not shown) indicate that the best rock type is RT1*, which has higher storage capacity but less natural permeability than RT3. Figure 10b shows a vertical cross-section along line AA' through the rock type volume. The predicted rock types on from the 3D surface seismic data show a perfect match at the well location. At this location, rock type RT1* spreads in the middle of the Meramec sandwiched by the over- and underlying rock type RT3. The black arrows in Figures 10a and b indicate zones of unknown rock type, where the Z_P - v pairs were not represented by the core. The presence of unknown rock type increases as we move away from the six cored wells used in constructing our rock type template. Studies by Miller at al. (2019) based on over 1000 triple combo wells showed a lateral change in geologic lithofacies with proximity to the shelf. Figure 10c and d show the uncertainty associated with the prediction calculated using equation 1. We obtain a high probability of predicting RT1* at the center of the zone of interest and RT3 at the bottom. Hence, the middle zone of the Meramec at this location is considered the most productive.

CONCLUSIONS

The Meramec of the STACK play can be represented by five geologic lithofacies based on the geological description of core and three rock types based on porosity and permeability core measurements. The core measurements provide sparse, very localized information. Optimum exploitation of the formation requires the prediction of these rock types away from previously drilled wells. To address this issue, we constructed a 3D probability estimate of the rock types that

can be used in well planning and completion design. We constructed a Bayesian rock type template based on the shared elastic Z_P and ν measurements, which was then applied to the 3D seismic Z_P and ν volumes. Classifying the three rock types measured porosity and permeability space in the laboratory two the two-dimensional Z_P and ν space shared by the laboratory measurements and surface seismic data increased uncertainty in the prediction. Hence, the three rock types were regrouped into two – a higher porosity, lower permeability rock type, and lower porosity, higher permeability rock type. Because of dispersion and effective media effects, the ultrasonic acoustic properties of the core samples showed differences in absolute value compared to the lower frequency seismic measurement extracted along the well. We compensated for these differences by using a linear transform to match the rock physics template to our seismic data. Using Bayes' theorem to estimate the probability of each rock type at each seismic voxel we found excellent predicted rock types at the six cored locations. In addition, the rock types delineate channels on the proportional slice seen on geometric attributes and spectral decomposition. The study suggests that most of the high porosity rocks are lying at the center of the reservoir sandwiched between the high permeable rocks. The center of the reservoir is considered to be a sweet spot zone since high porosity rocks are hypothesized to provide higher storage of hydrocarbons. We were not able to predict a rock type at all voxels in the seismic volume. Such shortcomings arise for two reasons: 1) prediction from only one well data is insufficient to sample spread of seismic elastic parameters, and 2) there may be additional rock types in the unknown zones have different porosity, permeability, Z_P and ν than used to define the three rock types used in this study. Elastic property analysis of other core measurements suggests that that changes in lithofacies as we extend further from the self-causes the variation of elastic expression of rock types both vertically and laterally. Ideally, we should create one probability density function by combining probability functions from

multiple core measurements spread across the study area using inverse distant weighing functions. Using the inverse distant weighted probability function in the Bayes theorem should eliminate the unpredictable zone and improve estimates.

ACKNOWLEDGEMENT

We thank Marathon Oil Company for their financial support and license to their proprietary data to conduct this research effort. The lead author specifically wishes to thank Mr. Chris McLain for sharing his geologic insight as well as providing critical mentorship throughout the duration of this project. All core measurements were conducted in the University of Oklahoma Mewbourne College of Earth and Energy's Integrated Core Characterization Center (IC3).

FIGURES

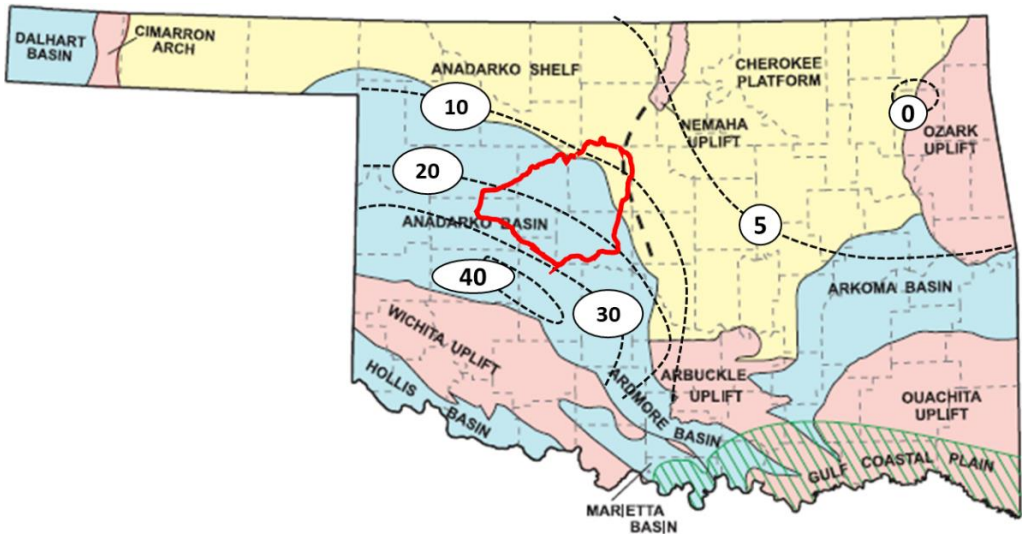

Figure 3-1. Map showing locations of the different basins in Oklahoma. The Anadarko Basin extends from northwestern to central Oklahoma. The red line indicates the Sooner Trend Anadarko Canadian Kingfisher (STACK) play of Oklahoma. The black dashed line shows contours of the top of Precambrian and Cambrian Basement rocks in thousands of feet. (Figure modified from Johnson, 2008).

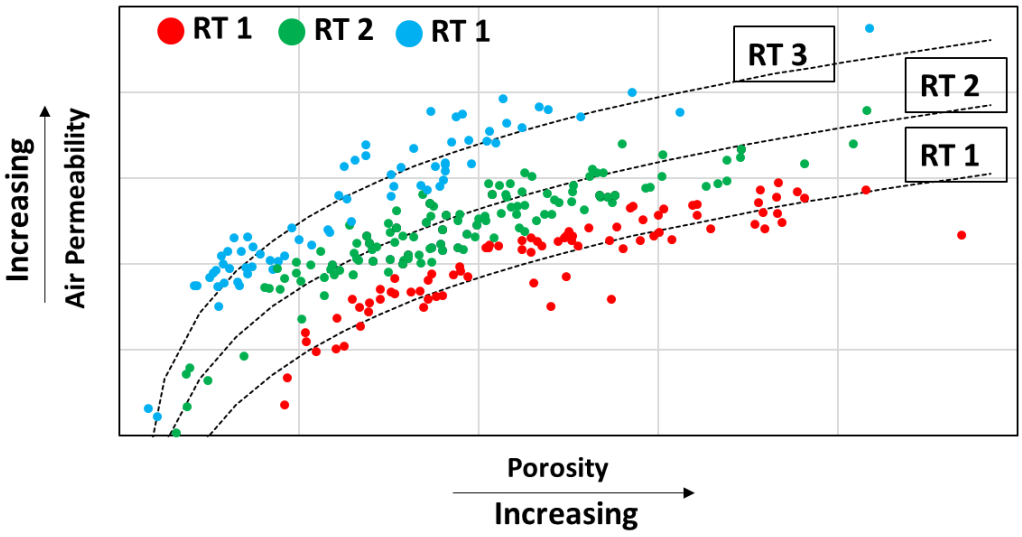

Figure 3-2. Cross plot between porosity and permeability measured on six cored wells. The dotted lines represent different flow zone indicator (FZI) values. We have defined three rock types (RT1, RT2, and RT3) using the FZI values.

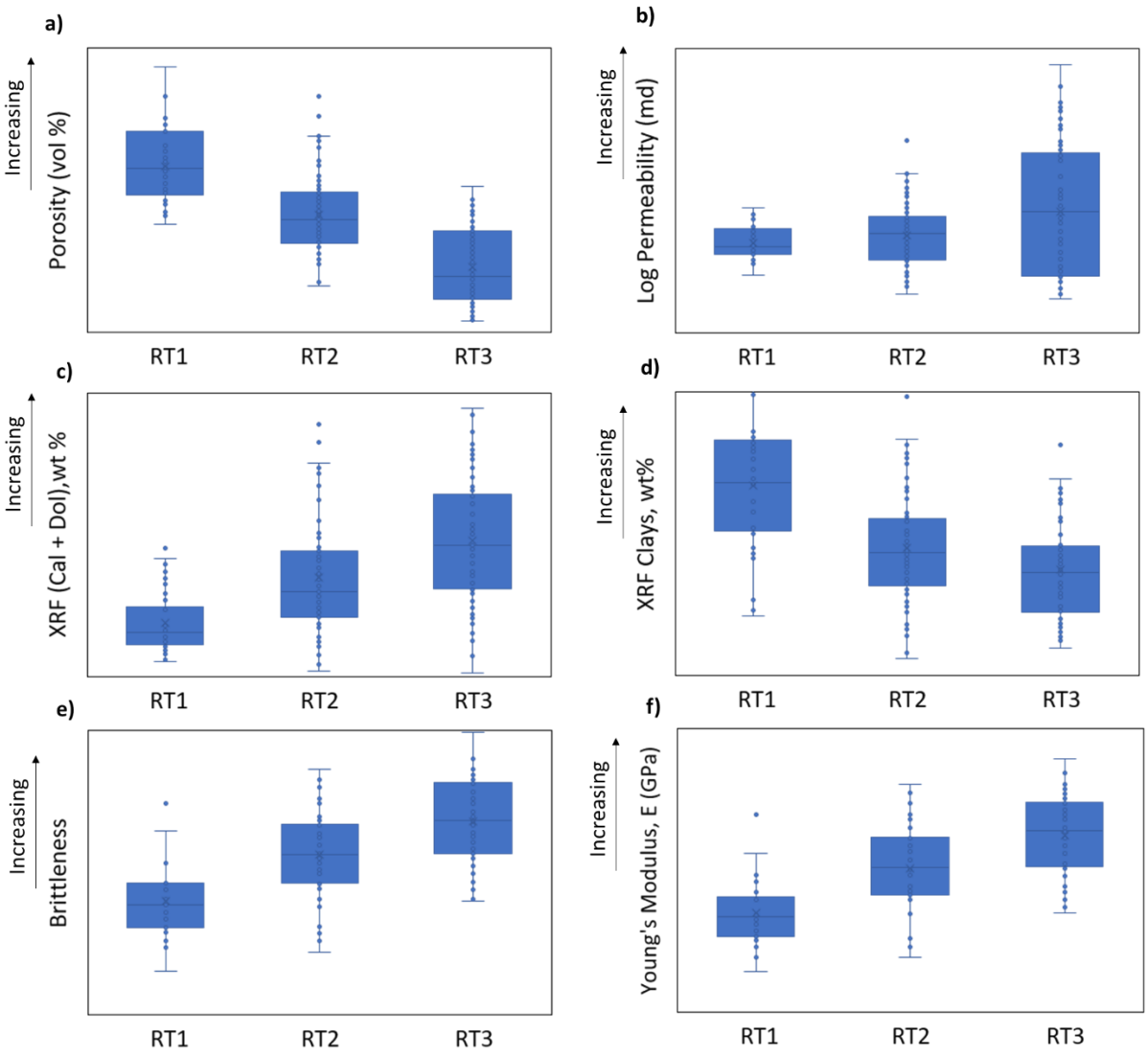

Figure 3-3. Variation of petrophysical properties for the three rock types: (a) porosity, (b) permeability, (c) XRF-derived carbonate content, (d) XRF-derived clay content, (e) Brittleness (as defined by Rickman et al., 2008) and (f) Young's Modulus. Porosity decreases while permeability increases from RT1 to RT3. Carbonate content increases while clay content decreases from RT1 to RT3. Brittleness increases from RT1 to RT3.

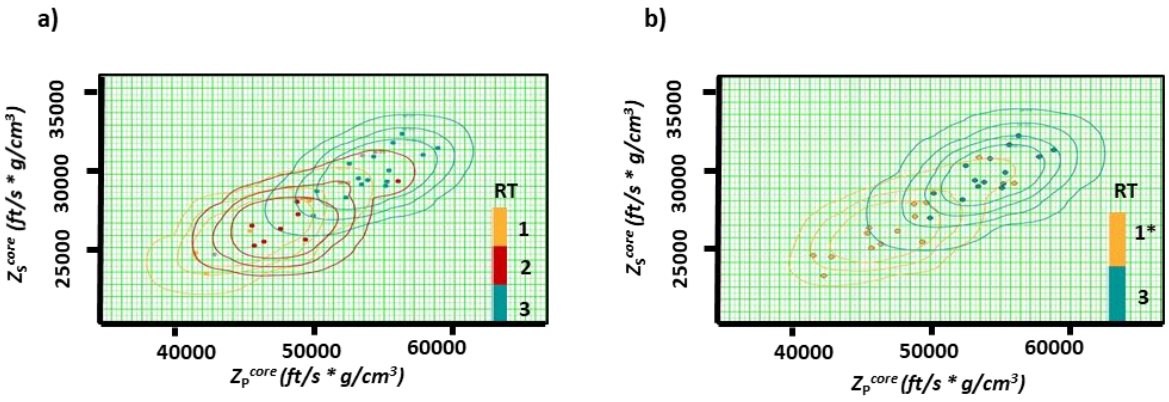

Figure 3-4. Cross plot of Z_P and Z_S computed from core measurements. The colors indicate the rock types using (a) all three rock types, and (b) rock types RT1* and RT2. A better delineation between the rock types is obtained in the elastic domain when we combine RT2 with RT1 to construct RT1*.

Table 3-1. Confusion matrix obtained from Bayesian classification when all the three rock types were classified in the Z_P - Z_S domain. Note that rock type 2 is poorly classified using these elastic parameters.

		Classified log		
		Rock type 1	Rock type 2	Rock type 3
Rock type log	Rock type 1	74.11%	24.92%	5.66%
	Rock type 2	22.56%	41.55%	27.64%
	Rock type 3	3.33%	33.53%	66.70%

Table 3-2. Confusion matrix obtained from Bayesian classification when RT2 was combined with RT1 (RT1*) and RT1* and RT3 were classified in the Z_P - Z_S domain. This simplification results in a more accurate classification for the two remaining rock types.

		Classified log	
		Rock type 1*	Rock type 3
Rock type log	Rock type 1*	85.88%	24.82%
	Rock type 3	14.12%	75.16%

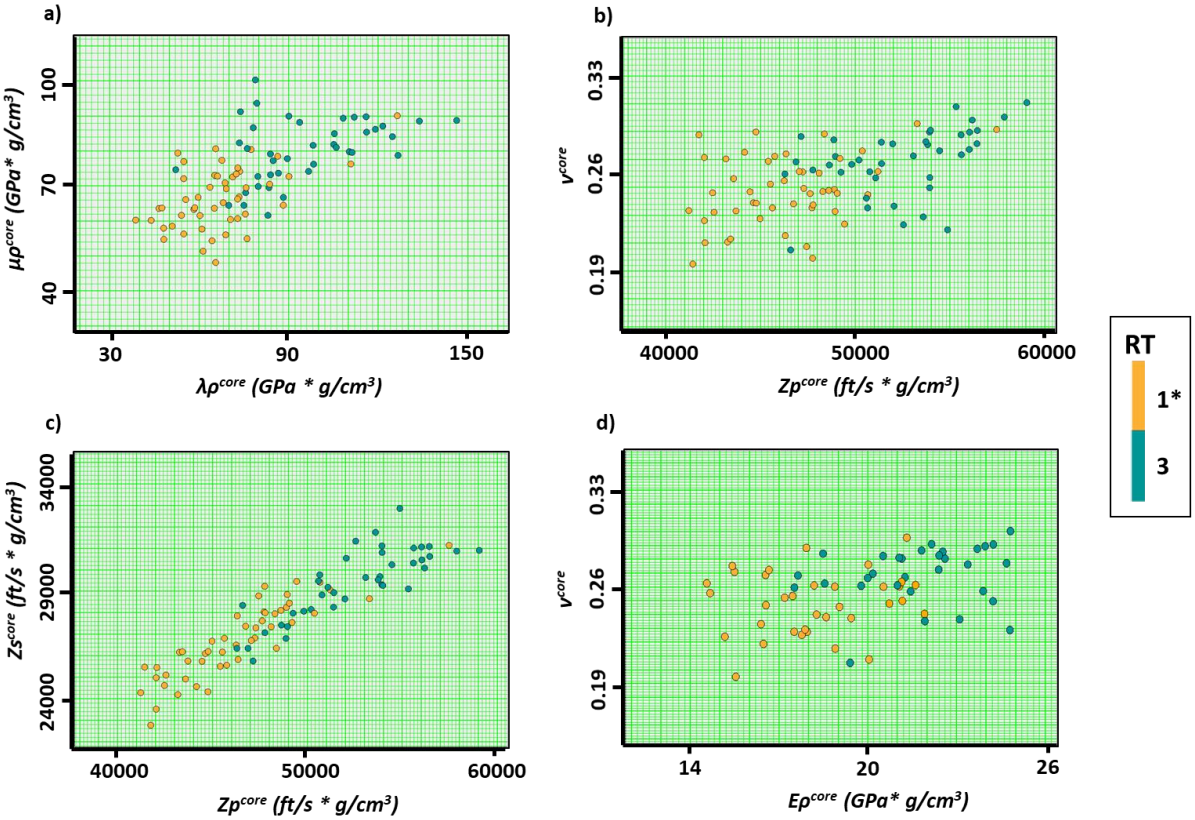

Figure 3-5. Cross plots between (a) lambda-rho ($\lambda\rho$) and mu-rho ($\mu\rho$), (b) P-impedance (Z_P) and Poisson's ratio (ν), (c) P-impedance (Z_P) and S-impedance (Z_S), and (d) Young's modulus-rho ($E\rho$) and Poisson's ratio (ν) measured on one of the well cores. Irrespective of elastic domain choice, the RT1* and RT3 show good, though not complete, elastic separability.

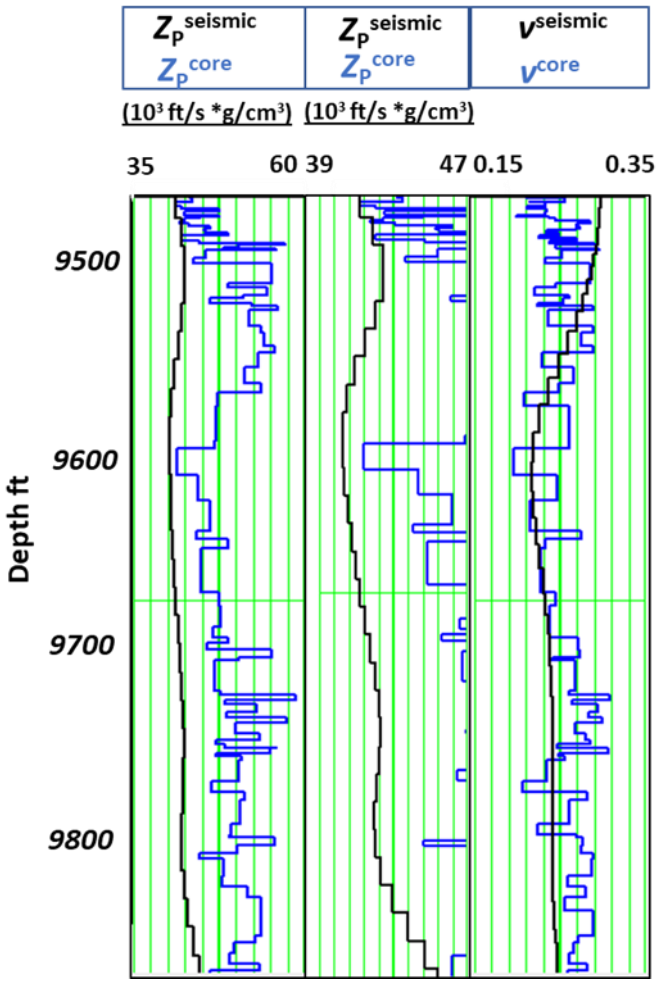

Figure 3-6. The left track shows the difference between Z_P derived from ultrasonic laboratory measurements on core (blue curve) and Z_P extracted along the well from the inverted seismic impedance volume (black curve). The middle track is the same as left track but with a change in scale, showing variation with depth. The right track shows the core and seismic v, where very little shift is observed between the core and seismic measurements.

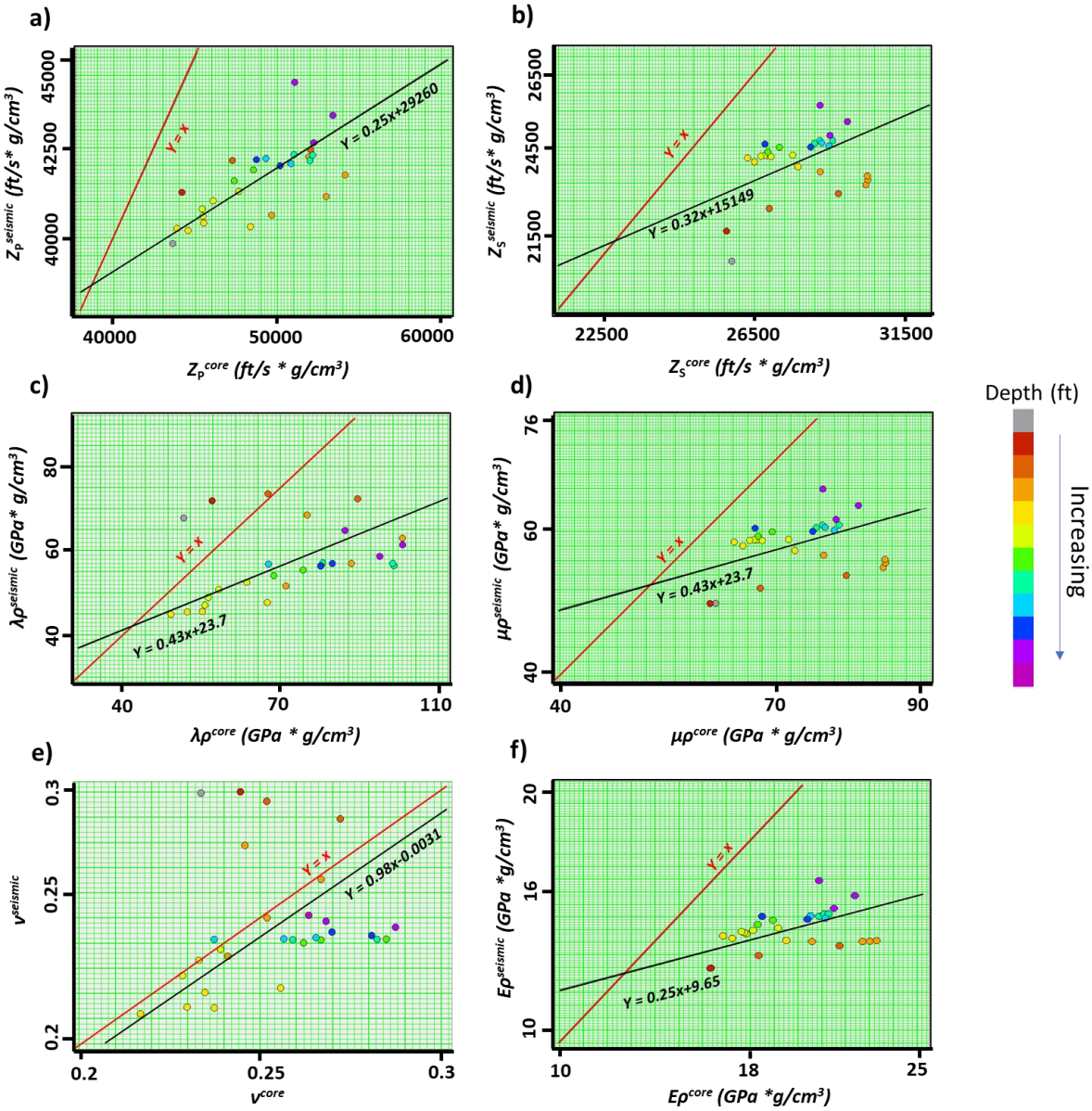

Figure 3-7. Cross plots between elastic properties measured at the core and seismic frequencies for (a) Z_P, (b) Z_S, (c) $\lambda\rho$, (d) $\mu\rho$, (e) v, and (f) $E\rho$.

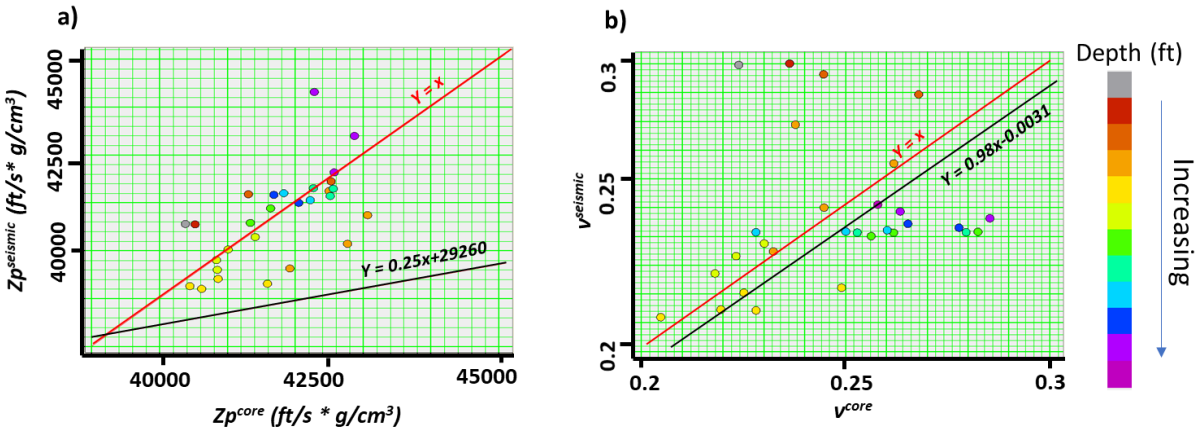

Figure 3-8. Cross plot between elastic properties measured at the core and derived from seismic for (a) Z_P and (b) v after scaling. The scaling has been performed using the linear equation mentioned in the respective cross plot.

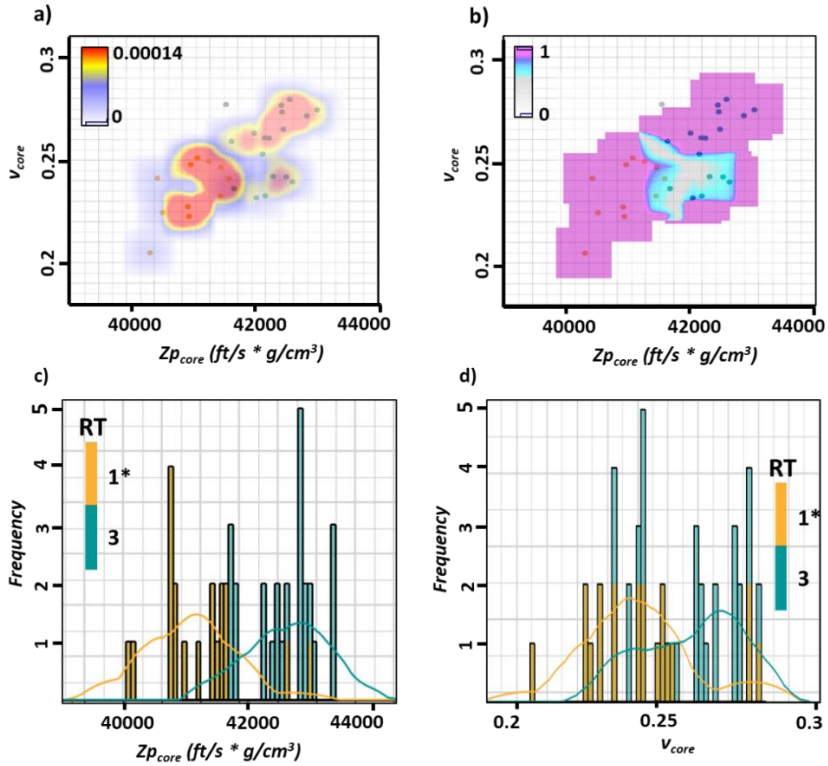

Figure 3-9. (a) Cross plot between Z_P^{core} and v^{core} overlain by the isomap of the conditional PDF. (b) The confidence map of predicting the facies. The overlap between the PDF of each rock type decreases confidence. Seismic estimates of Z_P-v pairs that fall in the white area are not represented by the rock properties sampled by the core measurements and are assigned to an "Unknown" rock type. One dimensional histograms and PDFs of (c) Z_P and (d) v for RT1* and RT3.

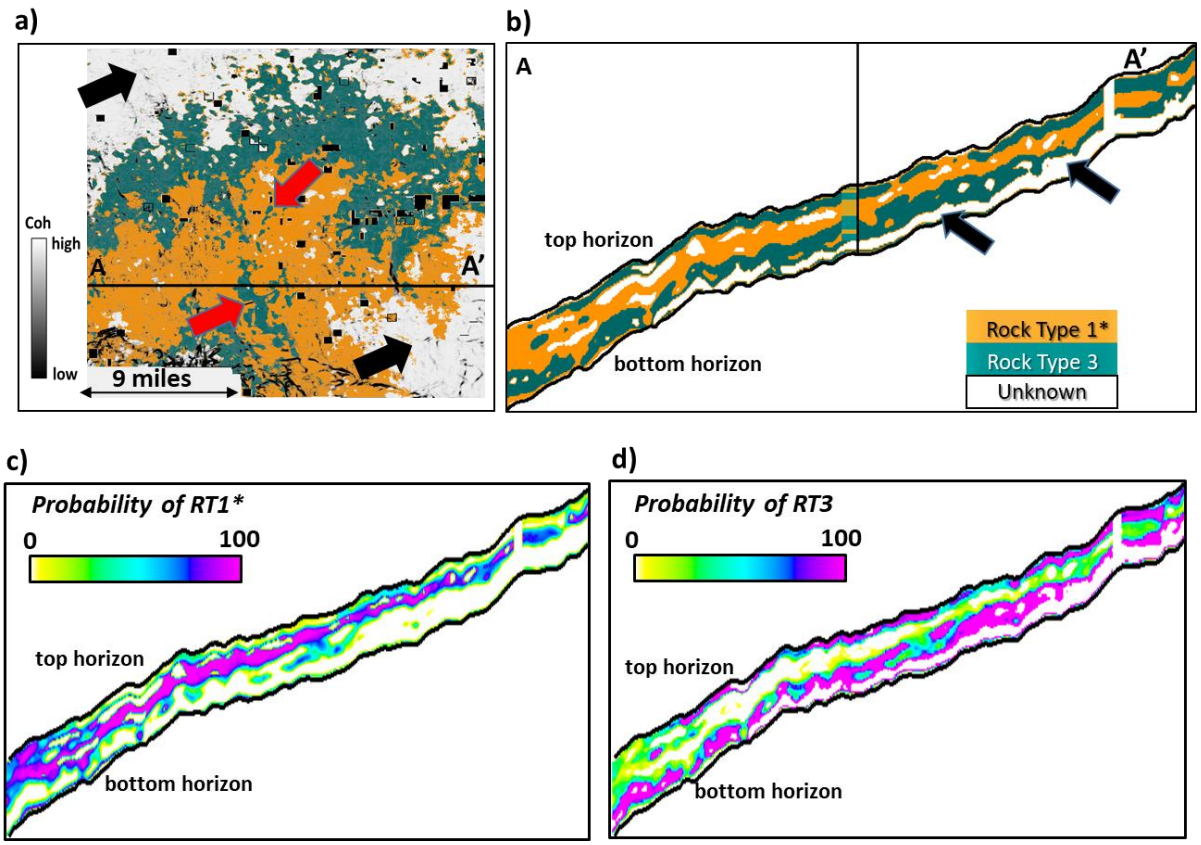

Figure 3-10. (a) Proportional slice at 40% below the top horizon through the (most likely) predicted rock type volume. Red arrows indicate channels. Black arrows indicate areas where rock type is unknown as described in Figure 9. (b) Cross-section along line AA' showing a good match of the predicted rock types at the well location. (c) and (d) show the probability of estimation of RT1* and RT3 respectively across the cross-section AA'.

REFERENCES

Amaefule, J. O., M. Altunbay, D. Tiab, D. G. Kersey, and D. K. Keelan, 1993, Enhanced reservoir description: using core and log data to identify hydraulic (flow) units and predict permeability in uncored intervals/wells: SPE Annual Technical Conference and Exhibition, SPE-26436-MS. https://doi.org/10.2118/26436-MS

Avseth, P., T. Mukerji, A. Jorstad, G. Mavko, and T. Veggeland, 2001, Seismic reservoir mapping from 3-D AVO in a North Sea turbidite system: Geophysics, 66 (4), 1157–1176. http://dx.doi.org/10.1190/1.1487063

Azra, T., 2010, Anisotropy, compaction and dispersion characteristics of reservoir and seal shales: 44th US Rock Mechanics Symposium, ARMA-10-344, Salt Lake City, Utah.

Best, A. I., and M. S. Sams, 1997, Compressional wave velocity and attenuation at ultrasonic and sonic frequencies in near-surface sedimentary rocks: Geophysical Prospecting, 45 (2), 327-344. https://doi.org/10.1046/j.1365-2478.1997.00337.x

Da Veiga, S., and M. Le Ravalec, 2012, Maximum likelihood classification for facies inference from reservoir attributes: Computational Geosciences, 16 (3), 709–722. https://doi.org/10.1007/s10596-012-9283-5

Doyen, P., 2007, Seismic reservoir characterization: An earth modelling perspective (EET2). EAGE

Duranti, L., R. Ewy, and R. Hofmann, 2005, Dispersive and attenuative nature of shales: multiscale and multifrequency observations: 75th Annual International Meeting, SEG, Expanded Abstracts, 1577–1580. https://doi.org/10.1190/1.2147994

Gonzalez, E. F., T. Mukerji, and G. Mavko, 2000, Facies classification using P-to-P and P-to-S AVO attributes: 70th Annual International meeting, SEG, Expanded Abstracts, 98-101. https://doi.org/10.1190/1.1816245

Grana, D., X. Lang, and W. Wu, 2016, Statistical facies classification from multiple seismic attributes: comparison between Bayesian classification and expectation–maximization method and application in petrophysical inversion: Geophysical prospecting, 65 (2), 544-562. https://doi.org/10.1111/1365-2478.12428

Gupta, I., C. H. Sondergeld, C. Rai, and D. Devegowda, 2017, Rock typing in Wolfcamp formation: 58th SPWLA Annual Logging Symposium, SPWLA-2017-D.

Higley, D.K. and S. B. Gaswirth, 2014, Petroleum systems and assessment of undiscovered oil and gas in the Anadarko Basin province, Colorado, Kansas, Oklahoma, and Texas – USGS Province 58, USGS Digital Data Series DDS-69-EE. https://doi.org/10.3133/ds69EE

Hofmann R., 2006, Frequency dependent elastic and anelastic properties of clastic rocks: PhD Thesis, Colorado School of Mines, Golden, Colorado.

Hornby, B. E., D. E. Miller, C. Esmersoy, and P. A. F. Christie, 1995, Ultrasonic-to-seismic measurements of shale anisotropy in a North Sea well: 65th Annual International Meeting, SEG, Expanded Abstract, 17-21. https://doi.org/10.1190/1.1887505

Johnson, K., 2008, Geologic History of Oklahoma: Educational Publication, 9, 3–8

Kale, S., C. Rai, and C. H. Sondergeld, 2010. Rock Typing in Gas Shales: SPE Annual Technical Conference and Exhibition, SPE 134539. http://dx.doi:10.2118/134539-MS

Lee, S.H., A. Kharghoria and A. Dutta-Gupta, 2002, Electrofacies characterization and permeability prediction in complex reservoirs, SPE Reservoir Evaluation and Engineering. V 5(3), 237-248, SPE 78662-PA. https://doi.org/10.2118/56658-MS

Miller, A., 2019. Mississippian Meramec Lithologies and Petrophysical property Variability, Stack Trend, Anadarko Basin, Oklahoma. MS thesis, University of Oklahoma, Norman, Oklahoma.

Miller, J. C., M. J. Pranter, and A. B. Cullen, 2019, Regional stratigraphy and organic richness of the Mississippian Meramec and associated strata, Anadarko Basin, central Oklahoma: Shale Shaker, 70 (2), 50-79.

Mukerji T., A., Jørstad, P. Avseth, G. Mavko, and J. R. Granli, 2001, Mapping lithofacies and pore-fluid probabilities in a North Seareservoir: seismic inversions and statistical rock physics: Geophysics 66 (4), 988–1001. https://doi.org/10.1190/1.1487078

Murphy, W. F., K. W. Winkler, and R. L. Kleinberg, 1986, Acoustic relaxation in sedimentary rocks, dependence on grain contacts and fluid saturation: Geophysics, 51 (3), 757–766. https://doi.org/10.1190/1.1442128

Patel, S., and K. J. Marfurt, 2019, Flexures in the Anadarko Basin: Do they indicate faulting or folding? 90th Annual International meeting, SEG, Expanded Abstracts, 1953-1957. https://doi.org/10.1190/segam2019-3216621.1

Perry, W. J., 1989, Tectonic evolution of the Anadarko Basin region, Oklahoma: US Geological Survey Bulletin, no. 1866. https://doi.org/10.3133/b1866A

Pittman E.D., 1992, Relationship of Porosity and Permeability to Various Parameters Derived from Mercury Injection – Capillary Pressure Curves for Sandstones: AAPG Bulletin, 76 (2): 191-198.

Pranter, M. J., A. Turnini, K. Marfurt, and D. Devegowda, 2016, Multidisciplinary characterization and modeling of Mississippian carbonate and silica-rich reservoirs, northern Oklahoma: AAPG Mid-Continent Section meeting, AAPG Search and Discovery.

Price, B., K. Haustveit, and A. Lamb, 2017, Influence of stratigraphy on barriers to fracture growth and completion optimization in the Meramec Stack Play, Anadarko Basin, Oklahoma: Unconventional Resources Technology Conference (URTEC), URTEC-2697585-MS. https://doi.org/10.15530/URTEC-2017-2697585

Robert R. S., P. D. Huddleston, and T. K. Kan, 1984, Seismic versus sonic velocities: A vertical seismic profiling study: Geophysics 49(8): 1153-1168. https://doi.org/10.1190/1.1441745

Rogers, S. M., 2001, Deposition and diagenesis of Mississippian chat reservoirs, north central Oklahoma: AAPG Bulletin, 85 (1), 115-130. https://doi.org/10.1306/8626C771-173B-11D7-8645000102C1865D

Schlanser, K., D. Grana, E. Campbell-Stone, 2014, Petro-elastic facies classification in the Marcellus Shale by applying Expectation Maximization to measured well logs, 84th Annual Technical conference and exhibition, SEG, 659-663. https://doi.org/10.1190/segam2014-0939.1

Schmitt, D. R., 1999, Seismic attributes for monitoring of a shallow heated heavy oil reservoir: A case study, Geophysics, 64 (2), 368–377. https://doi.org/10.1190/1.1444541

Suarez-Rivera, R., S. M. Willson, S. Nakagawa, and O., Magnar-Ness, 2001, Frequency Scaling for Evaluation of Shale and Mudstone Properties from Acoustic Velocities: AGU Fall Meeting Abstracts.

Wang G., T. R. Carr, Y. Ju, and C. Li, 2014, Identifying organic rich Marcellus shale lithofacies by support vector machine classifier in the Appalachian basin: Computers and Geosciences, 64, 52–60. https://doi.org/10.1016/j.cageo.2013.12.002

CHAPTER 4 SEISMIC ILLUMINATION OF SMALL-OFFSET SEISMOGENIC FAULTS, ANADARKO BASIN, OKLAHOMA

Swetal Patel[*1], Folarin Kolawole[1], Jacob I. Walter[2], Xiaowei Chen[1], and Kurt J. Marfurt[1]*

[1]School of Geosciences, University of Oklahoma, Norman, OK

[2]Oklahoma Geological Survey, University of Oklahoma, Norman, OK

ABSTRACT

In the last decade across the Central and Eastern US, there has been a substantial increase in the seismicity rate that scientists broadly attribute to wastewater disposal and, to a lesser extent, hydraulic fracturing. Active clusters of seismicity illuminate linear fault segments within the crystalline basement that were not known until seismicity began. Such surprises are due to the limited availability of 3D surface seismic surveys and the difficultly in imaging relatively shallow earthquake events from sparse seismic monitoring arrays. The STACK play of Central Oklahoma provides an opportunity to map such basement faults. Modern, high-quality surface seismic acquired to map the Meramec, and Woodford unconventional resource plays enable us to image basement faults and intrusions. Furthermore, because of increased earthquake risk from anthropogenic activities in the last decade, state regulatory agencies have deployed a relatively dense array of seismic monitoring stations, which allows us to integrate earthquake data into subsurface fault analysis. We map structural deformation using a suite of seismic attributes, including multispectral coherence, volumetric curvature, and aberrancy in a 3D seismic reflection dataset covering 1100 sq mi in the STACK area of Anadarko Basin, Oklahoma. To unravel the relationship between the structures and seismicity, we use relocated locally recorded earthquakes and compute the focal mechanism solution for the relocated events. Our results reveal a total of 90

previously unmapped top basement fault segments with dominant N-S, NW, and NE trends, the majority of which extend into the shallower sedimentary Hunton and Woodford formations. Because of the small fault offset, we find that aberrancy and curvature attribute best illuminate the basement-rooted faults in the study area. Fault segments with significant offset are better illuminated by bandlimited multispectral coherence. We argue that the inherited structure of these faults makes them easily illuminable by flexure-related seismic attributes, especially within the sedimentary cover. The integration of the illuminated faults with relocated earthquakes and focal mechanism solutions shows that some of the illuminated faults that have hosted intra-sedimentary and/or basement seismicity are reactivated strike-slip faults. We hypothesize that careful attribute mapping of faults and flexures, coupled with an understanding of the local stress and geomechanical properties, and calibrated with recent seismic activity in the area can help mitigate seismic hazards in tectonic settings where small-offset faults predominate.

INTRODUCTION

Within intraplate regions of the earth where low strain rates dominate, pre-existing faults are important for seismic hazard quantification. The hazard is highlighted by the recent spike in intraplate seismicity in Central and Eastern United States, which has been attributed to unconventional resource exploration and disposal of wastewater into deep sedimentary units that overlie the crystalline basement (e.g., Ellsworth, 2013; Weingarten et al., 2015; Machado et al., 2020). The increase in induced seismicity is most sporadic and widespread in the crystalline basement of Oklahoma, where the susceptibility has been attributed to the pre-existing structural fabric and frictional stability of the basement fault rocks (Kolawole et al., 2019).

In the last decade, Oklahoma went from a state experiencing an Mw 3.0 or greater earthquake about twice per year to experiencing 579 and 903 M3.0 or greater earthquakes in 2014

and 2015, respectively (Walter et al., 2020). From 2010 till present, Oklahoma Geological Survey cataloged more than 34,000 earthquakes (Figure 1a), including 24,840 earthquakes with magnitude >2.0, 2920 earthquakes with magnitude >3.0, and 77 with size >4.0 (https://ogsweb.ou.edu/eq_catalog/). The Nemaha fault separates two major seismic zones to the west and east sides and may plausibly act as a pressure boundary (Qin et al., 2019). The seismicity is mainly caused by wastewater produced as part of hydrocarbon production from shallower targets injected into deeper subsurface karstic Arbuckle Group, which lies directly above much older basement rocks at most places in Oklahoma. Such "injection-induced" seismicity peaked in 2015, which correlated to the dramatic increase in saltwater injection into the subsurface formation in the same year (Langenbruch et al. 2018). After 2015, market forces and a decrease in the injection rate were mandated by the Oklahoma Corporation Commission, which plausibly drove a reduction in the seismic activity rate (Walter et al., 2020). Though the injection-induced seismicity reduced substantially, the 2016 Mw 5.8 Pawnee Oklahoma earthquake (Walter et al. 2017) was one of the two largest cases of induced seismicity in the world within the past decade.

Saltwater, that is, coproduced with hydrocarbons, is injected into porous and permeable subsurface formations in Oklahoma for two operations: water flooding enhanced oil recovery (EOR) and saltwater disposal (SWD) (Walsh and Zoback, 2015). Saltwater disposal can cause an increase in the formation of pore pressure, promoting fault slip along optimally oriented faults (Walsh and Zoback, 2015; National Research Council, 2013). In addition to wastewater disposal or injection, carbon sequestration (Kaven et al. 2015) and hydraulic fracturing (Holland et al., 2013; Skoumal et al. 2015; Lei et al. 2017, Skoumal et al. 2018, Eyre et al. 2019) have also been linked to inducing earthquakes. Unlike carbon sequestration, hydraulic fracturing is common in Oklahoma because the economic exploitation of the Mississippian formation in the STACK

(Sooner Trend Anadarko Basin Canadian Kingfisher counties) area of Oklahoma requires marrying horizontal well technology with hydraulic fracturing. Shemeta et al. (2019) statistically identified 333 wells out of ~5,000 completions with hydraulic-related seismicity between October 2016 and August 2019. Though the broader statewide earthquake activity peaked in 2015 in Oklahoma (Langenbruch et al. 2018), relatively fewer earthquakes were recorded in the STACK during that time (Figure 1b). Most of the events in the STACK occurred between 2015-2019 (Figure 1c), coinciding with the exploitation of the Mississippian formation in the STACK area through drilling new wells in the unconventional Woodford and Meramec plays. The histogram analysis by Shemeta et al. (2019) correlated 1438 earthquakes in STACK and adjacent SCOOP (South Central Oklahoma Oil Province, Figure 1a) with the hydraulic fracturing notices filed by the operators. Out of 1438 events, the largest event of magnitude (M_w) 3.6 occurred in Kingfisher county in mid-2019. For this reason, although the bulk of earthquakes are associated with wastewater disposal, hydraulic fracturing-induced earthquake seismicity in the STACK cannot be ruled out.

The Oklahoma fault database (http://www.ou.edu/ogs/data/fault) is a comprehensive dataset of mapped faults created to gain a better understanding of seismic hazards and subsurface geology (Marsh and Holland, 2016). Figure 1 shows interpreted faults from the Oklahoma fault database compiled using data voluntarily provided by the oil and gas industry augmented by the published literature. Though induced seismicity is mainly caused by critically stressed fault reactivation, it is not necessary that the hypocenters of the earthquakes coincide with the mapped faults (Figure 1d). Such lack of direct correlation is due to multiple reasons: few faults in the identified in the basements and included in the database, uninterpreted faults in the area, hypocenter location uncertainty, and fault location uncertainty, particularly from those measured

near the surface and projected into the basement. Marsh and Holland (2016) noted that though the database cataloged many faults, that the database remains incomplete. Incompleteness stems from different definitions of "significant" faults across the industry, the difference in interpretation of subsurface data, the relatively poor illumination of smaller faults by legacy 2D seismic surveys, the inability of the interpreter to provide file formats compatible with the database (Holloway et al., 2015), and incomplete fault mapping in non-hydrocarbon prone areas of Oklahoma (Marsh and Holland, 2016). Hence, uninterpreted faults in the STACK area may underlie observed seismicity lineaments (Figure 1e).

In this paper, we use surface seismic and earthquake data to map potentially seismogenic faults in the STACK area. Such mapping can aid operators in minimizing injection-induced or hydraulic fracturing-induced earthquakes. We begin the paper by examining the problems that cause difficulty in imaging the faults in the STACK area. We then show how seismic attributes such as band-limited multispectral coherence, curvature, and aberrancy help delineate not only faults that exhibit offset, but also flexures that may indicate faults that fall below seismic resolution. Next, we correlate earthquake events imaged by a statewide array of surface seismometers to previously mapped faults and to faults and flexures mapped in the 3D seismic volume. We conclude with a summary of how the use of 3D surface seismic data, calibrated by mapping previous earthquake locations, may help minimize future earthquakes induced by wastewater injection and/or completion processes.

GEOLOGIC SETTING

The STACK area is located within the Anadarko Basin, Oklahoma (Figure 1a). The NE-SW -dipping Anadarko Basin is the deepest phanerozoic sedimentary basin in North America (Perry, 1989) and is composed of Ordovician to Permian sedimentary sequences that unconformably overlie the Precambrian granitic basement (Johnson, 2008). The present depth to the top of the eroded Precambrian basement ranges from 1,000 ft in the northeast to 40,000 ft in the southwest (Johnson, 2008). Burke (1977) reported that rifting during the Late Proterozoic extensional tectonics reactivated older Proterozoic and Cambrian faults to create the Mid-Continent Rift and Southern Oklahoma Aulacogen. Perry (1989) provides details on the tectonic evaluation of the Anadarko Basin, dividing the evolution of the Anadarko Basin into four different stages: 1) crustal consolidation and metamorphism during the middle Proterozoic, during which time much of the basement in central Oklahoma was formed by igneous activity, 2) development of the South Oklahoma Aulacogen during the Cambrian Period, 3) development of the southern Oklahoma trough between the Cambrian and the Mississippian and 4) contractional tectonic deformation of the older sedimentary units and subsidence of the Anadarko Basin as an intracratonic foreland basin during the Late Mississippian to Late Pennsylvanian. The Late Paleozoic contractional deformation peaked in the Late Pennsylvanian time during which the reactivation of the Precambrian basement faults resulted in folding, faulting, and transpressional deformation of the Phanerozoic sedimentary units (Gay, 2003; McBee, 2003; Kolawole et al., 2020). Hence, the basement faults have been created and reactivated several times during Precambrian, Cambrian, and Late Paleozoic time. The study area, STACK, is bounded by one of these faults, the Nemaha fault, to the east (Figure 1a).

The STACK area has garnered renewed interest due to multiple stacked layers of producible hydrocarbon formations. Figure 2a provides a generalized stratigraphic layout of the Anadarko Basin. The Mississippian Woodford and Meramec are the current target formation for unconventional hydrocarbon exploitation, whereas the Ordovician Arbuckle is the target formation for wastewater injection. The Ordovician to Mississippian formations were deposited on the top of the unconformity created by a brief period of erosion of the earlier Cambrian and Precambrian rocks. This period of erosion was followed by a long geologic time when sediments were deposited as parts of Oklahoma were alternately flooded by shallow seas and then raised above sea level. The Arbuckle Group was deposited during the Late Cambrian to Middle Ordovician time when Oklahoma was submerged entirely, and subsequently, thick limestone and dolomite were deposited over the entire state. The Hunton Group was deposited during the Silurian and Early Devonian periods and consisted of limestone and dolomite overlain by black shale. After widespread uplift and erosion forming an erosional unconformity, the Woodford Shale was deposited in the same areas as the Hunton during the Late Devonian and Early Mississippian periods. During the last half of the Mississippian, the basin subsided and led to deposition predominantly of shale with layers of limestone and sandstone. Primary formations deposited during this period are the Caney Shale, the Goddard formation, and the Springer formation.

DATA AND METHODS

3D Seismic Reflection Data

In this study, we analyze an ~1,100 square mi (~2,800 square km) high fold 3D seismic reflection survey located in the STACK area of central Oklahoma (Figure 1a). The data are devoid of random noise, migration artifacts, and acquisition footprint. The survey is a part of the Gigamerge survey created by combining 20 legacy and seven recent surveys acquired in the

northcentral Oklahoma. spectrally balancing of seismic volume provided a flat spectrum between 15 to 60 Hz with usable frequencies between 10 to 70 Hz, giving quarter wavelength resolution of 73 feet in the Mississippian formations.

The stratigraphic surfaces (top of the Mississippian, Meramec, Woodford, and Hunton formations) were interpreted in the seismic using well tops and seismic well ties (Figure 2b). The depth of the Woodford Formation in the survey ranges from 1470 ms. to 2140 ms.

The thickness of the interpreted sedimentary formations increased towards the northeast and decreased towards the southwest. Due to the unavailability of a well-drilled deep enough to the basement, the first continuous reflector above the basement was interpreted as the top of the basement.

To illuminate the structures in the dataset, we compute a suite of seismic attributes, including bandlimited multispectral coherence, curvature, and aberrancy. Examining horizon slices along the top basement allow us to characterize basement-related structural deformation, whereas horizon slices along the top Hunton provide an assessment of structural deformation in the shallower intra-sedimentary sections.

3-D Seismic attributes

Frequency-Dependent Multispectral Coherence

Seismic coherence is a routine measure to image structural and stratigraphic discontinuities. Marfurt and Chopra (2007) described several ways to compute waveform dissimilarity in nearby traces. Generally, interpreters prefer to calculate coherence using the broadband amplitude spectrum to image maximum resolvable features. But due to thickness tuning effect and variable signal to noise ratio at different frequencies, coherence computed on specific spectral components can highlight features of certain thicknesses much better than at others

(Marfurt, 2017; Li et al. 2018). Also, Partyka et al. (1999), Peyton et al. (1996), and Gao (2013) have shown that different spectral components reveal different geologic details. In the seismic data used in this paper, the 30-55 Hz frequency range revealed smaller as well as larger faults on coherence in the Mississippian formation (Patel and Marfurt, 2019). Adding or subtracting frequencies did not change the resolution of faults in the Mississippian formations. Hence, we computed coherence on the 30-55 Hz spectral components using the approach described by Li et al. (2018). A significant improvement is observed by computing coherence using band-limited data when compared to conventional broadband coherence (Figure 3a and b).

Volumetric Curvature

Although curvature does not map discontinuities, it does map the structural deformation about faults. Curvature will have large positive values for tightly folded anticlines, large negative values for tightly fold synclines, and a zero value for a flat or dipping planar features. For 2D structures, the curvature is reciprocal to the radius ($\boldsymbol{r}$) of the circle that is tangent and best fits a deformed surface at a particular point (Figure 4d). Figure 4c shows the anticlinal features of the flexures in the basin imaged by k_1 and the synclinal features imaged by k_2. Since the flexures appear conformal over the sedimentary section, unlike coherence, the curvature will image these deformed features across the whole section. The interpretation problem then becomes in distinguishing a simple fold from faults whose throw falls below seismic resolution and appears to be a fold. For normal faults, the most-positive k_1 and most-negative curvature k_2 anomalies bracket the fault rather than map the fault surface (Figure 4e). In contrast, aberrancy, the derivative of curvature, better delineates the fault surface.

Volumetric Aberrancy

Aberrancy measures the lateral change in curvature of a picked surface (Qi and Marfurt, 2018). Like curvature, it is also a measure of the deformation. In 3D, the aberrancy is described by its magnitude and azimuth (Qi and Marfurt, 2018). The magnitude is proportional to the amount of deformation, and the azimuth describes the direction of a decrease in curvature value (Figure 4g). Whereas the dip vector is the first derivative of the structure, the principal curvatures is the second derivative, and the aberrancy is the third derivative of the structure. Automatically computing time-structure maps for every voxel is currently limited only to small zones of interest (Schmidt et al. 2010). However, there are multiple ways to compute volumetric estimates of dip (Chopra and Marfurt, 2007). For this reason, volumetric aberrancy is computed using the second derivatives of the dip vector. Algorithmic details can be found in Di and Gao (2014) and Qi and Marfurt (2018).

In this paper, the azimuth of aberrancy is mapped against the hue axis of an HLS color model represented by a cyclical color bar. The magnitude of aberrancy is mapped against the saturation axis of the HLS color model. Several interpretation software packages allow mapping any three attributes against HLS. In cases where this option is not available, a workaround is to co-render the aberrancy azimuth and magnitude using opacity, as described by Marfurt (2015), where the aberrancy magnitude is plotted against the monochrome gray of the grey color. High magnitude values have low opacity (are transparent), showing the underlying azimuth value, while low magnitude values have high opacity and appear gray. Hence, the planar features appear grey while the flexures appear colored corresponding to the aberrancy azimuth values (Figure 4f). Unlike the curvature, the aberrancy magnitude images the fault trace (Figure 4h).

Earthquake Data, Event Relocation, and Focal Mechanism Computation

The Oklahoma Geological Survey (OGS) has monitored earthquake activity in the state over the last several decades (Walter et al., 2020). The network has expanded in an ad-hoc fashion to address monitoring needs as the seismicity rate increased in the last decade. OGS operates over 100 seismometers throughout the state and is the official Advanced National Seismic System (ANSS) regional network within the state, such that USGS catalog events are sourced from OGS. During business hours, analysts manually pick waveform phases and determine P-wave polarities for regional events within the state, when the signal-to-noise ratio allows. Accurate phase picks and P-wave polarities inform precise relocation and focal mechanism determination for events in the study region.

Since July 2010, we identified 3,438 catalog earthquakes within the study region defined by the bounds of 35.5- and 36.5-degrees' latitude North and 98.5- and 97.5-degrees' longitude West. We relocated events using a double-difference algorithm, HypoDD (Waldhauser and Ellsworth, 2000), and initially chose a velocity model consistent with the one used for OGS routine locations (Walter et al., 2020). We altered the velocity model to be more consistent with known basement and stratigraphic constraints (e.g., Crain and Chang, 2018). In addition, we used a Vp/Vs ratio of 1.78 rather than the 1.73 to be consistent with available well sonic log information and consistent with a recent relocation study (Schoenball and Ellsworth, 2017). The velocity model used for relocation is included as electronic supplemental information. In addition to the relocation, we recomputed focal mechanisms in a uniformly consistent manner using analyst-picked polarities inputted into the HASH program (Hardebeck and Shearer, 2002).

RESULTS

Structures revealed in Seismic Attribute Maps

Figure 5 shows a horizon slices along the top basement through a suite of seismic attribute volumes. Figure 6 shows similar horizon slices along the top Hunton. The paleotopographic features are best delineated on bandlimited multispectral coherence along the top Basement, but the correlation of the attribute with the earthquakes reveals that most earthquakes do not correlate to any mapped coherence anomalies (Figure 5a). The horizon slices through curvatures (Figure 5b) and aberrancy (Figure 5c) provide images of flexures rather than discontinuities. For normal faults with sufficient offset, the coherence anomaly maps the fault trace while the most-positive and most-negative curvature anomalies bracket the fault trace. As seismic resolution (or fault offset) decreases, the coherence anomaly disappears, but the curvature anomalies remain. Aberrancy maps the crossing point (flexure) from positive to negative curvature, thereby mapping a hypothesized fault trace. A total of 36, 70, and 76 lineaments were mapped on coherence, curvature, and aberrancy, respectively (Figure 5e). The lineament density is much lower in coherence compared to curvature and aberrancy.

Unlike along top basement, horizon slices through multispectral coherence along the top Hunton show considerable faulting. The most prominent are the NS lineament (purple arrow, Figure 6), imaged by curvature and aberrancy on the top basement, and the EW lineament (yellow arrow, Figure 6). The signature of the paleotopographic features disappears on coherence through top Hunton. Curvature reveals several new features and improves continuity of the NS lineament, as well as the splays associated with the EW lineament (Figure 6c). Aberrancy improves continuity of some of the lineaments imaged by curvature, and it also delineates other features that correlate with the paleotopographic features on top Hunton (Figure 6d). We attribute some of the greater

detail seen along the top Hunton to the higher frequency data at the shallower depths compared to the lower frequencies at the deeper basement. However, some of these features are geological, perhaps related to the helicoidal deformation of strike-slip faults like those observed over a Trenton Limestone play in Ohio (Sagan and Hart, 2006). A total of 56, 74, and 85 lineaments were mapped on coherence, curvature, and aberrancy, respectively, along top Hunton (Figure 6f). Coherence reveals a higher number of features on top Hunton than the top of the basement but still less than revealed by curvature and aberrancy. Aberrancy reveals the highest number of lineaments on top Hunton.

Because the Woodford formation overlays the Hunton, aberrancy delineates similar features on top Hunton and top Woodford (Figure 6d and e). Hence, we do not show a separate analysis for the Woodford and anticipate a similar statistical correlation on it. The earthquakes in the STACK area do not occur isolated, but rather correlate with the lineaments delineated by the curvature and aberrancy (Figure 5b-c, 6c-e). Aberrancy provides superior imaging of these structural features on the top Hunton and top basement. Where earthquakes align with aberrancy anomalies, they corroborate our hypothesis that these anomalies are faults or fault zones with offsets that fall below seismic resolution, or even weaker, fractured flexures rather than simple flexures that have deformed elastically or plastically.

On vertical slices (e.g., see Figures 3a, 4c, and 4f), these lineaments represent sub-vertical discontinuity surfaces that vertically offset and/or otherwise deform the stratigraphic reflectors. Along any of the discontinuity surfaces, we observe that offset geometries are often localized on the deeper reflectors, whereas the flexures often occur upsection on the shallower reflectors (e.g., Figure 3a). Because vertical seismic resolution decreases (and the loss of lateral resolution resulting in blurring increases) with depth, this observation implies that the change in the fault

character with depth is based on geology rather than on seismic data quality. Faults may lose offset, splay into a fault zone, or continue into more plastic lithologies as they propagate upward into the sedimentary section. We also observe that many of the discontinuities extend into the basement and offset or truncate vertically stacked intra-basement reflectors interpreted by Chopra et al. (2017) and Folarain et al. (2020) to be igneous sills (e.g., Figure 3a). Although sills can step upward (Chopra et al., 2017), such steps always follow a zone of weakness, which we would also interpret to be joint or fault. Following on the observations from previous studies (Chopra et al., 2017; Patel and Marfurt, 2019; Kolawole et al., 2019) and observing a correlation between the earthquakes and lineaments delineated by curvature and aberrancy, we interpret these illuminated lineaments as faults. Overall, these fault-related lineaments show little to no offset on the top basement and top Hunton surfaces. Within the seismic survey, the largest observed offset of faulting at the top Basement surface is ~30ms, whereas, at the top Hunton, the largest observed flexure is ~45ms.

Distribution of Interpreted Fault Lineaments

By integrating the seismic attribute maps (Figures 5 and 6), we identified and mapped 86 fault lineaments on the top Basement, 88 on the top Hunton, and 90 on the top Woodford surfaces (Figures 7a). Essentially, the density of fault lineaments decreases slightly with depth from the sedimentary sequences into the basement. The frequency-azimuth distribution of the fault lineaments for all three surfaces show multimodal distribution with similar prominent trends (Figures 7b-d). The prominent trends on three surfaces are NNW-SSE to ~N-S, NW-SE, and NE-SW. Among the NW and NE trends, the NW trend appears to be more dominant on the top basement and top Woodford surfaces.

Relocated Earthquake Patterns and Focal Mechanism Solutions

For the Kingfisher-Blaine-Canadian Counties (Figures 1a and 1e), we relocated a total of 3,523 recorded between 2010 to 2019 with magnitudes ranging from Mw0.6 to Mw4.5 (Figures 8a-b). The median error in the relocated events was 400 m horizontally and 800 m vertically. HypoDD relocation can get very good relative locations, but the absolute event location depends on velocity model. This is a challenge for regional seismic network. The surface locations (lat, long) of these events are generally more reliable than depth. The event histogram (Figure 8a) shows that although events extend down to >12 km depths, most of the earthquakes in this part of the basin occurred between 4-8 km which is located within the crystalline basement (Figure 8a). Only 2.2% of the events were located in the sedimentary formations. Additionally, a scatter plot of the earthquake magnitude shows that most of the intra-sedimentary earthquakes cover a relatively narrower range (Mw1.9 – 2.8) compared to those hosted within the basement (Mw1.0 – 3.8).

A North-South vertical section of seismicity clusters across the study area (Figure 8b) shows that the event clusters delineate sub-vertical rupture planes that extend from the deep basement zones (>10 km) across the top basement surface through the shallow sedimentary sequences. Additionally, the temporal evolution of the seismicity shows that the events recorded 2015 onwards overprints the older event clusters in the basement. Further, the shallowest events (blue arrow in Figure 8b) occurred more recently consistent with the period of most prevalent seismicity in the study area (Figure 1c).

We generated focal mechanism solutions for 207 events across the study area (Figures 9a-b). In plane-view, the relocated event clusters and focal mechanism solutions are collocated with (occurred directly on or near) several fault lineaments in the seismic attribute maps of the top basement (Figures 9a-b). Overall, the focal mechanism solutions show predominantly strike-slip

faulting with minor normal faulting along NW-SE and NE-SW trending nodal planes. The overlay of earthquake events on the seismic depth-sections (e.g., Figures 10a-b) shows the collocation of basement and sedimentary earthquake clusters with stacked discontinuity surfaces. Extracted curvature seismic attributes reveal multiple sub-vertical discontinuity surfaces that extend from the basement up into the sedimentary cover and connect isolated or clusters of earthquake events in both basement and sedimentary intervals (Figures 10b-c).

DISCUSSION

Seismic Illumination of Small-Offset Seismogenic Faults with Aberrancy and Curvature Attributes

The bandlimited multispectral coherence (Figure 4a) provides a much better improvement to broadband coherence (Figure 3a). However, the lateral extents of the fault lineaments in the coherence maps are largely underrepresented when compared to the curvature (Figure 5c) and aberrancy (Figure 5d) maps. For example, aberrancy and curvature attributes show significant improvement in delineating the N-S-trending faults compared to coherence. Additionally, we observe that the coherence fault lineaments are restricted to fault segments that show distinct offset character with associated significant flexure of the stratigraphic reflectors. Coherence measures similarity between neighboring waveforms. If the waveforms are very similar, the coherence attribute will have high value, and if the waveforms are very different, coherence will have low value. Coherence will image a fault with a seismically resolvable offset (more than one-quarter of the seismic wavelength), because the waveforms across the faults will be dissimilar. Figures 3b and c show broad-band coherence computed on the seismic data and extracted across the top of the basement and Hunton formation. Some of the faults have seismically resolvable offset on the top of the basement (Figure 3b). Coherence fails to image these faults in the sedimentary sections

because of flexures in the sedimentary section cause waveform similarity in nearby traces (Figure 3c).

Therefore, we infer that in geologic settings such as the Anadarko Shelf, where low fault offsets dominate, the curvature and aberrancy seismic attributes may be the most effective attribute in illuminating fault traces. Essentially, the aberrancy and curvature attributes may be additionally effective in delineating fault zones with sub-seismic offsets, whereas the coherence attribute may be more useful where the fault offset is significant enough to be seismically resolvable. However, we find that an interpretation approach that incorporates all three attributes best illuminates the lateral extents of the mapped fault (e.g., Figure 6b). Although previous structural investigations in the Anadarko Basin utilized curvature and coherence attributes to delineate fault segments (Elebiju et al., 2011; Liao et al., 2017; Kolawole et al., 2019, 2020), we emphasize that the aberrancy seismic attribute provides even better detail of structural deformation in such geologic settings as the study area (e.g., Patel and Marfurt, 2019).

Our results show that several faults in the study area extend from the sedimentary cover into the basement (e.g., Figures 4c and 4f, 8b, 10b-c). A detailed analysis of the vertical partitioning of structural styles along the basement-rooted faults in the Anadarko Basin was presented in Kolawole et al. (2020). It was shown that the faults are transpressional faults with an upward propagation that features a deeper domain of faulted blocks near the top basement, which transitions into faulted monocline upsection and simple monoclinal flexures in the shallower sections. Therefore, the small vertical offset of these faults provides an explanation for the rare occurrence of fault offsets only in the near top basement depths, and dominance of monoclinal flexures across most of the sedimentary section (e.g., Figure 3a). Additionally, the relatively more-compliant mechanical properties of the sedimentary units make it easier for the faults and top

basement paleotopographic features to flexurally deform the rocks. Hence, faults show better continuity on Hunton than the top of the basement. Therefore, we propose that, in fact, the large-scale structural styles of these small-offset faults make the aberrancy and curvature (flexure-illuminating) seismic attributes the ideal attributes for their illumination.

In both plane-view (e.g., Figures 5-6, 9) and cross-section (Figures 10a-c), the distribution of relocated seismicity clusters shows a collocation of the earthquakes with our carefully illuminated fault lineaments. Thus, we recommend the use of aberrancy and curvature seismic attributes for the investigation of potentially seismogenic faults in the Anadarko Basin, and other intraplate sedimentary basins where small-offset pre-existing faults pose critical seismic hazards. In relation to the recent spike in induced seismicity in Oklahoma and surrounding areas (e.g., Figure 1a), the seismogenic basement-rooted faults are often delineated after the fact (e.g., Schoenball and Ellsworth, 2017; Chen et al., 2017; Kolawole et al., 2019). There are several fault lineaments in the survey along or in the vicinity of which no earthquake activities have been recorded (e.g., Figure 6d). However, we suggest that the careful integration of fault geometry mapping (using the recommended seismic attributes) with geomechanical modeling of fault reactivation potential (e.g., Walsh and Zoback, 2016; Qin et al., 2019) of the mapped faults may be effective in mitigating resource-exploration-related seismic triggering.

The Illuminated Fault Structure and Induced Seismicity in Central Oklahoma and Other Areas

The illuminated faults show dominant plan-view trends along the N-S, NW-SE, and NE-SW orientations (Figures 7b-d). The focal mechanism solutions for the events show a predominance of strike-slip with minor normal fault reactivation on NW and NE-trending nodal planes (Figures 9a-b). Kolawole et al. (2019) demonstrated that the structural fabric of the

Precambrian crystalline basement underlying Oklahoma, Kansas, and surrounding areas is defined by a prominent NE- and NW- trending fault and fracture networks with a minor N-S trending set. Kolawole et al. (2020) showed that these Precambrian structural trends were reactivated in the Late Paleozoic, leading to basement-driven (unidirectional) and metasedimentary-driven (bi-directional) fault propagation patterns across the Anadarko Shelf. However, Qin et al. (2019) showed that in various parts of the basin, these three structural trends were reactivated in varying proportions relative to one another, such that in some places, only one or more of the structural trends propagated up into the pre-Paleozoic cover. Here, we observe a dominance of all three structural trends, extending across the basement-sedimentary interface (Figures 7b-c and 10a-c). In addition, the relative abundance of faulting in the basement compared to the sedimentary cover (Figure 7a) is consistent with observations in Kolawole et al. (2020), which suggested that it is related to the partial reactivation of the inherited Precambrian basement faults in the Late Paleozoic.

The present-day strike-slip faulting regime observed in the study area (Figures 9a-b) is consistent with most areas of seismicity in the basin (e.g., Alt and Zoback, 2017; Qin et al., 2019). The normal faulting events may be associated with flower structures along the strike-slip faults, as observed in the Woodward sequence located farther northwest of the study area (Qin et al., 2018). Previous studies have shown how fault orientations with respect to the ambient stress field influence the susceptibility of fault segments to shear reactivation which may be seismogenic or aseismic (e.g., Walsh and Zoback 2016; Alt and Zoback, 2017; Kolawole et al., 2019; Qin et al., 2019). Based on the orientation of maximum horizontal stress in the Kingfisher County area (~83° red arrows in Figures 7b-d; Qin et al., 2019), we infer that the NW-SE and NE-SW -trending fault segments are most critically oriented for shear reactivation in the present-day stress field. Thus, it

is not surprising that the illuminated fault lineaments with earthquakes on them (Figures 9a-b) are oriented at low oblique angles to the stress field. However, it is important to note that the illuminated N-S -trending fault lineaments could also be seismogenically triggered at very high fluid pressures (Qin et al., 2019).

As described above, the interpreted faults are basement-rooted strike-slip faults that developed during the Late Paleozoic transpressional tectonics (Liao et al., 2017; Gay, 2003; Kolawole et al., 2020), and the vertical partitioning of their structural styles (Kolawole et al., 2020) facilitate a prevalence of flexures along most of their segments (e.g., Figures 3a, 10a-c). These flexures may be simple differential compaction folds, faults smeared by seismic processing, sub-seismic conjugate faults or folds associated with reactivated basement faults. Patel and Marfurt (2019) hypothesized that some of the flexures are due to differential compaction caused by top basement paleotopography.

The seismicity recorded within the study area (Figures 8a-b) may be related to fault reactivation by wastewater disposal into the deeper sedimentary units (e.g., Arbuckle Formation), hydraulic fracturing within shallower sedimentary units (e.g., Woodford and Hunton Formations), or natural intraplate fault reactivation. The vertical extents of the seismic events (Figure 8b) and collocation with fault discontinuities in the 3D seismic data (Figures 10a-c) may indicate a potential link between intra-sedimentary and basement-hosted seismicity in this part of the Anadarko Basin. Therefore, the analyses presented in this study may provide better insight into the structures in the area relevant for future exploration activities in the area.

CONCLUSIONS

In this paper, we used attributes computed on 1100 square miles of seismic reflection data to delineate the tectonic framework of the STACK area of the Anadarko Basin. The attributes reveal that the faults in the area extending from sedimentary cover into the basement with the rare occurrence of offsets near the top basement but the prevalence of flexures across the sedimentary section. We show that though broadband coherence delineated some of the faults near the basement, it fails to image them in the sedimentary section due to sub seismic offset of the faults. Because of layering, the empirical analysis showed that faults are tuned at a 30-55 Hz frequency in the Mississippian formations. Hence, we suggest limiting multispectral coherence to the bandwidth that best represents the discontinuities of interest. The lateral and horizontal continuity of the fault is best delineated by flexure-sensitive attributes such as curvature and aberrancy. Unlike coherence, curvature and aberrancy map smoothly deformed rather than discontinuous structural features. We demonstrate that location of the fault is best delineated by the combination of bandlimited multispectral coherence, aberrancy, and curvature. Aberrancy delineates the most number of fault lineaments, and we consider it the most effective attribute to delineate tectonic features in the geologic setting such as Anadarko Basin. The lineament analysis of the seismic attributes shows that the density of fault lineaments decreases from sedimentary layers to top basement. The illuminated faults show multimodal distribution with dominant plan view trends along N-S, NW-SE, and NE-SW.

The locally recorded earthquakes collocate near the fault lineaments delineated by the seismic attributes indicating the seismogenic nature of the faults in the Anadarko Basin. The earthquake cluster reveals a sub-vertical rupture plane extending from the sedimentary section to the deep basement. The focal mechanism of the earthquakes reveals predominantly strike-slip

faulting with minor normal faulting along NW and NE-trending nodal planes. Some of the recent earthquake events occur in the sedimentary section coinciding with the increase in oil and gas exploration and production activities in the region. There are several faults in the STACK area, which are imaged by the seismic attributes shown in this study, but no earthquake activities have been recorded in their vicinity. We propose to study the reactivation potential of those faults. We also recommend the use of flexure sensitive attributes to delineate structural features in other Basins with similar structural characteristics as Anadarko Basin.

ACKNOWLEDGMENTS

We thank TGS for providing a license to the 3D seismic reflection data used in this study. We thank the Oklahoma Geological Survey (OGS) for providing the earthquake data used in this study. The first author wishes to thank Marathon Oil for financial support during the last two years of his PhD studies, devoted to studying the Meramec formation of the STACK play.

FIGURES

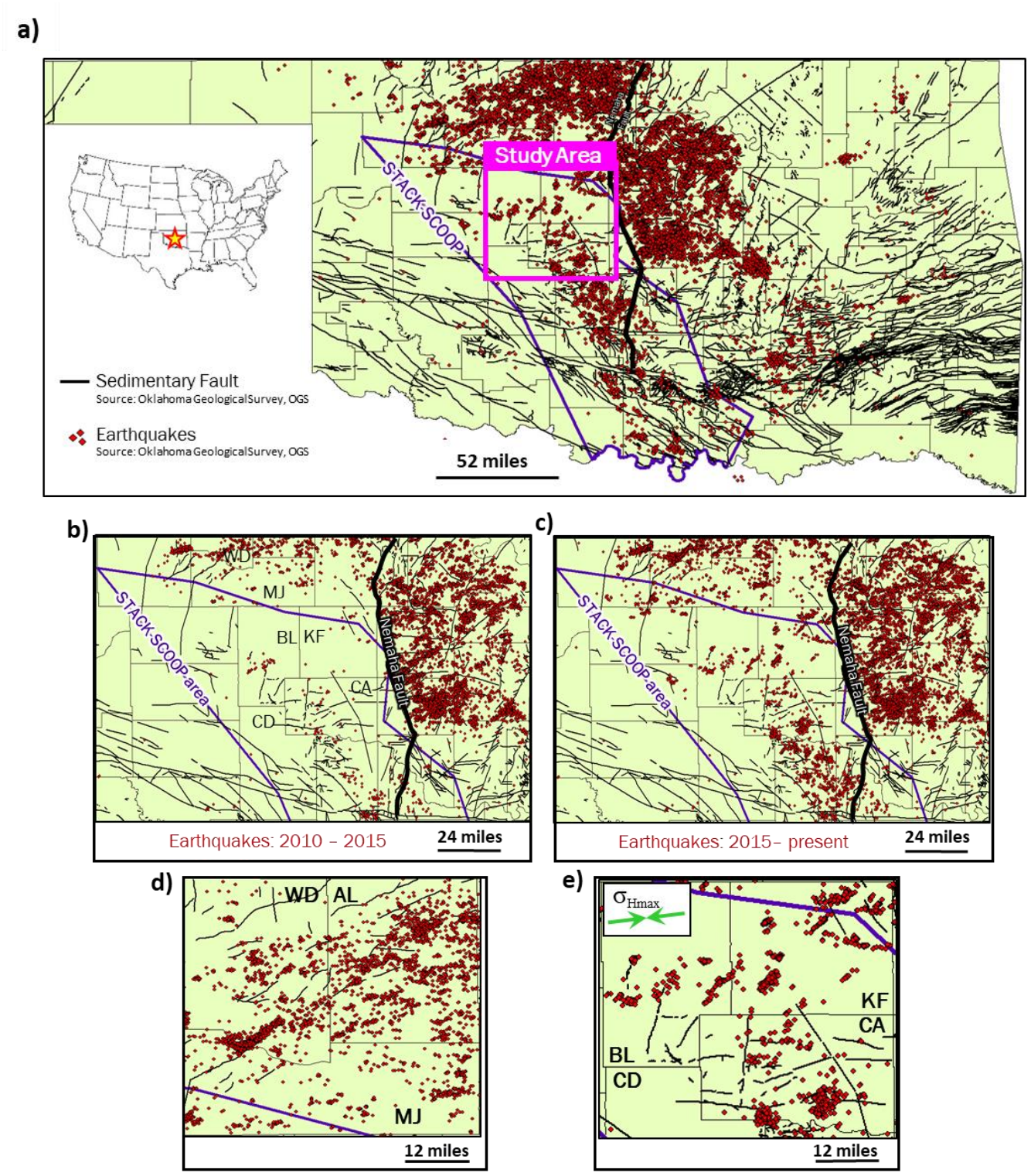

Figure 4-1. Map of earthquakes that occurred in Oklahoma from 2010-2019. The black line shows the faults the purple line delimits the STACK and SCOOP plays, and a thick black line delineates the Nemaha fault. Zoom views of (a). The area of

Interest [KF = Kingfisher County, BL = Blaine County, CA = Canadian County, and CD = Caddo County] showing earthquake (b) before, and (c) after 2015. Note the increase in the number of earthquakes after 2015. d) A zoom view of (a) from the north of Oklahoma showing that earthquakes in Alfalfa County (AL), Major County (MJ), and Woods County (WD) do not coincide with the currently mapped faults in the region. (e) A similar observation to (d) is observed in the area of interest. (1c inset) Green arrows represent the σ_{Hmax} orientation for the Kingfisher County (from Qin et al., 2019) (data courtesy OGS).

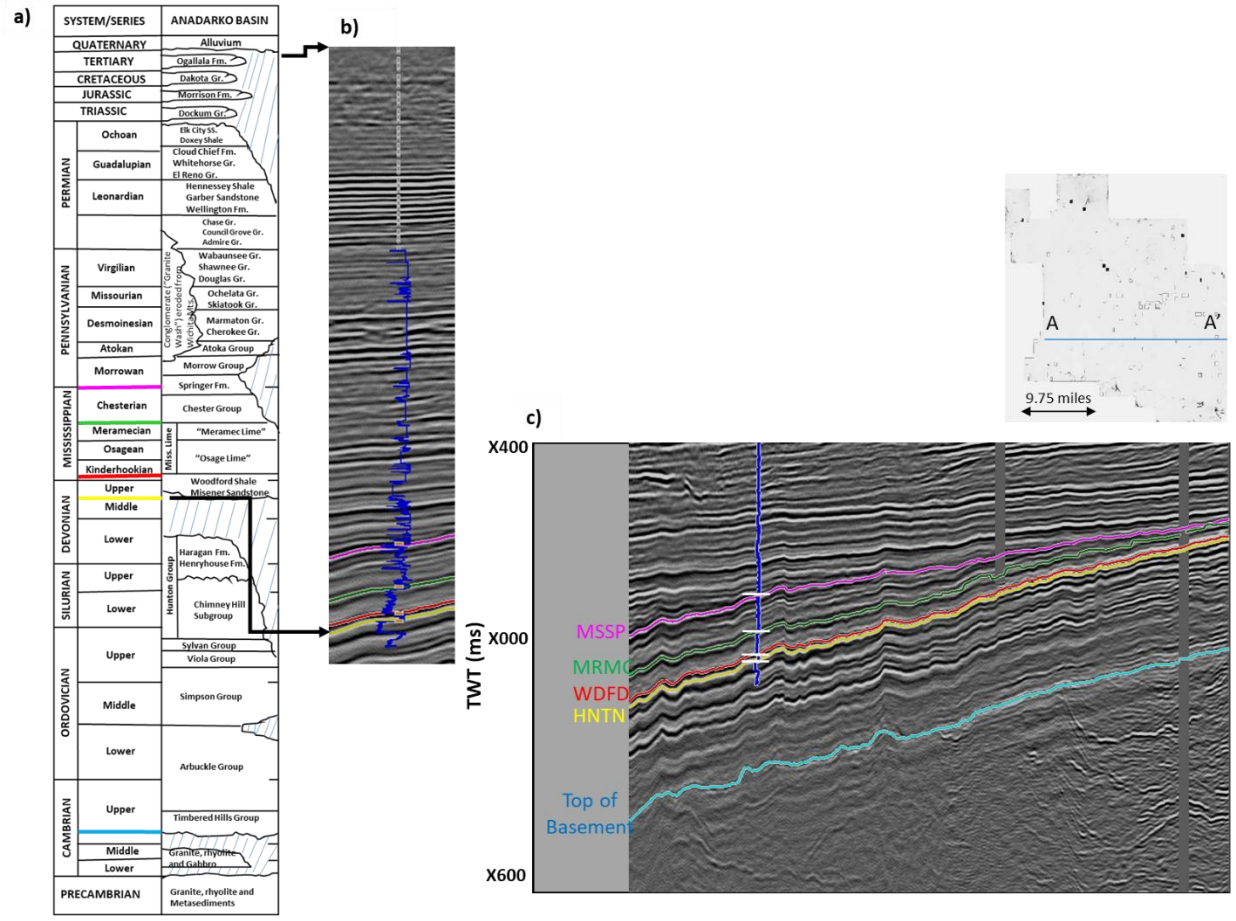

Figure 4-2. A generalized stratigraphic chart of Anadarko Basin modified from Johnson and Cardott (1992), showing formations mapped in the 3D seismic data volume. b) A zoom view of seismic cross-section near the Well. (c) An east-west seismic amplitude cross-section in the study area showing the top of the basement and top of some of the sedimentary sections interpreted using the well tops. The Meramec and Woodford are the more important oil and gas producing formations in the STACK area (Seismic data courtesy of TGS).

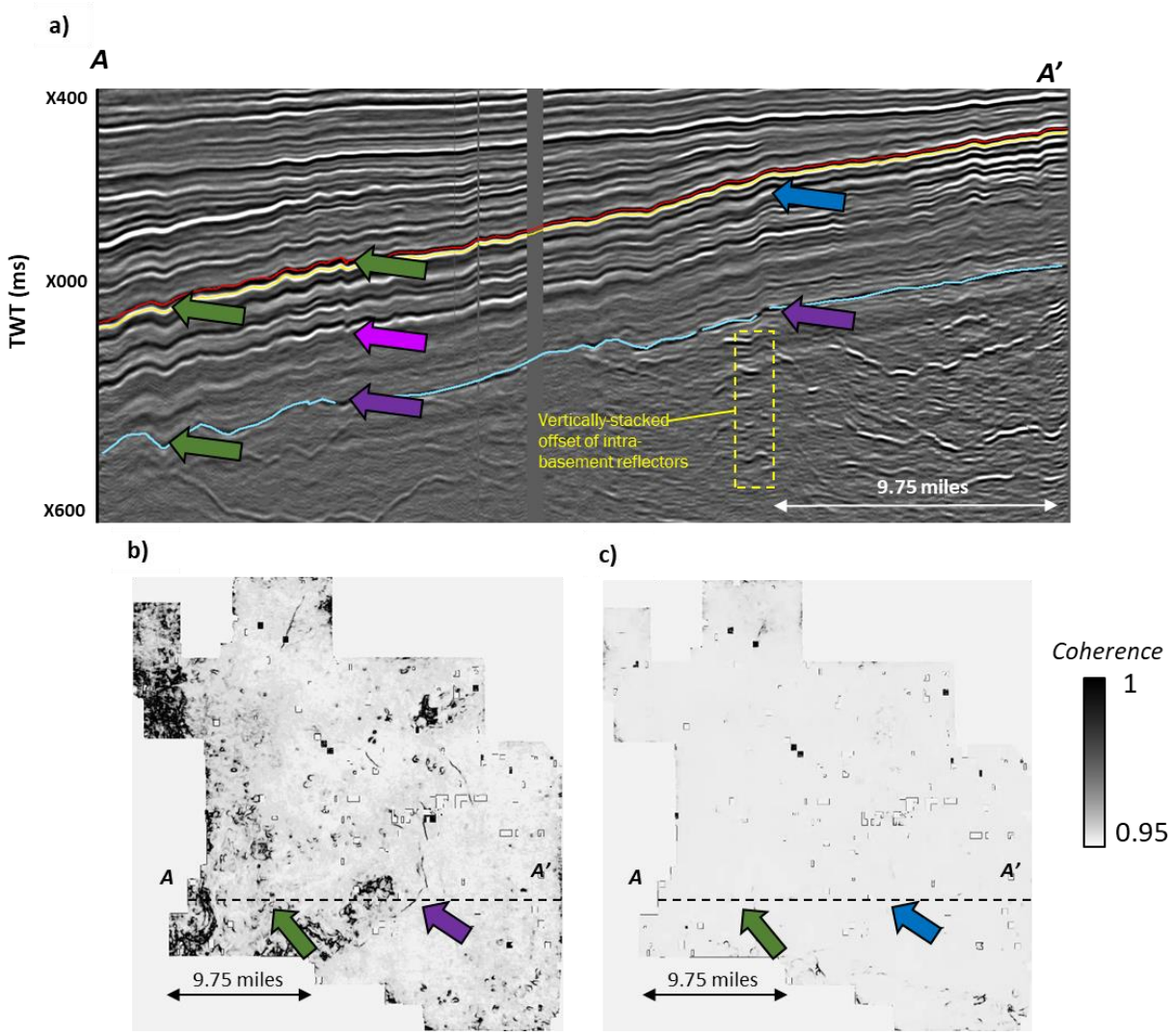

Figure 4-3. Vertical slice AA' through the seismic amplitude volume. Some faults show offsets (such as that indicated by the purple arrow) at the top of the basement (blue horizon) but appear as flexures in the sedimentary section (indicated by the blue arrow). The top Hunton (yellow horizon) and top Woodford (red horizon) form the bottom of the exploration target for most operators. Green arrows indicate a possible fault given its offset deeper in the section (pink arrow); however, because of the lack of displacement, no fault appears on the horizon slices through the coherence volume at the (b) top basement or (c) top Hunton. The purple and green arrows indicate the same locations as shown in (a) (seismic data courtesy TGS).

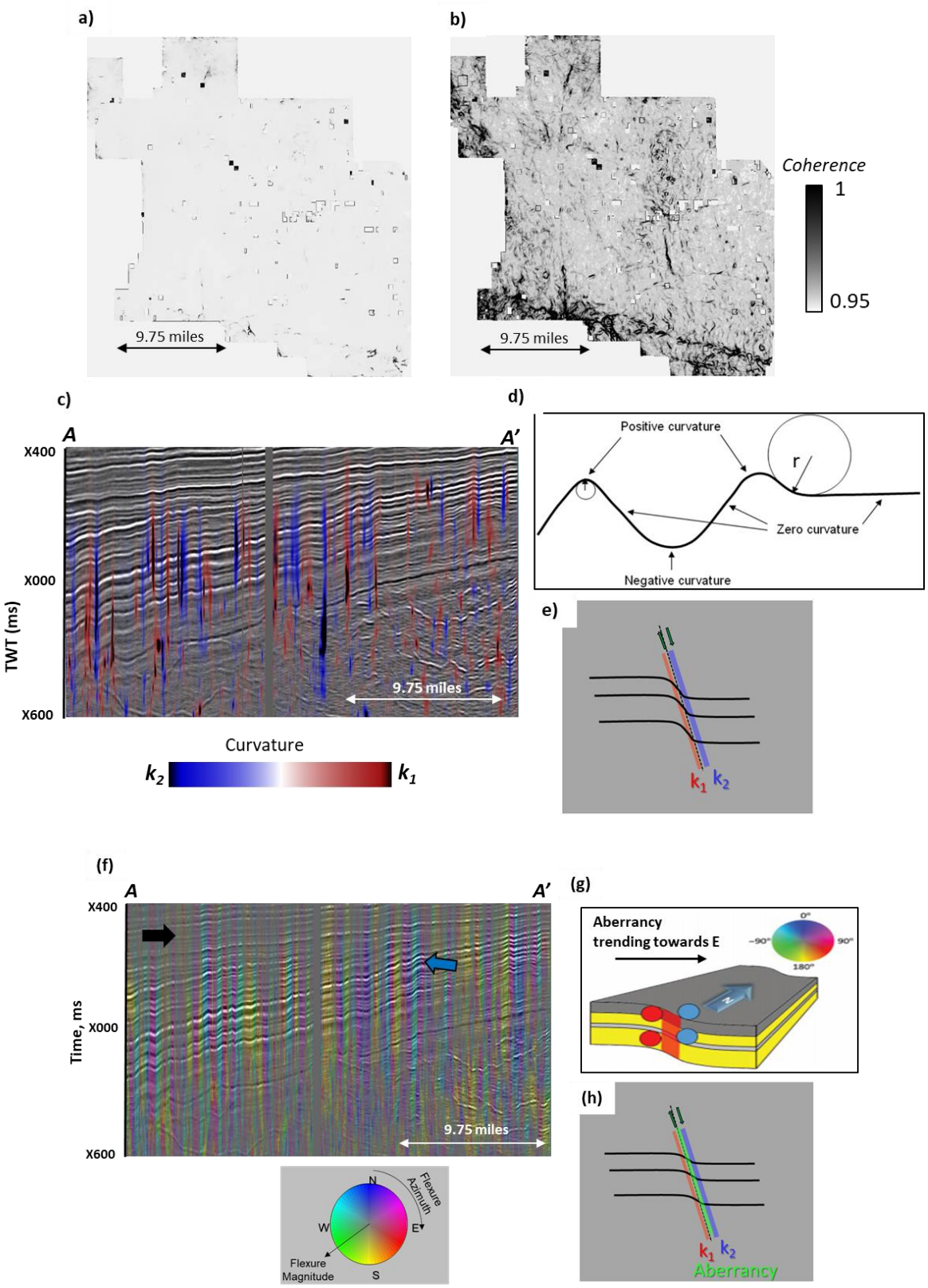

Figure 4-4. a) Broadband, and (b) bandlimited (30-55 Hz) multispectral coherence through Hunton, where the multispectral coherence provides improved fault images. (c) seismic amplitude co-rendered with most-positive (k_1) and most-negative (k_2)

curvature. For normal faults, k_1 delineates the footwall while k_2 delineates the hanging wall. (d) A cartoon showing curvature on a 2D structure. The synclinal feature exhibits negative curvature, generally mapped as a blue anomaly by k_2, whereas the anticlinal feature exhibits positive curvature, mapped as a blue anomaly by k_1. Planar features exhibit zero curvature (Chopra and Marfurt, 2007). (f) Vertical slice AA' through seismic amplitude co-rendered with the aberrancy vector (defined by a magnitude and azimuth). The planar features appear grey (black arrow) while the strong flexures appear colored where the color represents the azimuth of downside of the flexure. (g) A cartoon showing that aberrancy measures the lateral change of the curvature (After Qi and Marfurt, 2018). (h) A cartoon showing that for a fault zone whose offset falls below seismic resolution that curvature anomalies bracket a fault while aberrancy aligns with the fault trace (Seismic data courtesy of TGS).

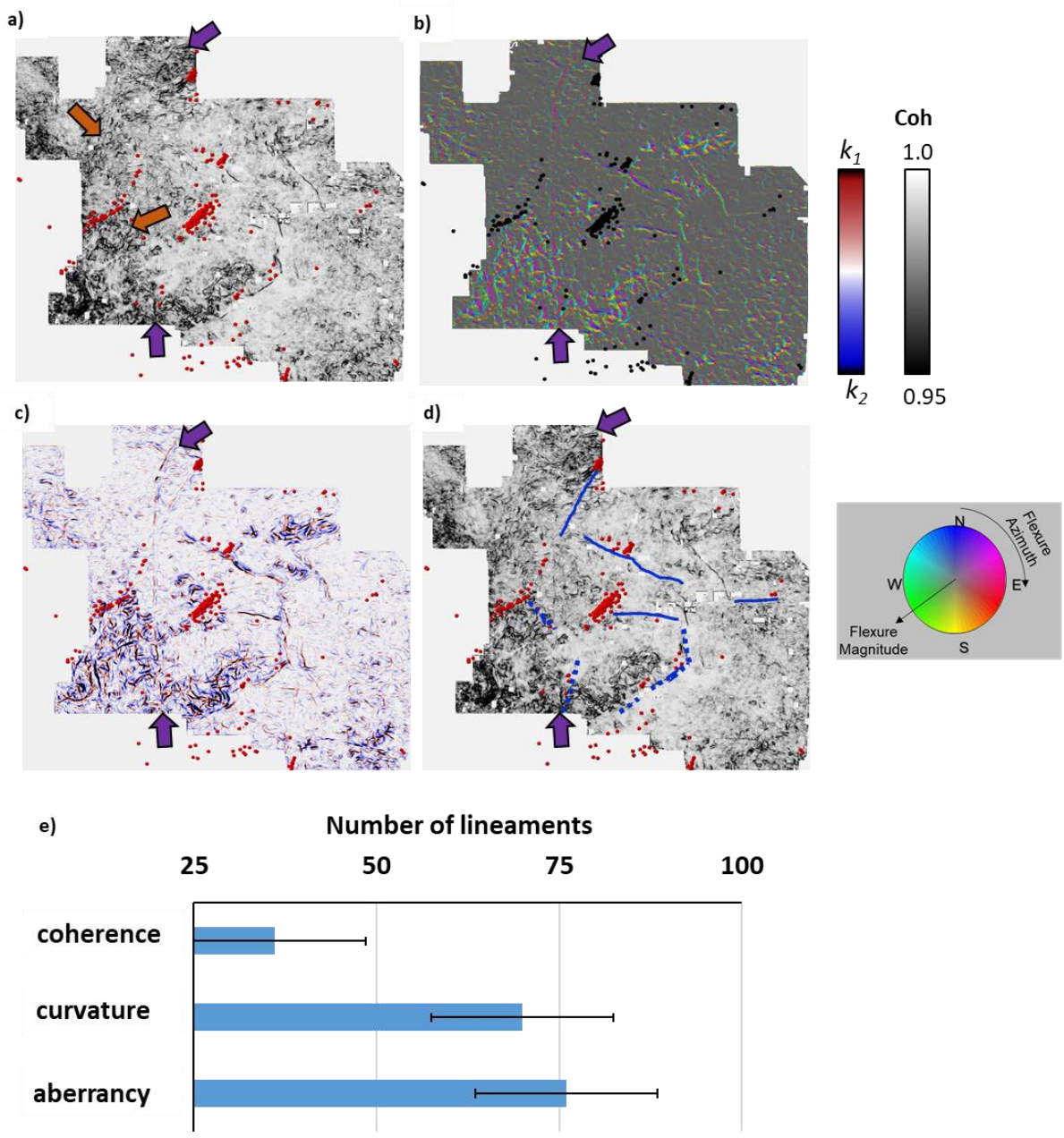

Figure 4-5. Horizon slices along top basement through the (a) bandlimited multispectral coherence (30-55 Hz), (b) co-rendered aberrancy magnitude and azimuth volumes, and (c) co-rendered k_1 and k_2 curvature. Earthquake locations indicated as red or black dots. (d) The same horizon slice shown in (a) but now with seismogenic faults mapped by curvature and aberrancy marked as blue lines. Seismogenic faults that are better mapped by aberrancy appear as dashed blue lines. The purple arrow indicates the NS strike-slip El Reno fault, which is poorly imaged by coherence but well imaged by curvature and aberrancy. The orange arrow points to paleotopographic features on top basement. (e) Statistical analysis of the number of faults mapped on (a), (b), and (c). (Earthquake locations from the Oklahoma Geological Survey catalog (Seismic data courtesy of TGS).

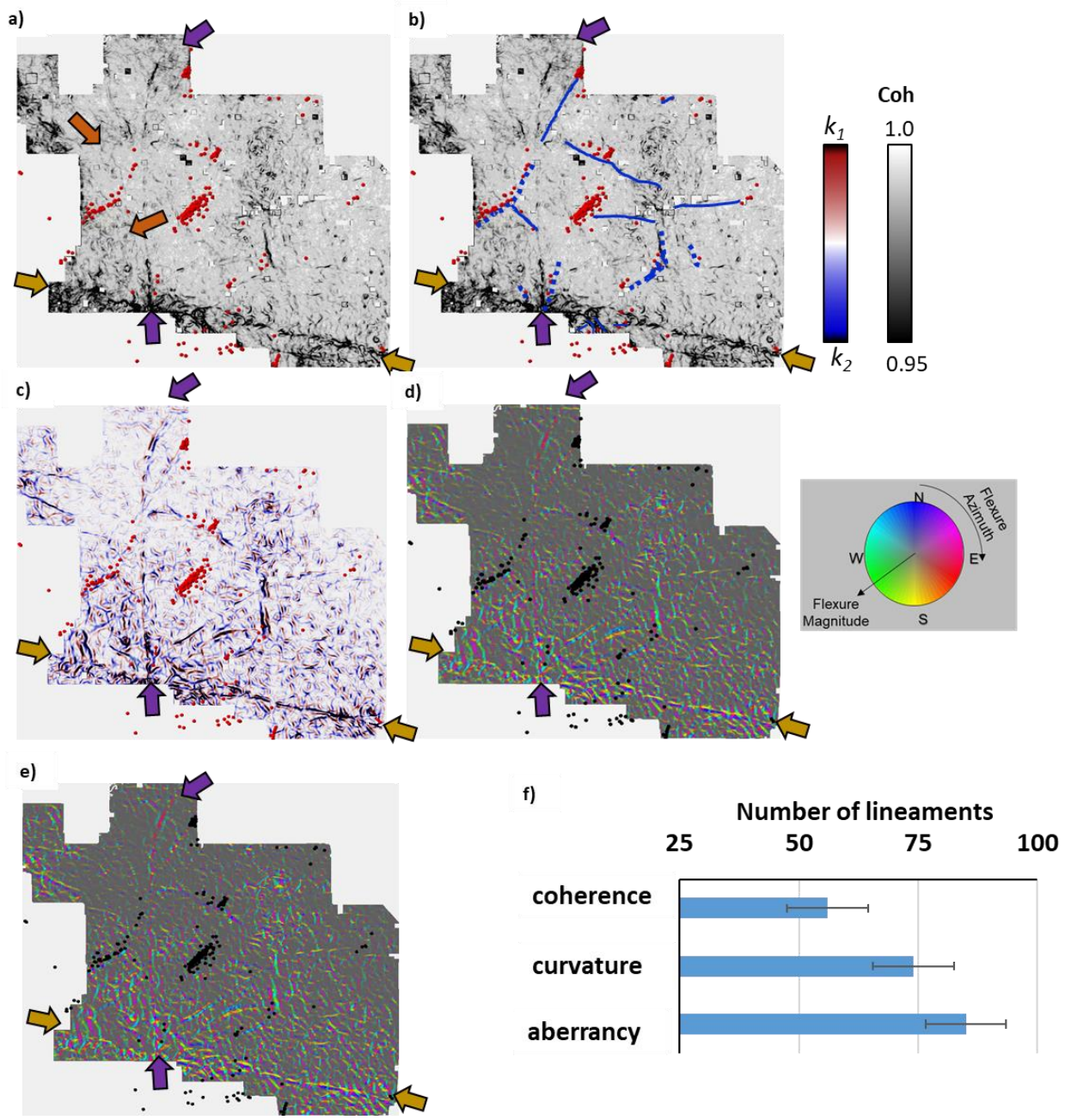

Figure 4-6. Horizon slices along the top Hunton through the (a) bandlimited multispectral coherence (30-55Hz), (b) co-rendered k_1 and k_2 curvature, and (c) co-rendered aberrancy magnitude and azimuth volumes. (d) The same horizon slice shown in (a) but now with seismogenic faults mapped by curvature and aberrancy marked as blue lines. Seismogenic faults that are better mapped by aberrancy appear as dashed blue lines. The purple arrow indicates the same NS strike-slip El Reno fault as in Figure 5. Yellow arrows indicate EW strike-slip faults that do not appear on the top of the basement but appear on the top Hunton. The orange arrow points to the same location as Figure 7a indicating decrease in paleotopographic feature's signature on Hunton. The seismic attributes on Hunton delineate several other structural features on Hunton that do not appear on top of the basement. (e) Horizon

slice along the top Woodford through the co-rendered aberrancy magnitude and azimuth volumes. Note there is little change from the top Hunton shown in (c). (f) Statistical analysis of the number of faults mapped on (a), (b), and (c). (Red and Black earthquake locations from the Oklahoma Geological Survey catalog (Seismic data courtesy of TGS).

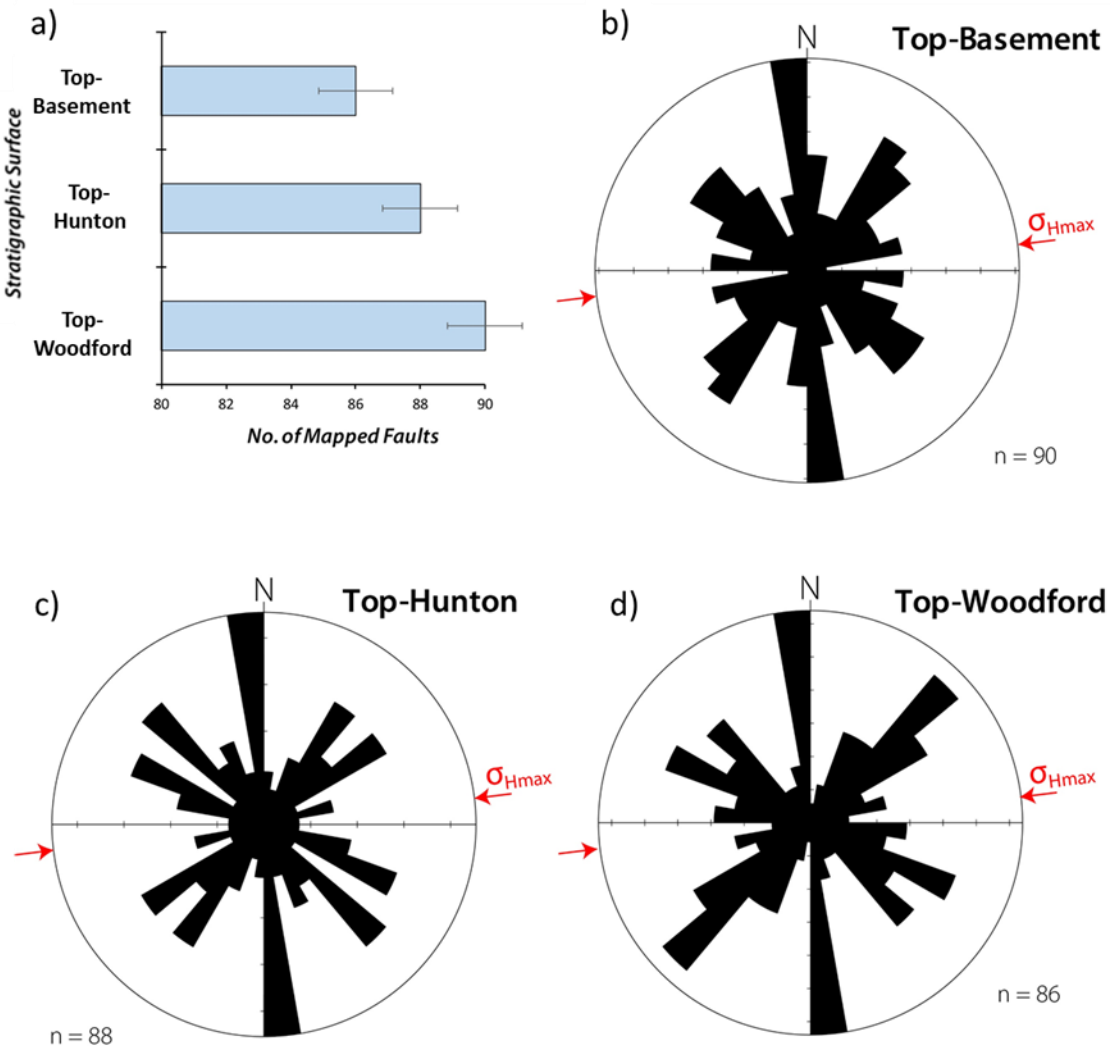

Figure 4-7. (a) Histogram of interpreted faults for the three stratigraphic surfaces mapped in this study. Most earthquakes occur in the shallow basement. Frequency-azimuth rose diagrams of the mapped fault segments for (b) top basement, (c) top Hunton, and (d) top Woodford showing dominant trends along N-S, NW-SE, and NE-SW. Red arrows represent the σ_{Hmax} (maximum horizontal stress) orientation for the study area found by Qin et al. (2019).

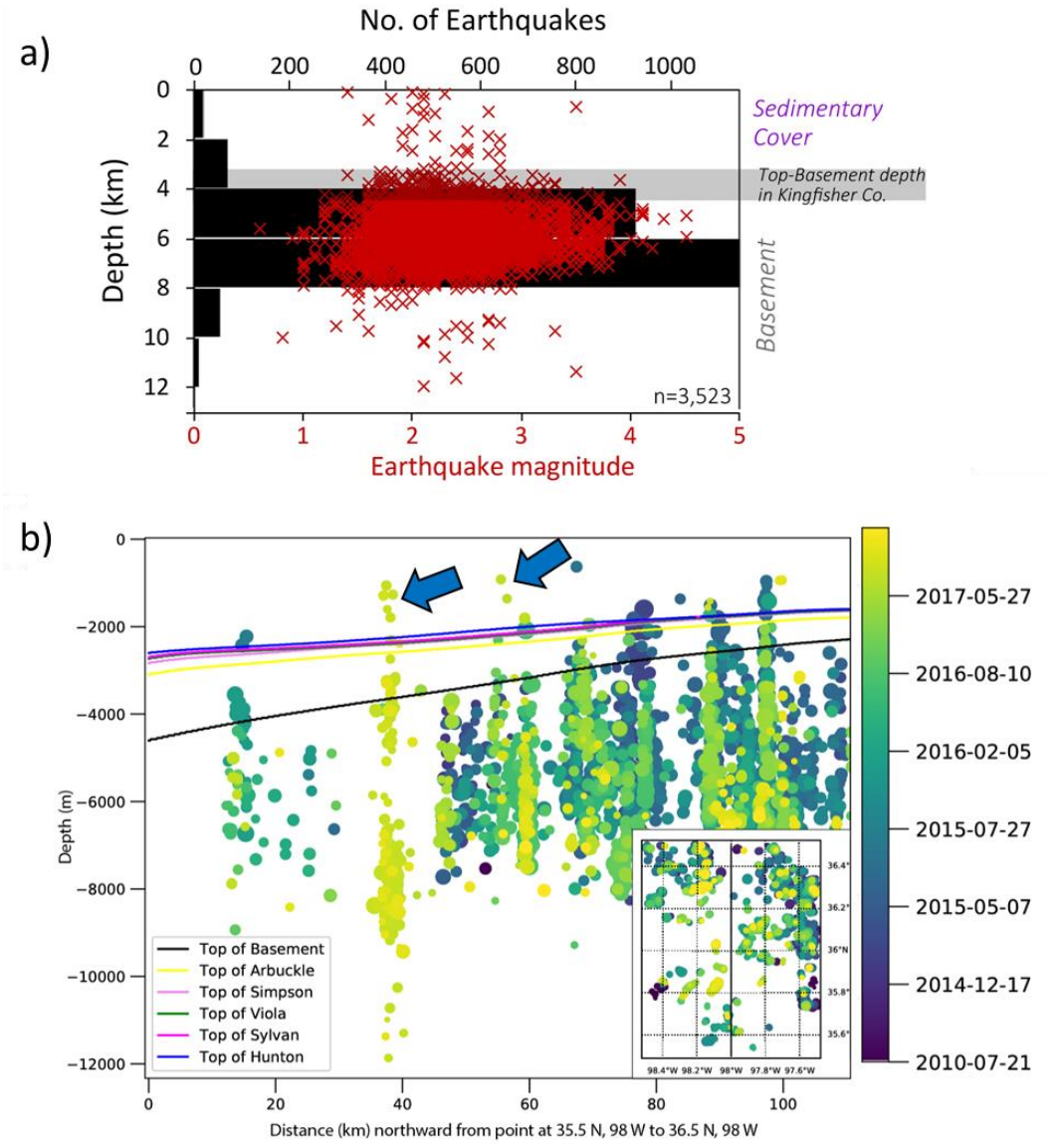

Figure 4-8. (a) Histogram of the depth distribution of the relocated earthquakes in the study area overlaid with the depth-distribution of earthquake magnitude. (b) N-S vertical section across the study area, showing the temporal evolution of the seismicity and the sub-vertical geometries of the earthquake clusters. The blue arrows point to recently occurred earthquakes in the sedimentary section. Horizons are top basement (in black), top Arbuckle (in yellow), top Simpson (in pink), top Viola (in green), top Sylvan (in dark pink), and top Hunton (blue). The top basement surface (black line) is from Crain and Chang (2018) (data courtesy OGS).

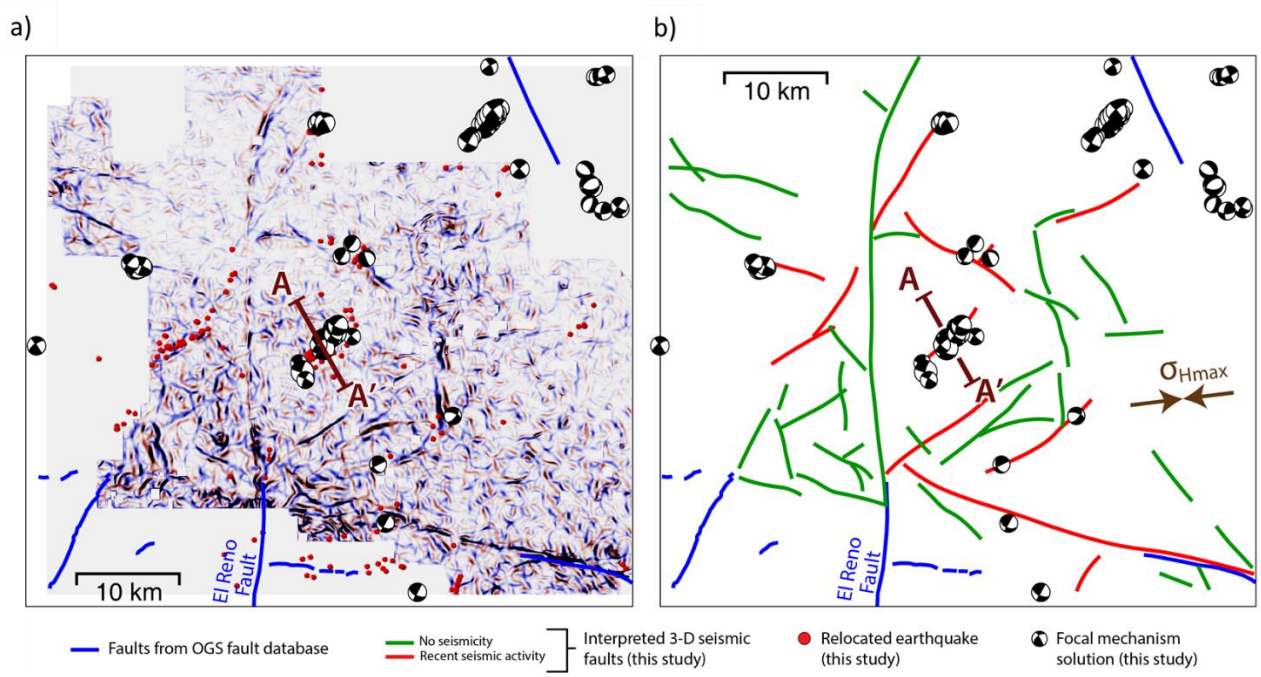

Figure 4-9(a) Horizon slice along the top Hunton through the co-rendered k_1 and k_2 curvature volumes overlaid with seismicity epicenters, focal mechanism solutions, and previously reported fault segments in the area. (b) Interpretation of the illuminated fault lineaments in Figure 9a. The red and green lines are the interpreted faults from 9a, and blue lines shows the faults from OGS. Earthquake information courtesy of the Oklahoma Geological Survey. Brown arrows represent the σ_{Hmax} orientation for the study area computed by Qin et al. (2019) (seismic data courtesy TGS and earthquake data courtesy OGS).

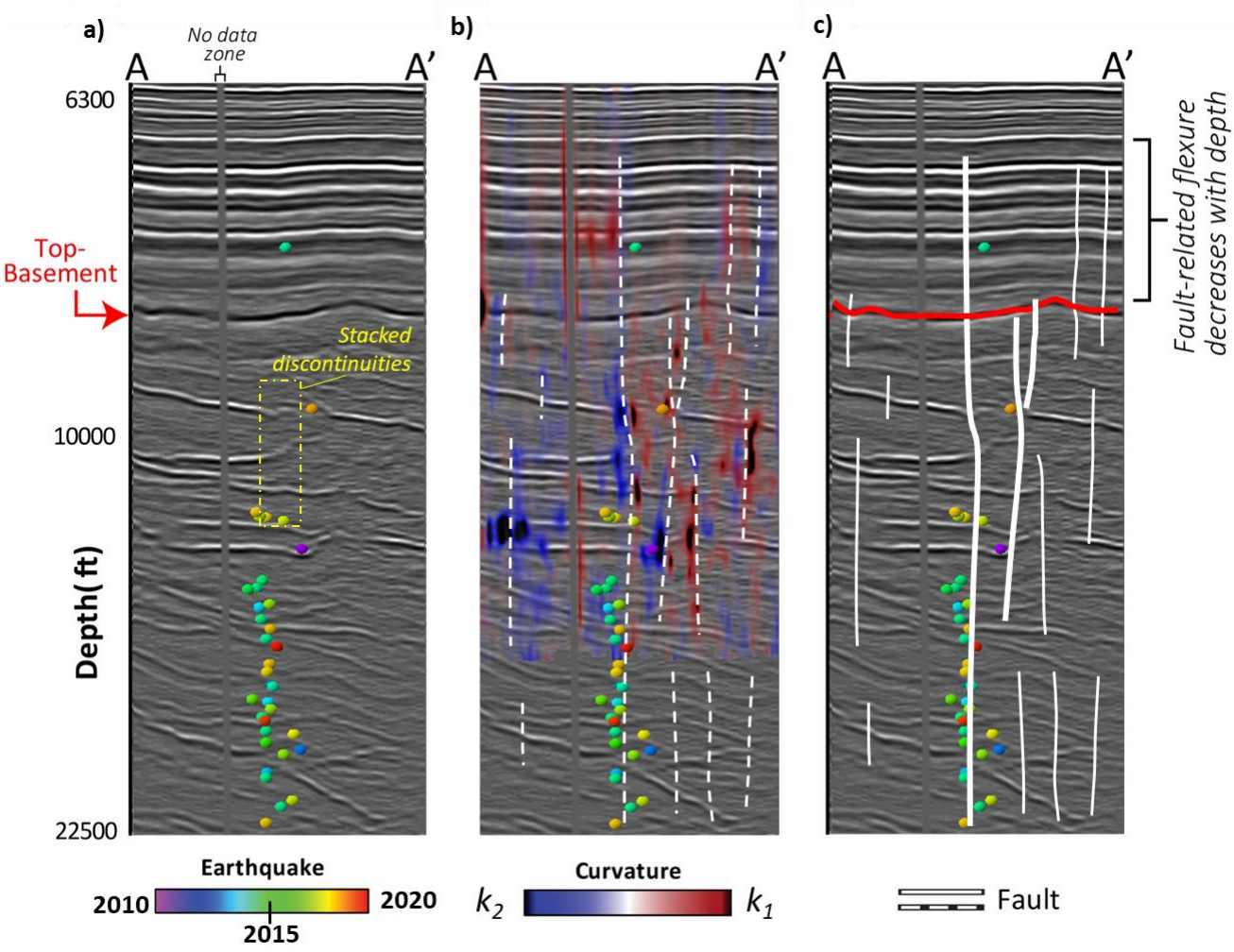

Figure 4-10. (a) Vertical slice through depth-converted (a) seismic amplitude volume along line BB' through the NW-trending earthquake cluster shown in Figure 9) (b) Line BB' through co-rendered amplitude and k_1 and k_2 curvature volumes. The vertical anomaly adjacent to the no-permit zone is an artifact. (c) Interpreted faults on line AA' using flexures mapped by curvature and discontinuities seen in the seismic amplitude data. The reflectors in the basement are from intruded sills, some of which are faulted (Chopra et al., 2017; Kolawale et al., 2020) (seismic data courtesy TGS).

REFERENCES

Alt, R. C. and M. D. Zoback, 2017, In Situ Stress and Active Faulting in Oklahoma In Situ Stress and Active Faulting in Oklahoma: Bulletin of the Seismological Society of America, 107 (1), 216-228. https://doi.org/10.1785/0120160156

Burke, K., 1977, Aulacogens and continental breakup: Annual Review of Earth and Planetary Sciences, 5, no. 1, 371–96. https://doi.org/10.1146/annurev.ea.05.050177.002103

Chen, X., N., Nakata, C. Pennington, J. Haffener, J. C. Chang, X. He, Z. Zhan, S. Ni, and J. I. Walter, 2017, The Pawnee earthquake as a result of the interplay among injection, faults and foreshocks: Scientific Reports, 7 (1), 1-18. https://doi.org/10.1038/s41598-017-04992-z

Chopra, S. and K. J. Marfurt, 2007, Seismic attributes for prospect identification and reservoir characterization: SEG Geophysical Development series no.11.

Chopra, S. and K. J. Marfurt, 2007, Seismic curvature attributes for mapping faults/fractures, and other stratigraphic features: CSEG Recorder, 32 (9), 37-41.

Chopra, S., L. Infante-Paez, and K. J Marfurt, 2017, Intra-basement intrusions in the STACK area of Oklahoma: AAPG Explorer, 42229.

Crain, K. D. and J. C. Chang, 2018, Elevation map of the top of the crystalline basement in Oklahoma and surrounding states: Oklahoma Geological Survey. Open-File Rept. OF1-2018.

Elebiju, O. O., S. Matson, G. R. Keller, and K. J. Marfurt, 2011, Integrated geophysical studies of the basement structures, the Mississippi chert, and the Arbuckle Group of Osage County region, Oklahoma: AAPG Bulletin, 95, 371–393. https://doi.org/10.1306/08241009154

Ellsworth, W.L., 2013, Injection-induced earthquakes: Science, 341 (6142), 1225942. https://doi.org/10.1126/science.1225942

Eyre, T. S., D. W. Eaton, M. Zecevic, D. D'Amico, and D. Kolos, 2019, Microseismicity reveals fault activation before Mw 4.1 hydraulic-fracturing induced earthquake: Geophysical Journal International, 218(1), 534-546. https://doi.org/10.1093/gji/ggz168

Gao, D., 2013, Wavelet spectral probe for seismic structure interpretation and fracture characterization: a workflow with case studies: Geophysics, 78, 57–67. https://doi.org/10.1190/geo2012-0427.1

Gao, D., and H. Di, 2015, Extreme curvature and extreme flexure analysis for fracture characterization from 3D seismic data: New analytical algorithms and geologic implications: Geophysics, 80 (2), IM11–IM20, https://doi.org/10.1190/geo2014-0185.1

Gay, S. P. Jr., 2003, The Nemaha trend-a system of compressional thrust-fold, strike-slip structural features in Kansas and Oklahoma (part 2, conclusion): The Shale Shaker, 54, 39–49.

Hardebeck, J. L., and P. M. Shearer, 2002, A new method for determining first-motion focal mechanisms: Bulletin of the Seismological Society of America, 92, 2264-2276. https://doi.org/10.1785/0120010200

Holland, A. A., 2013, Earthquakes triggered by hydraulic fracturing in south-central Oklahoma: Bulletin of the Seismological Society of America, 103 (3), 1784-1792. https://doi.org/10.1785/0120120109

Holloway, S., A. Holland, A. and G. Keller, 2015, Industry Contributions to the Oklahoma Fault Database. In Mid-Continent Section.

Johnson, K. S. and B. J. Cardott, 1992, Geologic framework and hydrocarbon source rocks of Oklahoma: in Source rocks in the southern midcontinent, 1990 symposium, Oklahoma Geological Survey Circular, 93, 21-37.

Johnson, K., 2008, Geologic History of Oklahoma: Educational Publication, 9, 3–8

Kaven, J. O., S. H. Hickman, A. F. McGarr, and W. L. Ellsworth, 2015, Surface monitoring of microseismicity at the Decatur, Illinois, CO2 sequestration demonstration site: Seismological Research Letters, 86(4), 1096–1101. https://doi.org/10.1785/0220150062

Li, F., J. Qi, B. Lyu, and K. J. Marfurt, 2018, Multispectral coherence: Interpretation, 6(1), T61-T69. https://doi.org/10.1190/INT-2019-0124.1

Lei, X., D. Huang, J. Su, G. Jiang, X. Wang, H. Wang, X. Guo, and H. Fu, 2017, Fault reactivation and earthquakes with magnitudes of up to Mw4.7 induced by shale-gas hydraulic fracturing in Sichuan Basin, China: Scientific Reports, 7, 7971. https://doi.org/10.1038/s41598-017-08557-y

Langenbruch, C., M. Weingarten, and M. D. Zoback, 2018, Physics-based forecasting of man-made earthquake hazards in Oklahoma and Kansas: Nature communications, 9(1), 1-10. https://doi.org/10.1038/s41467-018-06167-4

Liao, Z., H. Liu, Z. Jiang, K. J. Marfurt, and Z. E. Reches, 2017, Fault damage zone at subsurface: A case study using 3D seismic attributes and a clay model analog for the Anadarko Basin, Oklahoma: Interpretation, 5, T143–T150. https://doi.org/10.1190/INT-2016-0033.1

Machado, G. L., G. J. Hickman, M. P. Gogri, K. J. Marfurt, M. J. Pranter, and Z. A. Reza, 2019, Characterization of Arbuckle-basement wastewater disposal system, Payne County,

Northern Oklahoma: Interpretation, 7(4), SL19-SL36. https://doi.org/10.1190/INT-2019-0025.1

Marsh, S. and A. Holland, 2016, Comprehensive fault database and interpretive fault map of Oklahoma: Oklahoma Geological Survey. Open-File Rep. OF2-2016.

McBee, W., 2003a, The Nemaha and other strike-slip faults in the midcontinent USA: AAPG Mid-Continent Section Meeting Proceedings, 1–23.

National Research Council, 2013. Induced seismicity potential in energy technologies. National Academies Press, pp.31-48.

Patel, S. and K. J. Marfurt, 2019, Flexures in the Anadarko Basin: Do they indicate faulting or folding?: 90th Annual International meeting, SEG, Expanded Abstracts, 1953-1957. https://doi.org/10.1190/segam2019-3216621.1

Partyka, G., J. Gridley, and J. A. Lopez, 1999, Interpretational applications of spectral decomposition in reservoir characterization: The Leading Edge, 18, no. 3, 353–360. https://doi.org/10.1190/1.1438295

Perry, W. J, 1989, Tectonic evolution of the Anadarko Basin region, Oklahoma: US Geological Survey Bulletin, no. 1866.

Peyton, L., R. Bottjer, and G. Partyka, 1998, Interpretation of incised valleys using new-3D seismic techniques: A case history using spectral decomposition and coherency: The Leading Edge, 17, 1294–1298. https://doi.org/10.1190/1.1438127

Qi, X. and K. J. Marfurt, 2018, Volumetric aberrancy to map subtle faults and flexures: Interpretation, 6(2), T349-T365. https://doi.org/10.1190/INT-2017-0114.1

Qin, Y., X. Chen, B. M. Carpenter, and F. Kolawole, 2018, Coulomb stress transfer influences fault reactivation in areas of wastewater injection: Geophysical Research Letters, 45 (20), 11059-11067. https://doi.org/10.1029/2018GL079713

Qin, Y., X. Chen, J. I. Walter, J. Haffener, D. T. Trugman, B. M. Carpenter, M. Weingarten, and F. Kolawole, 2019, Deciphering the stress state of seismogenic faults in Oklahoma and southern Kansas based on an improved stress map: Journal of Geophysical Research: Solid Earth, 124 (12), 12920-12934. https://doi.org/10.1029/2019JB018377

Sagan, J. A. and B. S. Hart, 2006, Three-dimensional seismic-based definition of fault-related porosity development: Trenton–Black River interval, Saybrook, Ohio: AAPG bulletin, 90 (11), 1763-1785. https://doi.org/10.1306/07190605027

Schoenball, M., and W. L. Ellsworth, 2017, Waveform-relocated earthquake catalog for Oklahoma and southern Kansas illuminates the regional fault network: Seismological Research Letters, 88, 1252–1258. https://doi.org/10.1785/0220170083

Schmidt, I., M. Docherty, F. Pauget, and S. Lacaze, 2010, Improved 3D seismic interpretation and reservoir model construction using PaleoScan technology: AAPG, Expanded Abstract.

Shemeta, J. E., B. C Edward, and L. C. Clifford, 2020, Well Stimulation Seismicity in Oklahoma: Cataloging Earthquakes Related to Hydraulic Fracturing: In Asia Pacific Unconventional Resources Technology Conference, Brisbane, 95-106. https://doi.org/10.15530/AP-URTEC-2019-198283

Skoumal, R. J., M. R. Brudzinski, and B. S. Currie, 2015, Earthquakes induced by hydraulic fracturing in Poland Township, Ohio: Bulletin of the Seismological Society of America, 105 (1), 189-197. https://doi.org//10.1785/0120140168

Skoumal, R. J., R. Rosamiel, M. R. Brudzinski, A. J. Barbour and B. S. Currie, 2018, Earthquakes induced by hydraulic fracturing are pervasive in Oklahoma: Journal of Geophysical Research, 123 (12), 10918-10935. https://doi.org/10.1029/2018JB016790

Waldhauser F. and W.L. Ellsworth, 2000, A double-difference earthquake location algorithm: Method and application to the northern Hayward fault: Bulletin of the Seismological Society of America, 90, 1353-1368. https://doi.org/10.1785/0120000006

Walsh, F.R. and M. D. Zoback, 2015, Oklahoma's recent earthquakes and saltwater disposal: Science advances, 1 (5), 1500195. https://doi.org/10.1126/sciadv.1500195

Walsh III, F.R. and M. D. Zoback, 2016, Probabilistic assessment of potential fault slip related to injection-induced earthquakes: Application to north-central Oklahoma, USA: Geology, 44 (12), 991-994. https://doi.org/10.1130/G38275.1

Weingarten, M., S. Ge, J. W. Godt, B. A. Bekins, and J. L. Rubinstein, 2015, High-rate injection is associated with the increase in US mid-continent seismicity: Science, 348 (6241), 1336-1340. https://doi.org/10.1126/science.aab1345

APPENDIX

In the appendix we summarize mathematical details on computing curvature and aberrancy. A detail explanation on curvature computation can found in Chopra and Marfurt, 2007. Xuan and Marfurt (2018) and Di and Gao's (2014) provides detail explanation on aberrancy computation.

Curvature

Mathematically, the first step in curvature computation fits a quadratic surface $z(x,y)$ to an interpreted horizon (Chopra and Marfurt, 2007).

$$z(x,y) = ax^2+cxy+by^2+dx+ey+f \tag{A1}$$

Once the coefficients (a,b,c,d,e,f) are estimated, the mean of the curvature (k_{mean}) and Gaussian curvature (k_{Gauss}) is calculated as

$$K_{mean} = [a(1+e^2) + b(1+d^2) - cde] / (1 + d^2+ e^2)^{3/2} \tag{A2}$$

$$k_{Gauss} = (4ab-c^2) / (1+d^2+e^2)^2 \tag{A3}$$

The principal curvature (k_1 and k_2) can be calculated using k_{mean} and k_{Gauss},

$$k_1 = k_{mean} + (k_{mean}^2 - k_{Gauss})^{1/2} \tag{A4}$$

$$k_2 = k_{mean} - (k_{mean}^2 - k_{Gauss})^{1/2} \tag{A5}$$

k_1 is the most positive curvature and k_2 is the most negative curvature.

Aberrancy

Di and Gao's (2014) aberrancy computation method requires derivatives of the dip vector in a coordinate system rotated to be aligned with the local reflector dip and azimuth. Once we have computed the 2nd derivative of the dip vector in the rotated coordinate system, the apparent flexure *f(Ψ)* at azimuth Ψ is given by:

$$f(\Psi) = \frac{\partial^3 z'}{\partial x'^3}\cos^3\Psi + 3\frac{\partial^3 z'}{\partial x'^2 \partial y'}\cos^2\Psi\sin\Psi + 3\frac{\partial^3 z'}{\partial x' \partial y'^2}\cos\Psi\sin^2\Psi + \frac{\partial^3 z'}{\partial y'^3}\sin^3\Psi \quad \text{(A7)}$$

Where *x'*,*y'*, and *z'* are the rotating axis. The aberrancy is calculated by finding the extrema of equation A7. The extrema are the roots of equation A8.

$$\frac{df(\Psi)}{d\Psi} =$$

$$3\cos^3\Psi.\left[-\frac{\partial^3 z'}{\partial x' \partial y'^2}\tan^3\Psi - \left(2\frac{\partial^3 z'}{\partial x'^2 \partial y'} - \frac{\partial^3 z'}{\partial y'^3}\right)\tan^2\Psi + \left(2\frac{\partial^3 z'}{\partial x' \partial y'^2} - \frac{\partial^3 z'}{\partial x'^3}\right)\tan\Psi + \frac{\partial^3 z'}{\partial x'^2 \partial y'}\right] = 0$$

(A8)

Equation A8 is cubic in terms of *tan ψ;* hence it has three roots. The magnitude of the aberrancy is the sum of these three roots and the azimuth of the aberrancy is given by Ψ.

CHAPTER 5 CONCLUSIONS

In this dissertation, I examine the need to develop data conditioning and interpretation workflows to improve quantitative reservoir characterization of unconventional resource plays.

In chapter 2, we proposed a stretch compensation method to improve the resolution of far offset data, which is stretched by the processing steps, which aligns the non-zero offset to zero offset traces like NMO correction or prestack time migration. The stretch compensation is a function of the offset to depth ratio. I showed by comparing forward AVO modeling with original gather that a decrease in resolution of the far offset data leads to incorrect AVO estimation. The similarity between forward AVO model and stretch compensated data revealed that stretch compensation balances amplitude variation with the offset and improves AVO estimation. The balanced amplitudes and frequency across the reflectors improve the resolution of the S-impedance (Z_S) and density (ρ). We also examine the limitations of the method bases on assumptions and modeling. The method is valid for reservoirs with dip no more than 2^o due to the assumption that the stretch due to NMO is approximately the same as caused by prestack time migration. We show by elastic modeling that the method correctly estimates the composite response of the thick beds but introduces amplitude anomalies at far offset for tuned beds. The limitations of the method at tuning beds imply that the resolution improvement using bandwidth extension methods based on the location of energy peaks cannot extend the resolution of poorly resolved spectral components.

In chapter 3, we developed a workflow to combine core and seismic elastic measurements to find lateral and horizontal probability estimation of rock types away from cored well. The rock types were predicted over an area of 477 square miles between top Meramec and top Woodford

Formations in the Anadarko Basin. The probability estimates showed that the more productive rock, rock type 1, was sandwiched between the less productive rock type 3.

In chapter 4, we demonstrated the use of seismic attributes to delineate seismogenic faults in the STACK area of Oklahoma. The newly developed band-limited multispectral coherence attribute provided a significant improvement in delimiting faults compared to broadband coherence. A comparative study between aberrancy, coherence and curvature showed that the aberrancy is the best attribute to delineate the faults in a structural setting like Anadarko Basin, where strike-slip faults have a rare occurrence of offset but instead appear as flexures across the sedimentary section.